EFFECT OF 3-D HETEROGENEITIES AND TOPOGRAPHY ON SEISMIC WAVE PROPAGATION AND THE USE OF EMPIRICAL GREEN'S FUNCTIONS FOR SOURCE CHARACTERIZATION AND DISCRIMINATION

Michel Bouchon
Ningya Cheng
Matthias G. Imhof
Yingping Li
William L. Rodi
Craig A. Schultz
M. Nafi Toksöz

Earth Resources Laboratory
Department of Earth, Atmospheric, and
  Planetary Sciences
Massachusetts Institute of Technology
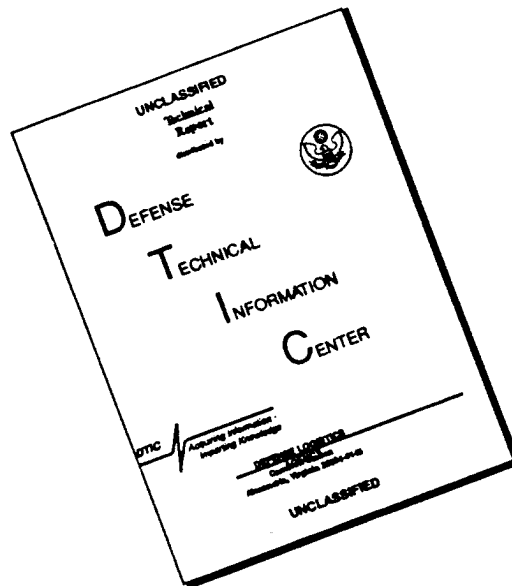Cambridge, Massachusetts 02139

1 September 1996

19961016 099

DISCLAIMER NOTICE

THIS DOCUMENT IS BEST QUALITY AVAILABLE. THE COPY FURNISHED TO DTIC CONTAINED A SIGNIFICANT NUMBER OF PAGES WHICH DO NOT REPRODUCE LEGIBLY.

REPORT DOCUMENTATION PAGE

1. AGENCY USE ONLY (Leave blank)	2. REPORT DATE	3. REPORT TYPE AND DATES COVERED
	1 SEPT. 1996	Final Technical 15 May 94-14 May 96

4. TITLE AND SUBTITLE

Effect of 3-D Heterogeneities and Topography on Seismic Wave Propagation and the Use of Empirical Green's Functions for Source Characterization and Discrimination

5. FUNDING NUMBERS

2309/AS

F49620-94-1-0282

6. AUTHOR(S)

M. Bouchon, N. Cheng, M. Imhof, Y. Li, W. Rodi, C. Schultz, M.N. Toksöz

7. PERFORMING ORGANIZATION NAME(S) AND ADDRESS(ES)

Massachusetts Institute of Technology
77 Massachusetts Avenue
Cambridge, MA 02139

8. PERFORMING ORGANIZATION REPORT NUMBER

61788

9. SPONSORING/MONITORING AGENCY NAME(S) AND ADDRESS(ES)

AFOSR/NM
110 Duncan Avenue Suite B115
Bolling AFB, DC 20332-0001

Dr. Stanley K. Dickinson

10. SPONSORING/MONITORING AGENCY REPORT NUMBER

11. SUPPLEMENTARY NOTES

12a. DISTRIBUTION/AVAILABILITY STATEMENT

Distribution Unlimited

12b. DISTRIBUTION CODE

13. ABSTRACT (Maximum 200 words)

We investigate two topics related to seismic nuclear monitoring and discrimination. The first is elastic wave propagation in complex earth models containing lateral variations in elastic properties or irregular interfaces. We describe an improved boundary element technique based on the conjugate gradient method and apply it to study the effects of surface topography. We also investigate the usefulness of a hybrid modeling method that combines multiple multipole and finite element techniques. Additionally, finite difference modeling is applied to a comparison of 2-D and 3-D scattering from irregular interfaces. The second topic area is the development of improved seismic discriminants. We find that the empirical Green's function method is effective for estimating the source time functions of earthquakes and explosions, and that the duration of the source time function is a good discriminant for large and very small events. For small events (M<3) and near regional distances (<250 km), Lg spectral ratio is a good discriminant between earthquakes and industrial explosions.

14. SUBJECT TERMS

Elastic wave scattering, boundary integral equations, multiple multipole expansions, seismic discrimination, emprical Green's functions

15. NUMBER OF PAGES

173

16. PRICE CODE

17. SECURITY CLASSIFICATION OF REPORT	18. SECURITY CLASSIFICATION OF THIS PAGE	19. SECURITY CLASSIFICATION OF ABSTRACT	20. LIMITATION OF ABSTRACT
Unclassified	Unclassified	Unclassified	

TABLE OF CONTENTS

iv

List of Contributing Scientists

Michel Bouchon, Visiting Professor, Massachusetts Institute of Technology

Matthias G. Imhof, Graduate Research Assistant, Massachusetts Institute of Technology

Yingping Li, Research Scientist, Massachusetts Institute of Technology

William Rodi, Research Scientist, Massachusetts Institute of Technology

Craig A. Schultz, Postdoctoral Associate, Massachusetts Institute of Technology

M. Nafi Toksöz, Professor of Geophysics, Massachusetts Institute of Technology

List of Previous and Related Contracts

Bibliography of Publications Totally or Partially Sponsored by the Contract

M. Bouchon, C.A. Schultz, and M.N. Toksöz, 1995, Effect of 3-D topography on seismic motion, J. Geophys. Res., 101, 5835–5846.

M. Bouchon, C.A. Schultz, and M.N. Toksöz, 1995, A fast implementation of boundary integral equation methods to calculate the propagation of seismic waves in laterally varying layered media, em Bull. Seism. Soc. Am., in press.

R.L. Gibson, Jr., M.N. Toksöz, and W. Dong, 1995, Seismic sources and wave propagation in 3-D: Radiation from cylindrical cavities, *Proceedings of the 17th Annual Seismic Research Symposium,* Scottsdale, Arizona, Air Force Phillips Laboratory.

M.G Imhof, Seismoacoustic multiple scattering: A comparison of multiple multipole expansions with an ultrasonic experiment, to be submitted to *J. Acoust. Soc. Am.*

M.G. Imhof, 1994, Scattering of acoustic and elastic waves using a hybrid multiple multipole expansions-finite element technique, accepted by *J. Acoust. Soc. Am.*

Y. Li, W. Rodi and M. N. Toksöz, 1994, Seismic source characterization with empirical Green's function and relative location techniques, *Proceedings of the 16th Annual Seismic Research Symposium,* Thornwood, New York, Air Force Phillips Laboratory, 231–237.

Y. Li, W. Rodi and M.N. Toksöz, 1995, Discrimination of earthquakes, explosions, and mining tremors using the empirical Green's function method, *Proceedings of the 17th Annual Seismic Research Symposium,* Scottsdale, Arizona, Air Force Phillips Laboratory.

Y. Li, M.N. Toksöz and W. Rodi, 1995, Source time functions of nuclear explosions and earthquakes in central Asia determined using empirical Green's functions, *J. Geophys. Res., 100,* 659–674.

Y. Li, M.N. Toksöz, and W.L. Rodi, 1996, Discrimination of small earthquakes and explosions, *Proceedings of the 18th Annual Seismic Research Symposium,* Annapolis, Maryland, Air Force Phillips Laboratory, 574–583.

C. A. Schultz, M. Bouchon, and M.N. Toksöz, 1995, Application of boundary integral equations and conjugate gradient methods to elastic wave propagation problems, submitted to *Geophysics.*

EFFECT OF 3D TOPOGRAPHY ON SEISMIC MOTION

by

Michel Bouchon [1] , Craig A Schultz [2], and M. Nafi Toksöz [3]

[1] Laboratoire de Géophysique Interne et Tectonophysique

Université Joseph Fourier

BP 53X, 38041 Grenoble, France

[2] Lawrence Livermore National Laboratory

P.O. Box 808, Livermore, California 94551

[3] Earth Resources Laboratory

Massachusetts Institute of Technology

Cambridge, MA 02139

Abstract

We present a semi-analytical, semi-numerical method to calculate the diffraction of elastic waves by an irregular topography of arbitrary shape. The method is a straightforward extension to three-dimensions of the approach originally developed to study the diffraction of SH waves (Bouchon, 1985) and P-SV waves (Gaffet and Bouchon, 1989) by two-dimensional topographies. It relies on a boundary integral equation scheme formulated in the frequency domain where the Green functions are evaluated by the discrete wavenumber method. The principle of the method is simple. The diffracted wavefield is represented as the integral over the topographic surface of an unknown source density function times the medium Green functions. The Green functions are expressed as integrals over the horizontal wavenumbers. The introduction of a spatial periodicity of the topography combined with the discretization of the surface at equal intervals results in a discretization of the wavenumber integrals and in a periodicity in the horizontal wavenumber space. As a result, the Green functions are expressed as finite sums of analytical terms. The writing of the boundary conditions of free stress at the surface yields a linear system of equations where the unknowns are the source density functions representing the diffracted wavefield. Finally, this system is solved iteratively using the conjugate gradient approach. We use this method to investigate the effect of a hill on the ground motion produced during an earthquake. The hill considered is 120m high and has an elliptical base and ratios of height-to-half-width of 0.2 and 0.4 along its major and minor axes. The results obtained show that amplification occurs at and near the top of the hill over a broad range of frequencies. For incident shear waves polarized along the short dimension of the hill the amplification at the top reaches 100% around 10Hz and stays above 50% for frequencies between 1.5Hz and 20Hz. For incident shear waves polarized along the direction of elongation of the topography, the maximum amplification

occurs between 2Hz and 5Hz with values ranging from 50% to 75%. The results also show that the geometry of the topography exerts a very strong directivity on the wavefield diffracted away from the hill and that at some distance from the hill this diffracted wavefield consists mostly of Rayleigh waves.

Introduction

Studies of the effect of the irregular topography of the earth surface on seismic waves have been motivated by two types of observations. The first investigations (Tatel, 1954; Gilbert and Knopoff, 1960; Key, 1967; Hudson, 1967; Greenfield, 1971) were stimulated by observations of anomalous arrivals on seismograms recorded in or near regions of rough topography. These investigations led to the identification of these arrivals as energy scattered by the topographic features and consisting mostly of Rayleigh waves. Subsequent investigations (Boore et al., 1981; Bannister et al., 1990; Gupta et al., 1990; Wagner and Langston, 1992; Clouser and Langston, 1995) have confirmed these findings and have shown that topographic scattering is an important source of seismic coda.

Another observation that lent importance to the problem was the recording of extremely high accelerations (at the time the highest ground accelerations ever recorded) at a site located on a topographic ridge during the San Fernando, California, earthquake of 1971. Numerical simulations carried out for the particular configuration of the site concluded that the accelerations recorded had been amplified by the local topography (Boore, 1972; Bouchon, 1973). The interest originally incited by the San Fernando earthquake recordings has since continued. Field experiments have been performed on hills and mountain ridges (Davis and West, 1973; Rogers et al., 1974; Griffiths and Bollinger, 1979, Tucker et al., 1984; Umeda et al., 1986; Carver et al., 1990; Pedersen et al., 1994a; Nechtschein et al., 1995) and they have confirmed that amplification - sometimes quite large - occurs near the top of a hill or mountain and along the crest of a ridge.

Some visual observations made in epicentral areas of strongly felt earthquakes such as the presence of churned and shattered earth at the top of prominences (Muir, 1912; Hadley, 1964; Nason, 1971) and the disruptions of rocks and boulders near hill crests (Oldham, 1899; Clark,

1972; Bolt and Hansen, 1977; Umeda, 1990) also indicate the occurrence of intense shaking in elevated areas of rugged topography. Further interest in this problem was generated by observations of the damage patterns of recent earthquakes like the 1987 Whittier Narrows, California, earthquake (Kawase and Aki, 1990) and the 1989 Loma Prieta earthquake (Ponti and Wells, 1991; Hartzell et al., 1994) and by recordings made during the 1994 Northridge, California, earthquake of extremely high accelerations (1.78g, one of the highest acceleration ever recorded during an earthquake) at a site located on top of a hill (Shakal et al., 1994).

Motivated by all these observations and by the need to include and quantify these effects in seismic risk assessment and microzonation studies, a remarkable amount of work has been done on the theoretical investigation and on the numerical simulation of the diffraction of seismic waves by irregular topographies (Trifunac, 1973; Sabina and Willis, 1975; Wong and Jennings, 1975; Singh and Sabina, 1977; Sills, 1978; Sanchez-Sesma and Rosenblueth, 1979; England et al., 1980; Ilan and Bond, 1981; Bard, 1982; Sanchez-Sesma et al., 1982; Shah et al., 1982; Wong, 1982; Ohtsuki and Harumi, 1983; Sanchez-Sesma, 1983; Zahradnik and Urban, 1984; Bard and Tucker, 1985; Bouchon, 1985; Géli et al., 1988; Kawase, 1988; Gaffet and Bouchon, 1989; Sanchez-Sesma and Campillo, 1991; Pedersen et al., 1994b; Takemiya and Fujiwara, 1994). Laboratory model studies of topographic scattering observed in the field have also been conducted (Rogers et al., 1974; Anooshehpoor and Brune, 1989).

The theoretical and numerical results obtained for ridge type topographies consistently predict the occurrence of amplification at the ridge crest. The levels of amplification calculated, however, almost systematically underestimate the actual amplifications observed in the field. Several hypotheses have been advanced to account for this discrepancy (Griffiths and Bollinger, 1979; Bard, 1982; Bard and Tucker, 1985; Géli et al., 1988; Hartzell et al., 1994). Among them is the two-dimensionality of the topographic geometries assumed in the calculations. Recent field experiments using seismic arrays and conducted at the site where

high accelerations were recorded during the Northridge earthquake emphasize the three-dimensional nature of the seismic response of the hill (Lee et al., 1994; Spudich et al., 1995). The only three-dimensional theoretical investigation reported in the geophysical litterature to date seems to be the study by Sanchez-Sesma (1983) of scattering by an axi-symmetric surface irregularity.

We present in this paper a relatively simple semi-analytical semi-numerical approach to calculate the diffraction of elastic waves by an irregular three-dimensional topography of arbitrary shape. The method relies on a boundary integral equation formulation and on the use of the discrete wavenumber method to evaluate the Green functions. It constitutes the straightforward extension to the 3D case of the method originally developed to study the diffraction of SH waves (Bouchon, 1985) and of P-SV waves (Gaffet and Bouchon, 1989) by 2-dimensional topography.

Description of the method

We consider the problem of a seismic wavefield impinging from below on the surface of an elastic homogeneous half-space. We denote by α, β and ρ the P and S wave velocities and density of the medium and by λ and μ its Lamé coefficients. We define a cartesian coordinate system (x,y,z) in which z is chosen to be the downward vertical direction. Then, the displacement field u at a point $\mathbf{x}$ may be written in the form:

$$u_i(\mathbf{x}) = u_i^o(\mathbf{x}) + \int_S Q_j(s)G_{ij}(\mathbf{x},\mathbf{x}_s)ds \qquad (1)$$

where u^o is the incident source field, $Q_j(s)$ is an unknown source density function, G_{ij} is the medium Green function, S denotes the diffracting surface, and the subscript i indicates the component of displacement considered.

Each point s of the surface acts like a diffracting source of strength $Q_j(s)$ that may be

6

represented as consisting of 3 forces acting along the (x,y,z) directions (Coutant, 1989).

In order to perform the integration expressed by equation (1) we introduce a spatial periodicity in the x and y directions and discretize the surface at equal Δx and Δy intervals. We then first assume that the incident wavefield has a $e^{i\omega t}$ time dependence and express the Green functions G_{ij} in the form of horizontal wavenumber integrals (Lamb, 1904). The spatial periodicity results in a discretization of the wavenumber integrals (Bouchon and Aki, 1977; Bouchon, 1979) while the spatial discretization at constant Δx and Δy intervals implies a periodicity in the horizontal wavenumber domains (Bouchon, 1985; Campillo and Bouchon, 1985). Equation (1) then becomes:

$$u_i(\mathbf{x}) = u_i^0(\mathbf{x}) + \sum_{i_x=1}^{N_x} \sum_{i_y=1}^{N_y} Q_j(i_x, i_y) G_{ij}(\mathbf{x}, \mathbf{x}_{i_x, i_y}) \Delta x \, \Delta y \qquad (2)$$

with, using the displacement potential expressions given in Bouchon (1979),

$$G_{xx} = \frac{-i}{2 L_x L_y \rho \omega^2} \sum_{m_x=-M_x}^{M_x} \sum_{m_y=-M_y}^{M_y} [\frac{k_x^2}{v} e^{-iv|z-z_s|} + \frac{k_y^2 + \gamma^2}{\gamma} e^{-i\gamma|z-z_s|}] e^{-ik_x(x-x_s)} e^{-ik_y(y-y_s)}$$

$$G_{xy} = \frac{-i}{2 L_x L_y \rho \omega^2} \sum_{m_x=-M_x}^{M_x} \sum_{m_y=-M_y}^{M_y} k_x k_y [\frac{e^{-iv|z-z_s|}}{v} - \frac{e^{-i\gamma|z-z_s|}}{\gamma}] e^{-ik_x(x-x_s)} e^{-ik_y(y-y_s)}$$

$$G_{xz} = -i \frac{sgn(z-z_s)}{2 L_x L_y \rho \omega^2} \sum_{m_x=-M_x}^{M_x} \sum_{m_y=-M_y}^{M_y} k_x [e^{-iv|z-z_s|} - e^{-i\gamma|z-z_s|}] e^{-ik_x(x-x_s)} e^{-ik_y(y-y_s)}$$

$$G_{yx} = G_{xy}$$

$$G_{yy} = \frac{-i}{2 L_x L_y \rho \omega^2} \sum_{m_x=-M_x}^{M_x} \sum_{m_y=-M_y}^{M_y} [\frac{k_y^2}{v} e^{-iv|z-z_s|} + \frac{k_x^2 + \gamma^2}{\gamma} e^{-i\gamma|z-z_s|}] e^{-ik_x(x-x_s)} e^{-ik_y(y-y_s)}$$

$$G_{yz} = -i \frac{sgn(z-z_s)}{2 L_x L_y \rho \omega^2} \sum_{m_x=-M_x}^{M_x} \sum_{m_y=-M_y}^{M_y} k_y [e^{-iv|z-z_s|} - e^{-i\gamma|z-z_s|}] e^{-ik_x(x-x_s)} e^{-ik_y(y-y_s)}$$

7

$$G_{zx} = G_{xz}$$

$$G_{zy} = G_{yz}$$

$$G_{zz} = \frac{-i}{2L_x L_y \rho \omega^2} \sum_{m_x=-M_x}^{M_x} \sum_{m_y=-M_y}^{M_y} [\nu e^{-i\nu|z-z_s|} + \frac{k_x^2+k_y^2}{\gamma} e^{-i\gamma|z-z_s|}] e^{-ik_x(x-x_s)} e^{-ik_y(y-y_s)} \qquad (3)$$

with:

$$k_x = \frac{2\pi m_x}{L_x} \; ; \quad k_y = \frac{2\pi m_y}{L_y} \; ; \quad (3a)$$

$$\nu = (\frac{\omega^2}{\alpha^2} - k_x^2 - k_y^2)^{1/2} \, , \, \mathrm{Im}(\nu) \le 0 \; ; \quad \gamma = (\frac{\omega^2}{\beta^2} - k_x^2 - k_y^2)^{1/2} \, , \, \mathrm{Im}(\gamma) \le 0$$

$$sgn\,(z-z_s) = 1 \; \text{for} \; z \ge z_s \, , \quad sgn\,(z-z_s) = -1 \; \text{for} \; z < z_s$$

and where $L_x = N_x \Delta x$ and $L_y = N_y \Delta y$ denote the spatial periodicity lengths in the x and y directions, and $N_x = 2M_x + 1$, $N_y = 2M_y + 1$, implying that N_x and N_y are odd integers. The corresponding stress wavefield may be written

$$\sigma_{pq}(\mathbf{x}) = \sigma_{pq}^o(\mathbf{x}) + \sum_{i_x=1}^{N_x} \sum_{i_y=1}^{N_y} Q_j(i_x,i_y) H_{pqj}(\mathbf{x}, \mathbf{x}_{i_x,i_y}) \Delta x \, \Delta y \qquad (4)$$

with: $\quad H_{pqj} = \lambda \delta_{pq} G_{pj,q} + \mu(G_{pj,q} + G_{qj,p}) \qquad (5)$

where $\delta_{pq} = 1$ for $p = q$, and $\delta_{pq} = 0$ for $p \ne q$, and where $G_{pj,q}$ denotes the derivative of G_{pj} with respect to the q coordinate.

The unknown source densities $Q_j(i_x,i_y)$ are obtained by solving the stress-free boundary conditions at each discretized point (j_x, j_y) of the surface:

$$T_p(j_x,j_y) = n_q(j_x,j_y) \, \sigma_{pq}(\mathbf{x}_{j_x,j_y}) = 0 \qquad (6)$$

where **n** denotes the unit normal to the surface.

Equation (6) is a system of $3N_x N_y$ linear equations which may be rewritten:

$$\sum_{i_x=1}^{N_x} \sum_{i_y=1}^{N_y} [n_q(j_x,j_y) H_{pqj}(\mathbf{x}_{j_x,j_y}, \mathbf{x}_{i_x,i_y}) \Delta x \Delta y] \; Q_j(i_x,i_y) = -n_q(j_x,j_y)\, \sigma_{pq}^o(\mathbf{x}_{j_x,j_y}) \qquad (7)$$

or

$$\sum_{i_x=1}^{N_x} \sum_{i_y=1}^{N_y} C_{pj}(j_x,j_y;i_x,i_y)\, Q_j(i_x,i_y) = -T_p^o(j_x,j_y) \qquad (8)$$

with

$$C_{pj}(j_x,j_y;i_x,i_y) = n_q(j_x,j_y)\, H_{pqj}(\mathbf{x}_{j_x,j_y}, \mathbf{x}_{i_x,i_y}) \Delta x \Delta y \qquad (9a)$$

$$C_{pp}(j_x,j_y;j_x,j_y) = -\frac{1}{2}. \qquad (9b)$$

The expression for $C_{pp}(j_x,j_y;j_x,j_y)$ (equation (9b)) which is independent of the local normal direction is derived by taking $n_z(j_x,j_y)=1$ in equation (9a) as discussed in Bouchon and Coutant (1994).

The right hand side of equation (8) represents (with a change of sign) the incident stress at the surface. Its evaluation is straightforward and can be obtained using the discrete wavenumber method (Bouchon, 1979) if the source is a point source or an extended source. In the case where the source is a vertically propagating S wave of unit spectral amplitude and polarized along the x direction, as will be considered in the next section, the expressions for the incident displacement and stress wavefields are:

$$u_x^o(x,y,z) = e^{i\frac{\omega}{\beta}z}$$

$$\sigma_{pq}^o(x,y,z) = 0 \quad \text{except} \quad \sigma_{xz}^o(x,y,z) = \sigma_{zx}^o(x,y,z) = i\mu\frac{\omega}{\beta} e^{i\frac{\omega}{\beta}z} \qquad (10)$$

$$T_x^o = n_z \sigma_{xz}^o \qquad T_y^o = 0 \qquad T_z^o = n_x \sigma_{zx}^o.$$

In the case where the source is an obliquely propagating plane wave, equation (3a) must be replaced by:

$$k_x = k_x^o + \frac{2\pi m_x}{L_x} \; ; \quad k_y = k_y^o + \frac{2\pi m_y}{L_y} \; ;$$

where k_x^o and k_y^o are the horizontal wavenumber components of the incident wave.

The solution of the system of equations (8) yields the strength and phase of the diffracting sources distribution $Q_j(i_x, i_y)$ from which the wavefield can be evaluated anywhere in the medium using equation (2). The system is solved for each frequency and the solution is multiplied by the spectrum of the source time function of the incident wavefield and Fourier transformed to the time domain. The effect of the periodicity of the structure is removed by using complex frequencies as discussed in Bouchon and Aki (1977) and Bouchon (1979).

The discretization intervals Δx and Δy are determined for each frequency: at low frequencies a minimum number of discretization points N_x and N_y is assumed, insuring that the topographic surface is well defined; as the frequency increases these numbers are defined such that there are at least 2.5 points per seismic wavelength, that is:

$$N_x = 2.5 \times L_x \times \frac{frequency}{\beta}$$

$$N_y = 2.5 \times L_y \times \frac{frequency}{\beta}.$$

As a result, at high frequency, the size of the system increases like the square of the frequency. In order to reduce this size we remove from the matrix equation (8) all the terms which lie below a certain amplitude threshold as discussed in the two-dimensional case by Bouchon et al. (1995) and Schultz et al. (1995), and we invert the resulting sparse system

iteratively using the conjugate gradient method. A test showing the accuracy of the solution obtained with this procedure is presented in the next section.

Effect of a hill

We now use the method to investigate how the topography of a hill affects the seismic ground motion. The topography considered is displayed in Figure 1. The base of the hill is an ellipse of minor and major axes equal to 600m and 1200m. The top of the hill stands at 120m and its flanks have a cosine shape. The size of the model considered (defined by the periodicity lengths in the two horizontal directions) is 2000m by 2000m. The medium P-wave velocity is 3000m/s and the Poisson ratio is 0.25. We first consider the case of a vertically incident shear wave polarized along the minor axis of the ellipse. We assume that this incident wave has a Ricker-pulse time dependence centered about 10Hz. The resulting ground motion produced along the profile that crosses the hill along its minor axis is shown in Figure 2. One observes a clear amplification of the ground motion at and near the top of the hill. The hill also diffracts part of the incoming vertically propagating S-wave into a horizontally propagating P-wave and a Rayleigh wave. Near the bottom of the hill these two diffracted waves have comparable amplitude, but, as distance increases, the Rayleigh wave becomes predominant as the surface P-wave attenuates more rapidly. The ground motion produced along the perpendicular profile that runs along the major axis of the hill is displayed in Figure 3. The results show that there is almost no diffracted wavefield radiated in this direction.

The parameters used in this simulation are as follows: 31 equally spaced frequencies between 0Hz and 30 Hz are considered; below 15Hz all the matrix terms are included, while above 15Hz an amplitude threshold of 1% is applied. The validity of the solution obtained by removing the matrix terms that lie below this amplitude threshold may be estimated by

comparing it to the complete full matrix solution (Figure 4). This comparison is made at 15Hz for the horizontal ground displacement calculated along a profile running from the top of the hill to the edge of the model and following the minor axis of the topography. At this frequency the sparse system retains only 7% of the non-zero terms of the full system.

Snapshots of the horizontal ground displacement are presented in Figure 5. They show the strong directivity that the shape of the topography exerts on the diffracted wavefield: most of the diffracted energy is radiated in the direction perpendicular to the direction of elongation of the topography and, as seen also in Figure 3, only insignificant energy is diffracted in directions close to the direction of elongation. Most of the wavefield diffracted away from the hill has been generated in the summit area of the hill, as is also clearly seen in Figure 2. There is also some energy diffracted by the bottom of the hill but it is much weaker.

In order to assess the amplification of ground motion produced by the hill and investigate its frequency dependence, we computed the spatial variation of the peak horizontal displacement produced for 4 frequencies of excitation (Figure 6). In each case the source is a vertically incident S-wave pulse polarized along the minor axis of the hill. In the first case ($\lambda_S=h$) the center frequency of the pulse is such that its wavelength λ_S is equal to the height h of the hill. In the other cases the center wavelengths of the incident pulse are twice, three times, and four times the height. The peak horizontal displacement is inferred by combining the time traces of the two horizontal displacement components. The results show that amplification occurs at and near the top of the hill at all frequencies considered. This amplification is maximum at the top of the hill. The zone of high amplification is elongated and follows the ridge of the elongated topography. The width of this zone is about proportional to the incident seismic wavelength. The amplification reaches 100% for $\lambda_S=h$, 90% for $\lambda_S=2h$, 70% for $\lambda_S=3h$, and 60% for $\lambda_S=4h$. Some attenuation takes place on the

12

flanks of the hill.

We now investigate the case where the incident S-wave is polarized along the direction of elongation of the topography. The horizontal ground displacement produced along the two perpendicular profiles crossing the hill is displayed in Figure 7. Some amplification still occurs in the summit area of the hill. This amplification, however, is not as strong as the one produced when the incident wave is polarized along the short dimension of the topography. The shape of the topography still exerts the same directivity on the wavefield diffracted away from the hill, no significant energy being radiated in the direction of elongation of the topography. The absence of Rayleigh waves on the profile which runs along the minor axis of the hill is due to a node of radiation of P-waves in this direction.

Maps of corresponding peak horizontal displacements as a function of incident wavelength are presented in Figure 8. Amplification still takes place at or near the top of the hill for the three longest wavelengths considered. The maximum amplification (75%) now occurs at the longest wavelength ($\lambda_S=4h$) and diminishes as the frequency increases (65% at $\lambda_S=3h$, 35% at $\lambda_S=2h$, 0% at $\lambda_S=h$).

In order to investigate more fully the frequency dependence of the topographic amplification, we present in Figure 9 the evolution of the displacement amplitude ratio between the top and the base of the hill as a function of frequency. For incident waves polarized along the elongated direction of the topography, the peak amplification occurs between 2Hz and 5Hz. In this frequency band the ground motion at the top of the hill is amplified by values ranging from 50% to 75%. In contrast almost no amplification occurs for frequencies higher than 10Hz. For motion transverse to the direction of elongation of the hill, the peak amplification occurs around 10Hz where it reaches about 100%. The amplification of the transverse ground motion stays above 50% over a broad frequency range extending from 1.5Hz to 20Hz.

Conclusion

We have presented a semi-analytical semi-numerical method to calculate the diffraction of seismic waves by a three-dimensional topography of arbitrary shape. The formulation relies on a boundary integral equation scheme where the Green function are evaluated by the discrete wavenumber method. The boundary conditions of free stress at the surface lead to a linear system of equations, which is solved iteratively by the conjugate gradient method. We have used this formulation to investigate the effect of a hill on earthquake ground motion. We found that for the configuration studied - the hill is 120m high and its base is an ellipse 1200m in length and 600m in width - amplification occurs at and near the top of the hill over a broad range of frequencies. Amplification levels are the highest for shear waves polarized transversely to the direction of elongation of the hill. The amplification of transverse motions at the top of the hill reaches 100% at 10Hz and stays above 50% between 1.5Hz and 20Hz. For motion along the direction of elongation of the topography, the maximum amplification occurs between 2Hz and 5Hz with values ranging from 50% to 75%. At some distance from the hill the diffracted wavefield consists mostly of Rayleigh waves. The geometry of the hill can exert a drastic directivity on the diffracted wavefield.

Acknowledgements

References

Anooshehpoor, A., and J.N. Brune, Foam rubber modeling of topographic and dam interaction effects at Pacoima Dam, *Bull.Seism.Soc.Am.*, 79, 1347-1360, 1989.

Bannister, S.C., E.S. Husebye, and B.O. Ruud, Teleseismic P coda analysed by three-component array techniques: deterministic location of the topographic P-to-Rg scattering near the NORESS array, *Bull.Seism.Soc.Am.*, 80,1969-1986, 1990.

Bard, P.Y., Diffracted waves and displacement field over two-dimensional topographies, *Geophys.J.Roy.Astr.Soc.*, 71, 731-760, 1982.

Bard, P.Y., and B.E. Tucker, Ridge and tunnel effects: A comparison of observation and theory, *Bull.Seism.Soc.Am.*, 75, 905-922, 1985.

Bolt, B.A., and R.A. Hansen, The upthrow of objects in earthquakes, *Bull. Seism.Soc.Am.*, 67, 1415-1427, 1977.

Boore, D.M., A note on the effect of simple topography on seismic SH waves, *Bull. Seism.Soc.Am.*, 62, 275-284, 1972

Boore, D.M., S.C. Harmsen, and S.T. Harding, Wave scattering from a steep change in surface topography, *Bull.Seism.Soc.Am.*, 71, 117-125, 1981.

Bouchon, M., Effect of topography on surface motion, *Bull.Seism.Soc.Am.*, 63, 615-632, 1973.

Bouchon, M., Discrete wave number representation of elastic wave fields in three-space dimensions, *J.Geophys.Res.*, 84, 3609-3614, 1979.

Bouchon, M., A simple complete numerical solution to the problem of diffraction of SH waves by an irregular surface, *J.Acoust.Soc.Am.*, 44, 1-5, 1985.

Bouchon, M, and K. Aki, Discrete wave-number representation of seismic source wave fields, *Bull.Seism.Soc.Am.*, 67, 259-277, 1977.

Bouchon, M., and O. Coutant, Calculation of synthetic seismograms in a laterally-varying

medium by the boundary element - discrete wavenumber method, *Bull.Seism.Soc.Am.*, 84, 1869-1881, 1994.

Bouchon, M., C.A. Schultz, and M.N. Toksöz, A fast implementation of boundary integral equation methods to calculate the propagation of seismic waves in laterally-varying layered media, *Bull.Seism.Soc.Am.*, submitted, 1995.

Campillo, M., and M. Bouchon, Synthetic SH-seismograms in a laterally varying medium by the discrete wavenumber method, *Geophys.J.Roy.Astr.Soc.*, 83, 307-317, 1985.

Carver, D.L., K.W. King, E. Cranswick, D.W. Worley, P. Spudich, and C. Mueller, Digital recordings of aftershocks of the October 17, 1989, Loma Prieta, California, earthquake: Santa Cruz, Los Gatos, and surroundings areas, *US Geol. Surv. Open–File Report*, 90-683, 1990.

Clark, M.N., Intensity of shaking estimated from displaced stones, *US Geol. Surv. Prof. Paper*, 787, 175-182, 1972.

Clouser, R.H., and C.A. Langston, Modeling observed P-Rg conversions from isolated topographic features near the NORESS array, *Bull.Seism.Soc.Am.*, in press., 1995.

Coutant, O., Numerical study of the diffraction of elastic waves by fluid-filled cracks, *J.Geophys.Res.*, 94, 17805-17818, 1989.

Davis, L.L., and L.R. West, Observed effects of topography on ground motion, *Bull. Seism.Soc.Am.*, 63, 283-298, 1973.

England, R., F.J. Sabina, and I. Herrera, Scattering of SH waves by surface cavities of arbitrary shape using boundary methods, *Phys.Earth Planet.Inter.*, 21, 148-157, 1980.

Gaffet, S., and M. Bouchon, Effects of two-dimensional topographies using the discrete wavenumber - boundary integral equation method in *P–SV* cases, *J.Acoust.Soc.Am.*, 85, 2277-2283, 1989.

Géli, L., P.Y. Bard, and B. Julien, The effect of topography on earthquake ground motion: A review and new results, *Bull.Seism.Soc.Am.*, 78, 42-63, 1988.

Gilbert, F., and L. Knopoff, Seismic scattering from topographic irregularities, *J.Geophys. Res.*, 65, 3437-3444, 1960.

Greenfield, R.J., Short-period P-wave generation by Rayleigh wave scattering at Novaya Zembya, *J.Geophys.Res.*, 76, 7988-8002, 1971.

Griffiths, D.W., and G.A. Bollinger, The effect of appalachian mountain topography on seismic waves, *Bull.Seism.Soc.Am.*, 69, 1081-1105, 1979.

Gupta, I.N., C.S. Lynnes, T.W.McElfresh, and R.A. Wagner, F-k analysis of NORESS array and single-station data to identify sources of near-receiver and near-source scattering, *Bull.Seism.Soc.Am.*, 80, 2227-2241, 1990.

Hadley, J.B., Landslides and related phenomena accompanying the Hebgen Lake earthquake of August 17, 1959, *US Geol. Surv. Prof. Paper*, 435, 107-138, 1964.

Hartzell, S.H., D.L. Carver, and K.W. King, Initial investigation of site and topographic effects at Robinwood ridge, California, *Bull.Seism.Soc.Am.*, 84, 1336-1349, 1994.

Hudson, J.A., Scattered surface waves from a surface obstacle, *Geophys.J.Roy.Astr. Soc.*, 13, 441-458, 1967.

Ilan, A., and L.J. Bond, Interaction of a compressional impulse with a slot normal to the surface of an elastic half space - II, *Geophys.J.Roy.Astr.Soc.*, 65, 75-90, 1981.

Kawase, H., Time-domain response of a semicircular canyon for incident SV, P, and Rayleigh waves calculated by the discrete wavenumber boundary element method, *Bull.Seism.Soc.Am.*, 78, 1415-1437, 1988.

Kawase, H., and K. Aki, Topography effect at the critical SV wave incidence: Possible explanation of damage pattern by the Whittier Narrows, California, earthquake of 1 October 1987, *Bull.Seism.Soc.Am.*, 80, 1-22, 1990.

Key, F.A., Signal-generated noise recorded at the Eskdalemuir seismometer array station, *Bull.Seism.Soc.Am.*, 57, 27-37, 1967.

Lamb, H., On the propagation of tremors at the surface of an elastic solid, *Phil.Trans. Roy.Soc. London, Ser.A*, 203,1-42, 1904.

Lee, W.H.K., R.A. White, D.H. Harlow, J.A. Rogers, and P. Spudich, Digital seismograms of selected aftershocks of the Northridge earthquake recorded by a dense seismic array on February 11, 1994 at Cedar Hill Nursery in Tarzana, California, *US Geol. Surv. Open–File Report*, 94-234, 1994.

Muir, J., The Yosemite, *TheCenturyCo., NewYork*, 1912.

Nason, R.D., Shattered earth at Wallaby Street, Sylmar, *US Geol. Surv. Prof. Paper*, 733, 97-98, 1971.

Nechtschein, S., P.Y. Bard, J.C. Gariel, J.P. Meneroud, P. Dervin, M. Cushing, C. Gaubert, S. Vidal, and A.M. Duval, A topographic effect study in the Nice region, submitted to *Bull.Seism.Soc.Am.*, 1995.

Ohtsuki, A., and K. Harumi, Effect of topography and subsurface inhomogeneities on seismic SV waves, *Earthq.Eng. and Struct.Dyn.*, 11, 441-462, 1983.

Oldham, R.D., Report on the great earthquake of 12 June 1897, *Mem.Geol.Surv.India*, 29, 1899.

Pedersen, H., B. LeBrun, D. Hatzfeld, M. Campillo, and P.Y. Bard, Ground motion amplitude across ridges, *Bull.Seism.Soc.Am.*, 84, 1786-1800, 1994a.

Pedersen, H.A., F.J. Sanchez-Sesma, and M. Campillo, Three-dimensional scattering by two-dimensional topographies, *Bull.Seism.Soc.Am.*, 84, 1169-1183, 1994b.

Ponti, D.J., and R.E. Wells, Off-fault ground ruptures in the Santa Cruz Mountains, California: ridge-top spreading versus tectonic extension during the 1989 Loma Prieta earthquake, *Bull.Seism.Soc.Am.*, 81, 1480-1510, 1991.

Rogers, A.M., L.J. Katz, and T.J. Bennett, Topographic effects on ground motion for incident P waves: A model study, *Bull.Seism.Soc.Am.*, 64, 437-456, 1974.

Sabina, F.J., and J.R. Willis, Scattering of SH waves by a rough half-space of arbitrary slope, *Geophys.J.Roy.Astr.Soc.*, 42, 685-703, 1975.

Sanchez-Sesma, F.J., Diffraction of elastic waves by three-dimensional surface irregularities, *Bull.Seism.Soc.Am.*, 73, 1621-1636, 1983.

Sanchez-Sesma, F.J., and E. Rosenblueth, Ground motion at canyons of arbitrary shape under incident SH waves, *Earthq.Eng. and Struct.Dyn.*, 7,441-450, 1979.

Sanchez-Sesma, F.J., I. Herrera, and J. Avilés, A boundary method for elastic wave diffraction: Application to scattering of SH waves by surface irregularities, *Bull.Seism.Soc.Am.*, 72, 473-490, 1982.

Sanchez-Sesma, F.J., and M. Campillo, Diffraction of P, SV, and Raileigh waves by topographic features: a boundary integral formulation, *Bull.Seism.Soc.Am.*, 81, 2234-2253, 1991.

Schultz, C.A., M. Bouchon, and M.N. Toksöz, Application of boundary integral equations and conjugate gradient methods to elastic wave propagation problems, *Geophysics*, submitted, 1995.

Shah, A.H., K.C. Wong, and S.K. Datta, Diffraction of plane SH waves in a half-space, *Earthq.Eng. and Struct.Dyn.*, 10, 519-528, 1982.

Shakal, A., M. Huang, R. Darragh, T. Cao, R. Sherburne, P. Malhotra, C. Cramer, R. Sydnor, V. Graizer, G. Maldonado, C. Peterson, and J. Wampole, CSMIP Strong motion records from the Northridge, California, earthquake of 17 January 1994, *Report OSMS 94–07, California Division of Mines and Geology, Sacramento, California*, 1994.

Sills, L., Scattering of horizontally polarized shear waves by surface irregularities,

Geophys.J.Roy.Astr.Soc., 54, 319-348, 1978.

Singh, S.K., and F.J. Sabina, Ground-motion amplification by topographic depressions for incident P wave under acoustic approximation, *Bull.Seism.Soc.Am.*, 67, 345-352, 1977.

Spudich, P., M. Hellweg, and W.H.K. Lee, Directional topographic site response at Tarzana observed in aftershocks of the 1994 Northridge, California, earthquake: Implications for main shock motions, *Bull.Seism.Soc.Am.*, submitted, 1995.

Takemiya, H., and A. Fujiwara, SH-wave scattering and propagation analyses at irregular sites by time domain BEM, *Bull.Seism.Soc.Am.*, 84, 1443-1455, 1994.

Tatel, H.E., Note on the nature of a seismogram, 2, *J.Geophys.Res.*, 59, 289-294, 1954.

Trifunac, M.D., Scattering of plane SH waves by a semi-cylindrical canyon, *Earthq.Eng. and Struct.Dyn.*, 1, 267-281, 1973

Tucker, B.E., J.L. King, D. Hatzfeld, and I.L. Nersesov, Observations of hard rock site effects, *Bull.Seism.Soc.Am.*, 74, 121-136, 1984.

Umeda, Y., The bright spot of an earthquake, *Tectonophysics*, 211, 13-22, 1992.

Umeda, Y., A. Kuroiso, K. Ito, Y. Ito, and T. Saeki, High accelerations in the epicentral area of the Western Nagana Prefecture, Japan, earthquake of 1984, *J.Seism.Soc.Japan*, 39, 217-228, 1986.

Wagner, G.S., and C.A. Langston, Body-to-surface-wave scattered energy in teleseismic coda observed at the NORESS seismic array, *Bull.Seism.Soc.Am.*, 82, 2126-2138, 1992.

Wong, H.L., Effect of surface topography on the diffraction of P, SV, and Rayleigh waves, *Bull.Seism.Soc.Am.*, 72, 1167-1183, 1982.

Wong, H.L., and P.C. Jennings, Effects of canyon topography on strong ground motion, *Bull.Seism.Soc.Am.*, 65, 1239-1257, 1975.

Zahradnik, J., and L. Urban, Effect of a simple mountain range on underground seismic

motion, *Geophys.J.Roy.Astr.Soc.*, 79, 167-183, 1984.
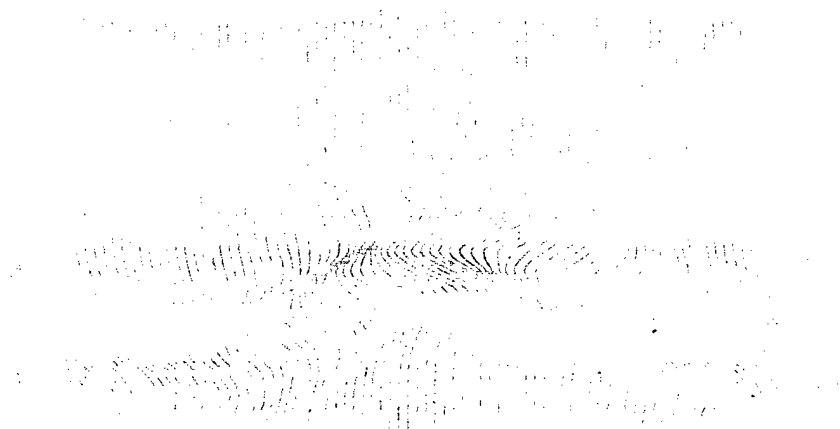
Figure legends

Figure 1

Shape of the topography considered. The distances and heights are expressed in meters and the elevation contour lines are spaced at 10m interval. The hill has an elongated elliptical shape with an aspect ratio of two.

Figure 2

Horizontal (top) and vertical (bottom) displacements produced by a vertically propagating S wave incident on the topography of Figure 1. The shear wave is polarized along the short dimension of the hill and the profile runs along the same direction. A cross-section of the topography is displayed on the left of the figure.

Figure 3

Horizontal displacement produced by a vertically propagating S wave incident on the topography of Figure 1. The shear wave is polarized along the short dimension of the hill while the profile runs along the major axis of the hill. The corresponding topographic cross-section is displayed on the left of the figure.

Figure 4

Comparison in amplitude and phase between the full and the sparse matrix solutions for the horizontal displacement at a frequency of 15Hz. The profile considered runs from the top of the hill to the edge of the model and follows the minor axis of the topography.

Figure 5

Snapshots of the horizontal displacement produced for a vertically incident S pulse polarized along the short dimension of the topography. The component of displacement

displayed is the one parallel to the incident polarization direction. The time sequence is indicated and the time interval between successive frames is 1/32s. The incident pulse is a Ricker wavelet with a center period of 0.138s, corresponding to a wavelength equal to twice the hill height. The first seven snapshots are dominated by the primary incident pulse which illuminates the topography. The elliptic base of the hill is visible on snapshot 6. The last nine snapshots show the diffracted wavefield being generated mostly in the summital area of the hill and propagating away from the hill.

Figure 6

Maps showing the spatial distribution of horizontal displacement amplitude for four different frequencies of excitation. λ_S denotes the shear wavelength, and h is the height of the topography. The dotted line indicates the base of the hill.

Figure 7

Horizontal ground motion produced along two profiles running parallel to the major (top) and minor (bottom) axes of the hill for a vertically incident S wave polarized along the elongated dimension of the topography. The corresponding topographic cross-sections are displayed on the left of the figure.

Figure 8

Maps showing the spatial distribution of horizontal displacement amplitude for four different frequencies of excitation. λ_S denotes the shear wavelength, and h is the height of the topography. The dotted line indicates the base of the hill.

Figure 9

Amplitude ratio between the ground motions at the top and at the base of the hill in the case of incident shear waves polarized along directions parallel and transverse to the direction

of elongation of the topography. The reference point at the base of the hill is chosen at some distance from the hill so as not to be affected by the presence of the hill.

TOPOGRAPHY
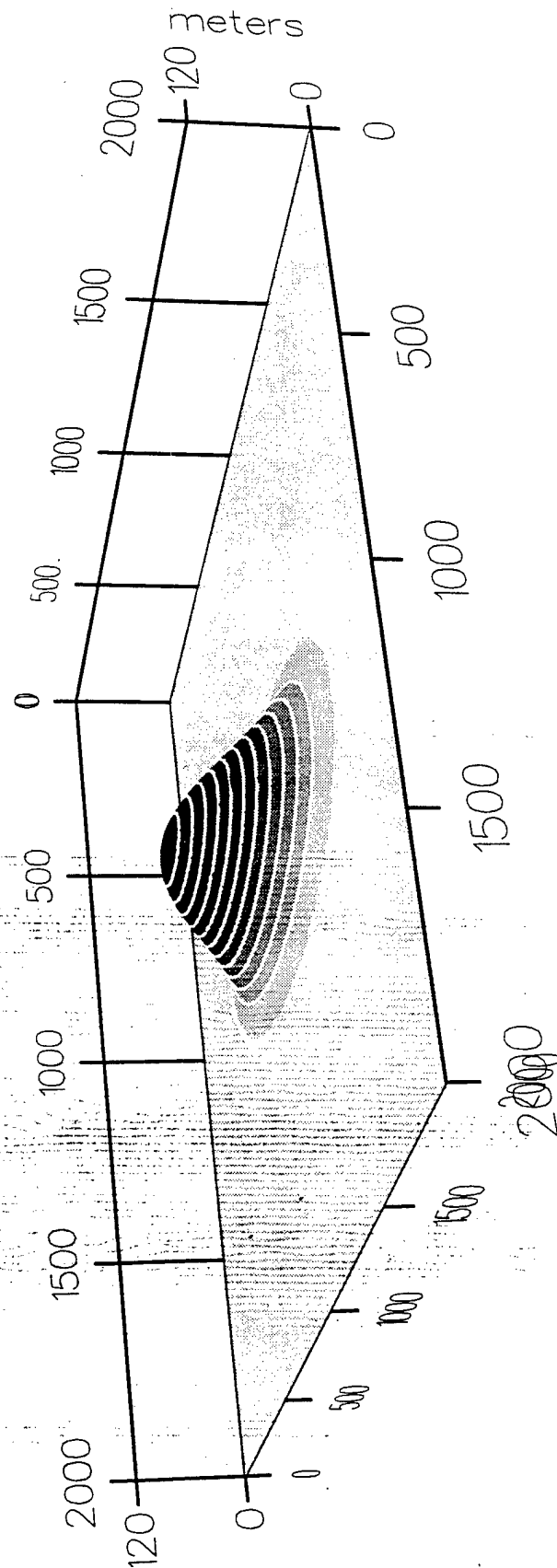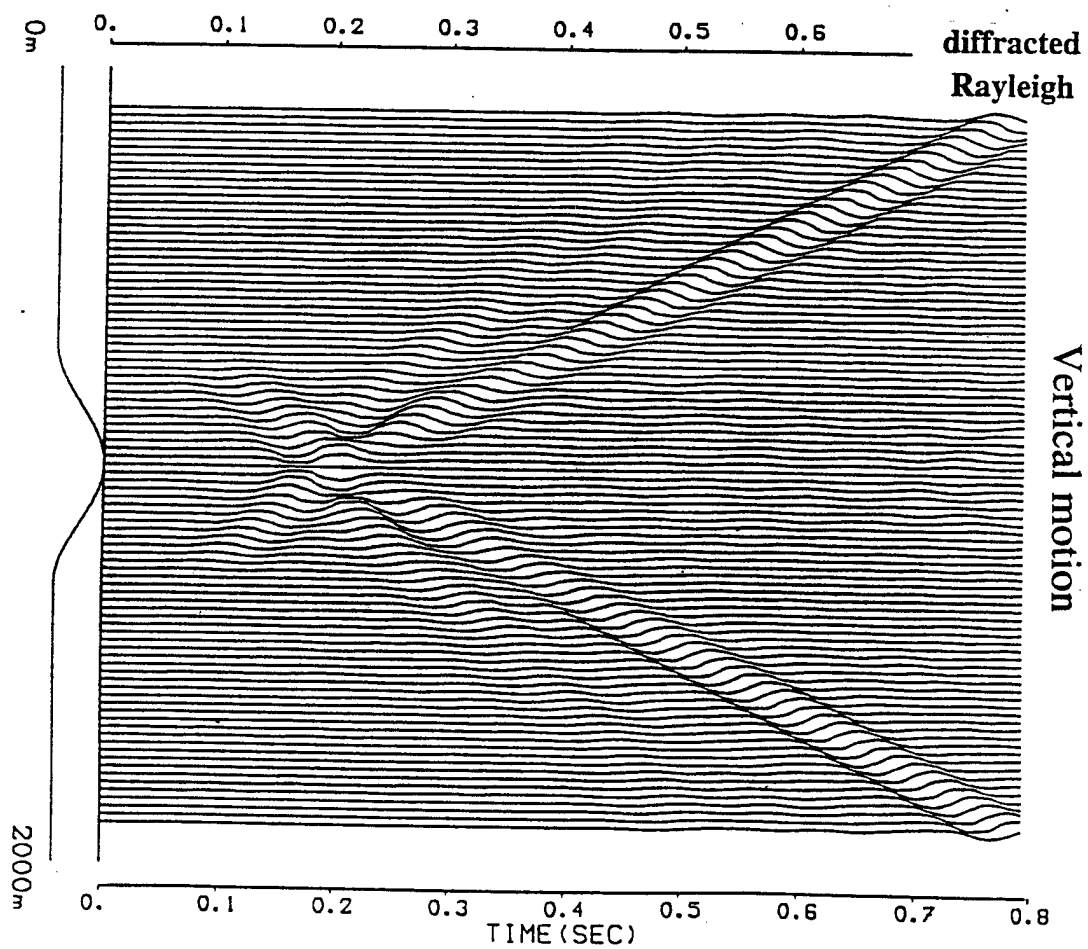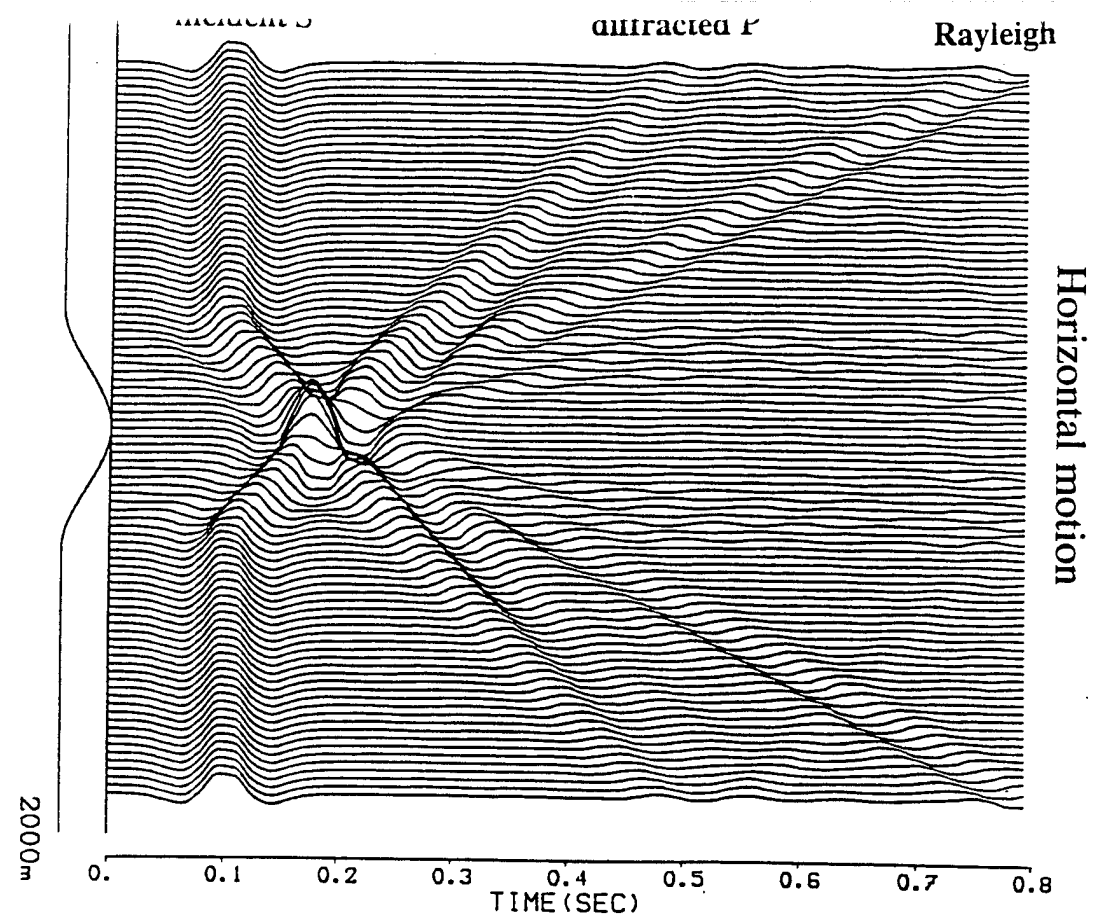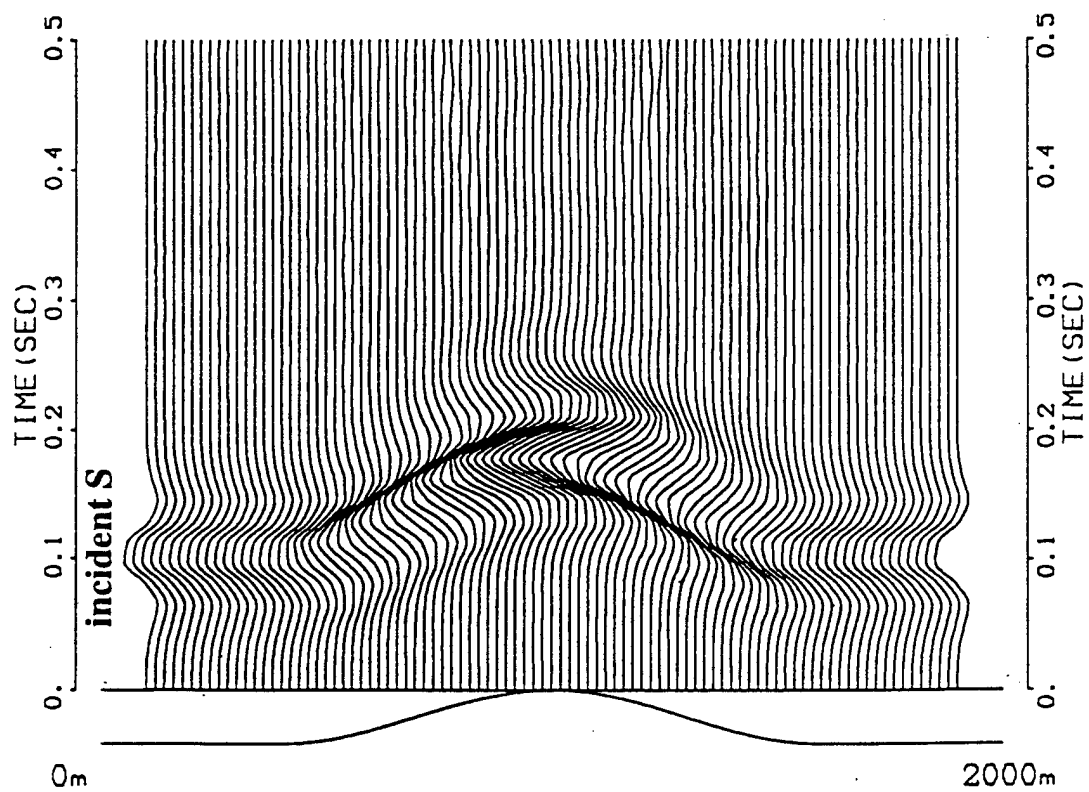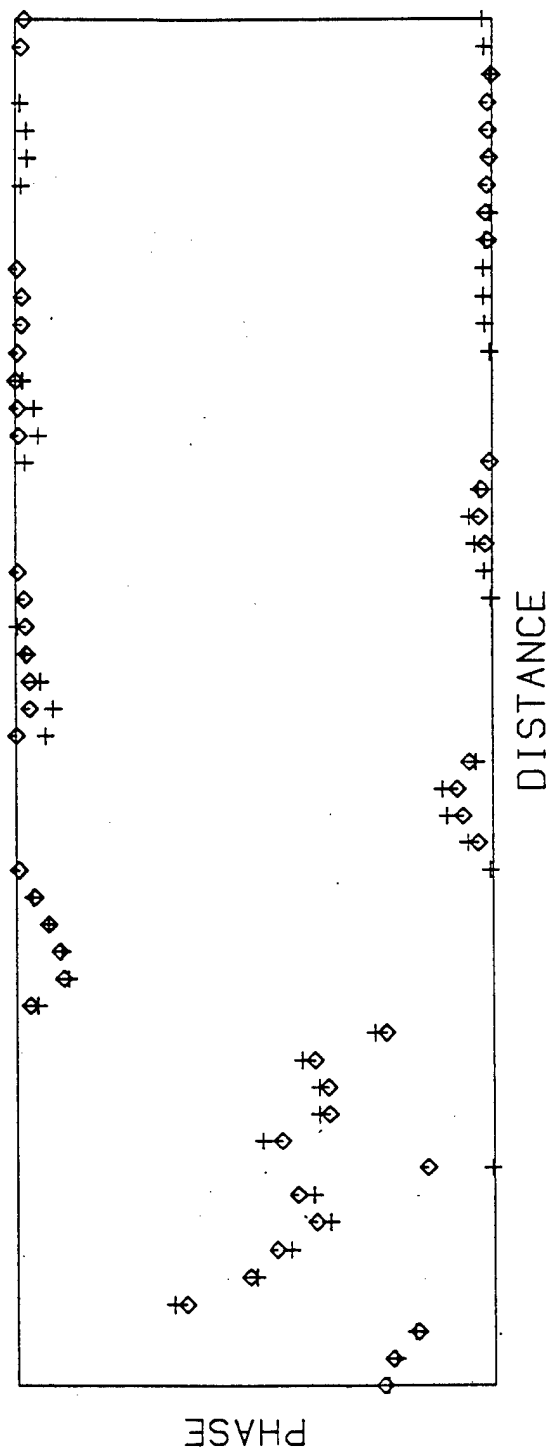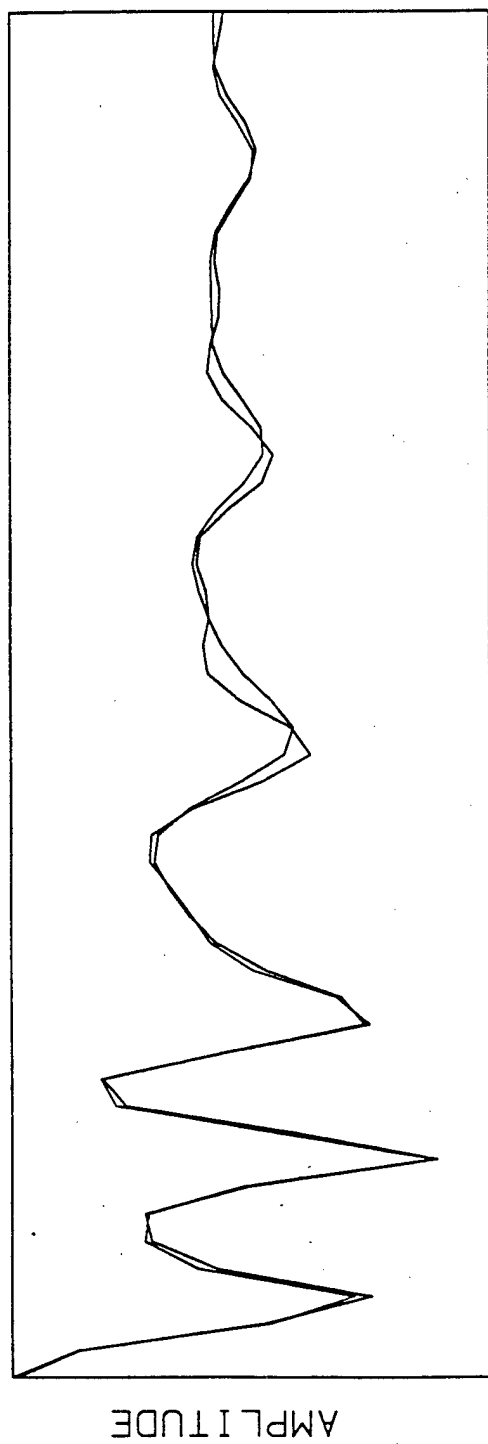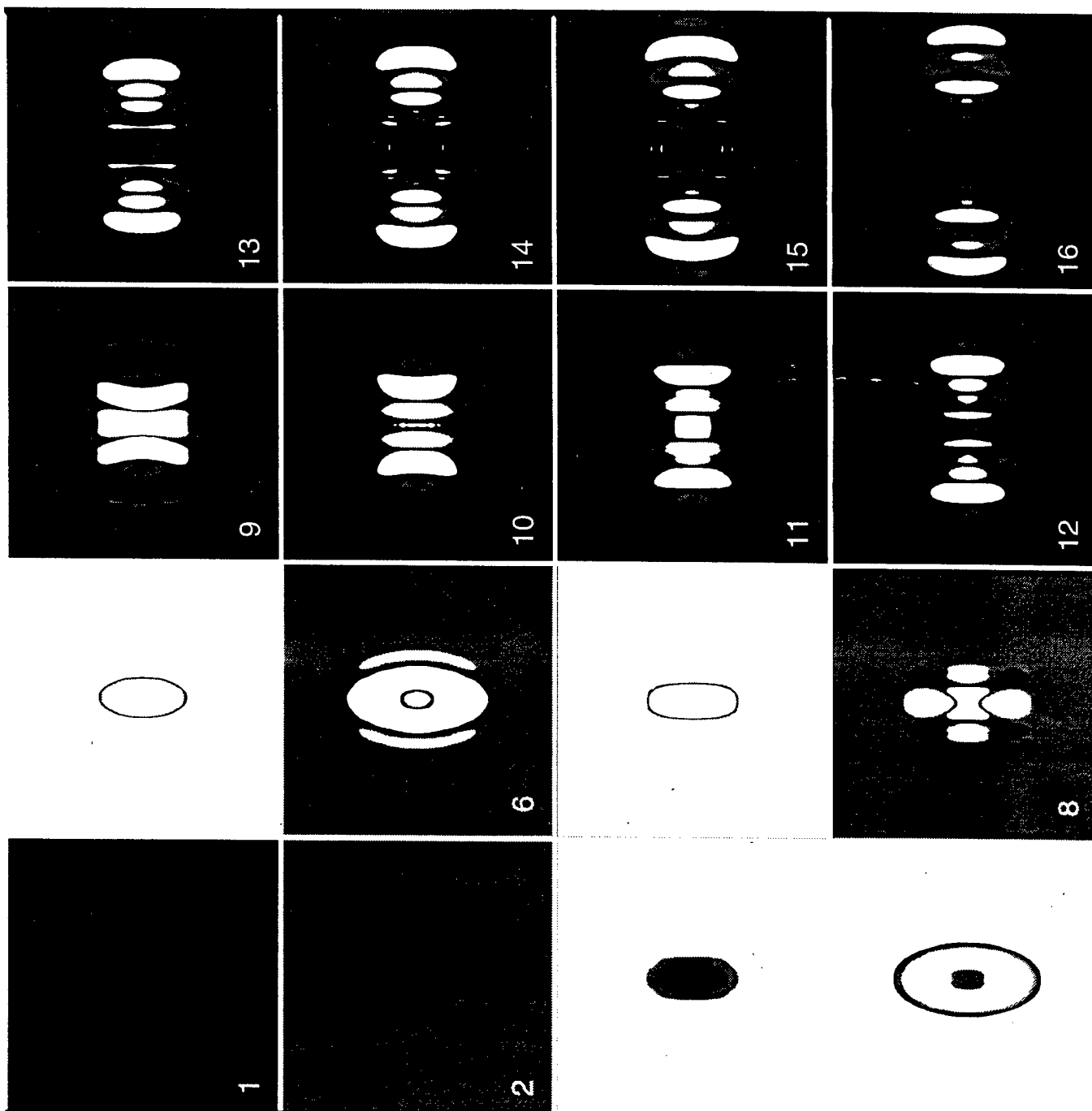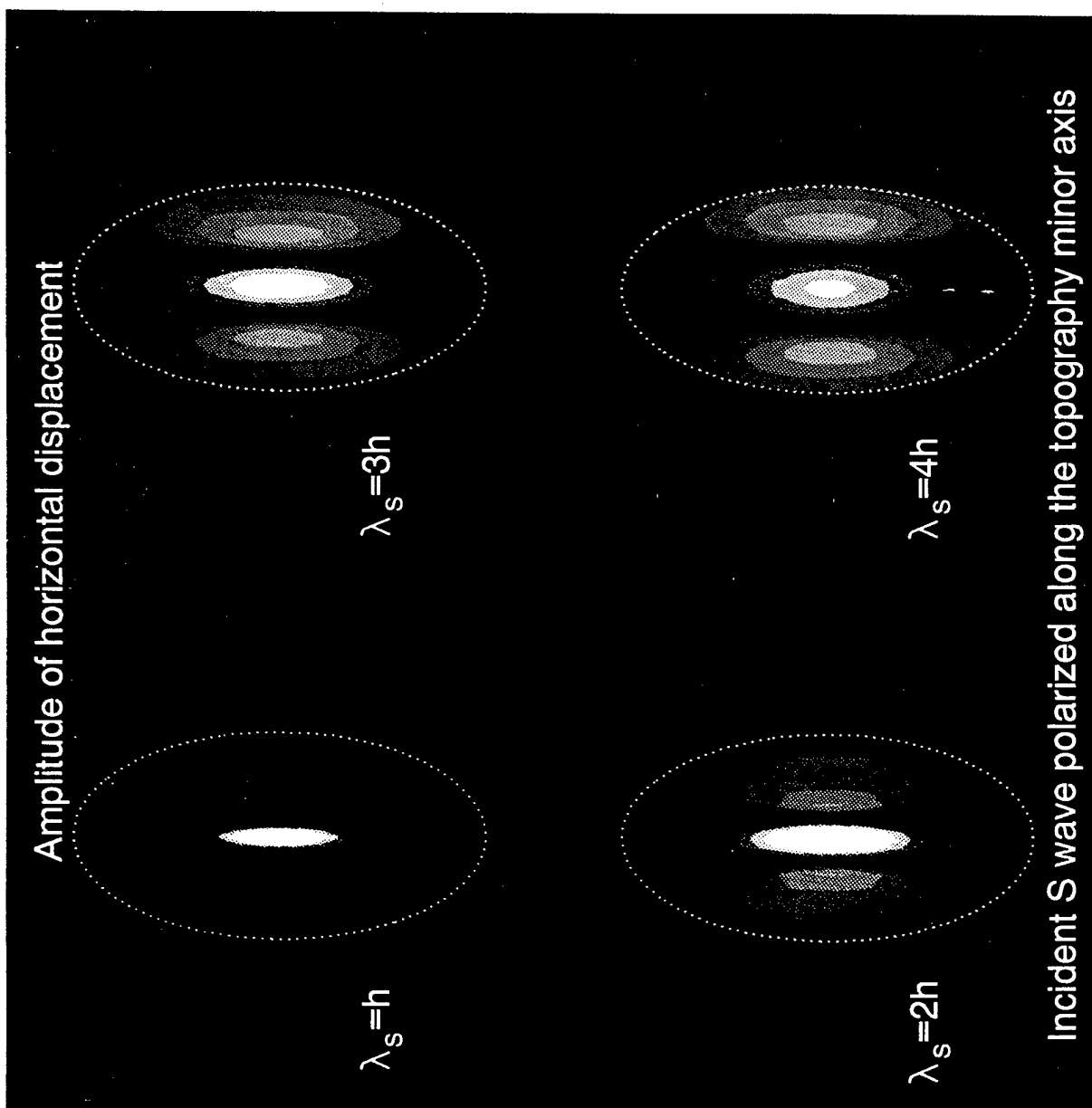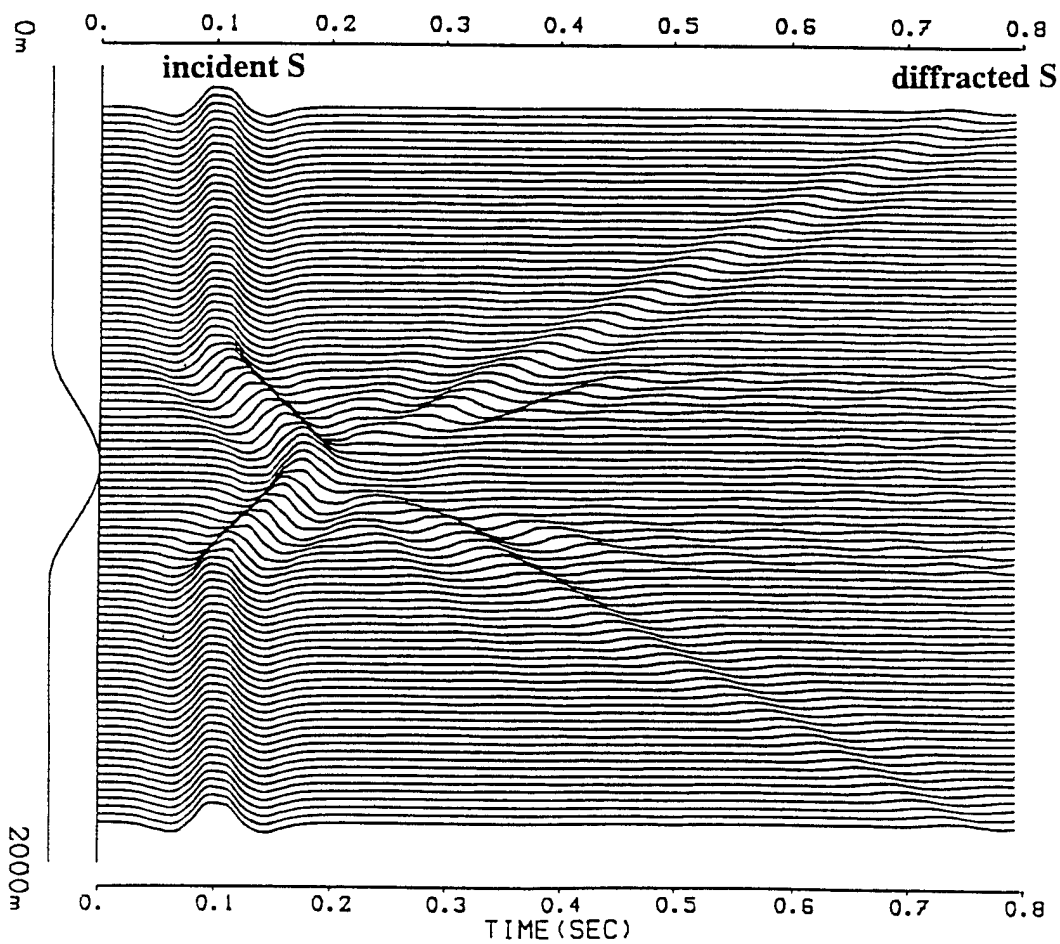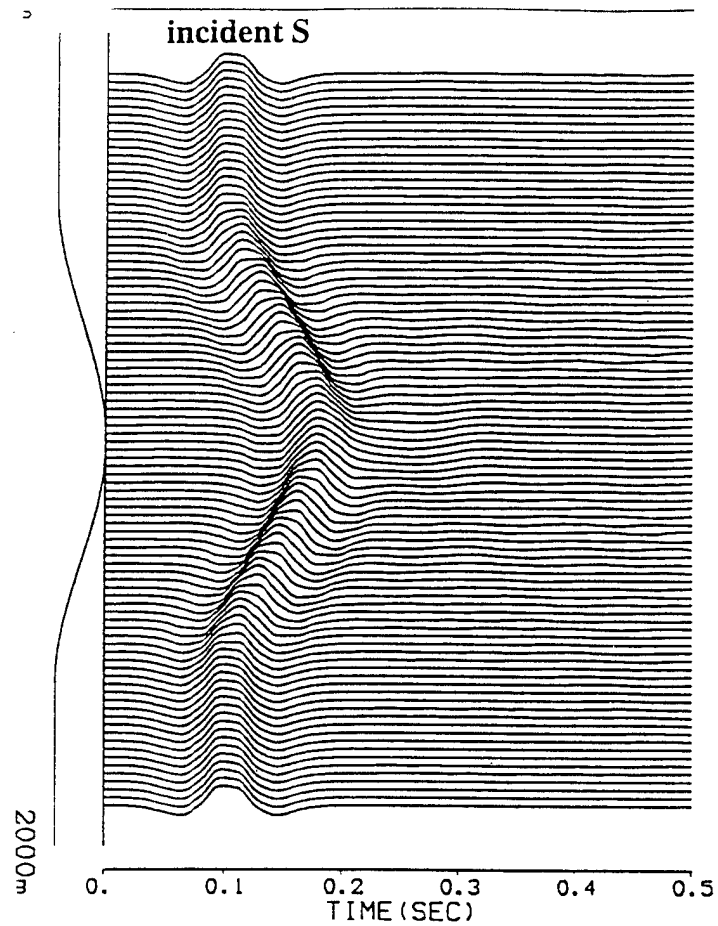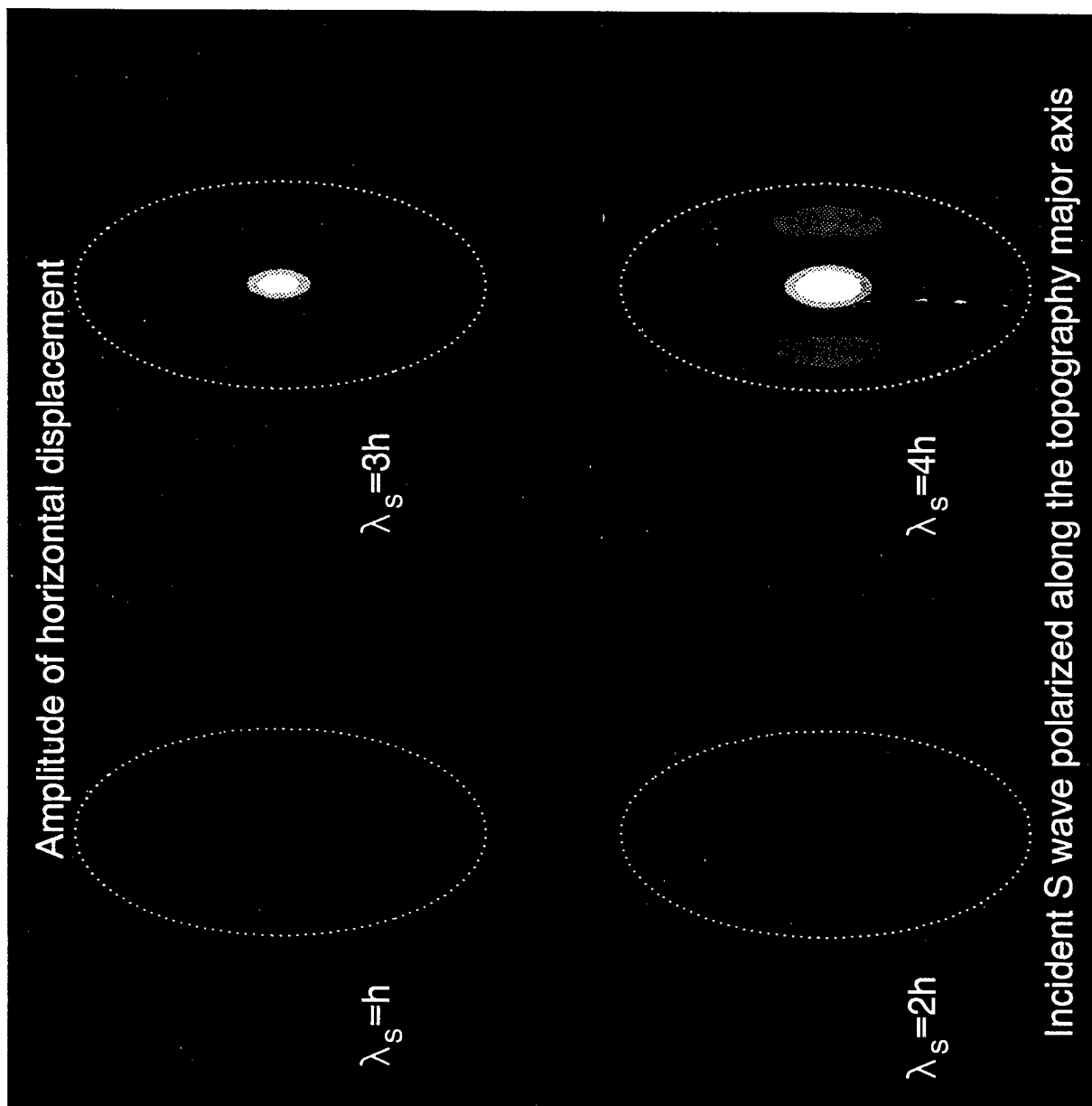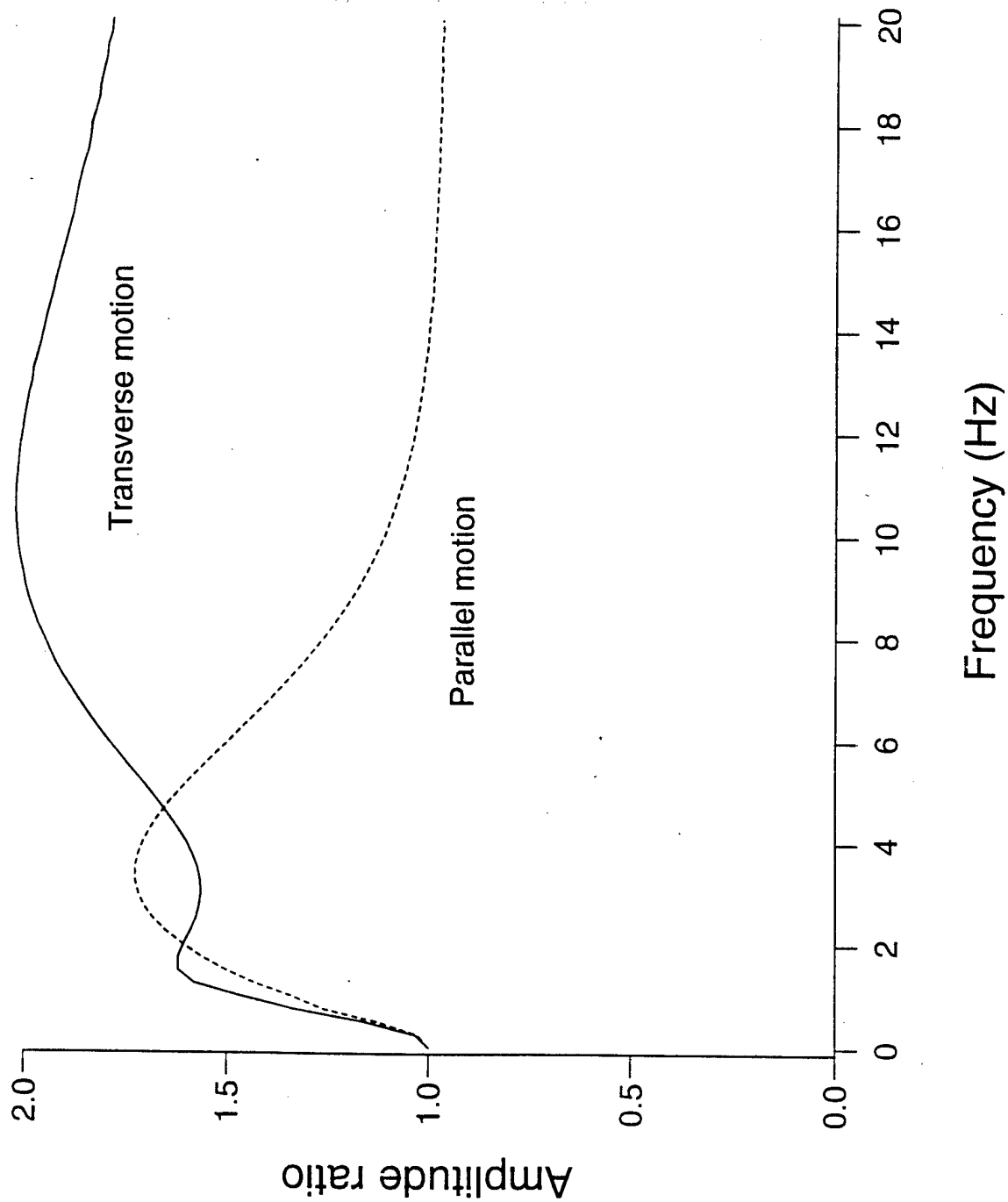
meters

Figure 1

26

Figure 2

incident S   diffracted P   Rayleigh

Horizontal motion

TIME (SEC)

diffracted
Rayleigh

Vertical motion

TIME (SEC)

27

Horizontal motion

28

Figure 3

AMPLITUDE

PHASE

DISTANCE

29

Figure 4

Figure 5

30

Amplitude of horizontal displacement

Incident S wave polarized along the topography minor axis

31

incident S

diffracted S

TIME (SEC)

TIME (SEC)

2000m

0m

2000m

Figure 7

Amplitude of horizontal displacement

$\lambda_s = h$

$\lambda_s = 3h$

$\lambda_s = 2h$

$\lambda_s = 4h$

Incident S wave polarized along the topography major axis

33

top/base

Figure 9

Amplitude ratio

Frequency (Hz)

Transverse motion

Parallel motion

A fast implementation of boundary integral equation methods

to calculate the propagation of seismic waves

in laterally-varying layered media

by

Michel Bouchon [1,2] , Craig A Schultz [1], and M. Nafi Toksöz [1]

[1] Earth Resources Laboratory

Massachusetts Institute of Technology

Cambridge, MA 02139

[2] Laboratoire de Géophysique Interne et Tectonophysique

Université Joseph Fourier

BP 53X, 38041 Grenoble, France

Abstract

We present a boundary integral equation / conjugate gradient formulation to study the propagation of seismic waves through complex geological structures. The method is aimed at extending the range of applications of boundary integral equations or boundary elements methods to geological models of relatively large size or complexity. We show that the system of equations which expresses the boundary conditions at the medium interfaces and which is inherent to the biem or bem approach can be drastically reduced in size and that only 10 to 20% of the terms of this system contribute significantly to the solution. The boundary conditions may thus be expressed in the form of a very sparse linear system which can be inverted iteratively by the conjugate gradient method. We use this approach to investigate the effect of a sedimentary layer of varying thickness on local and regional seismic wave propagation. We show that the amplitude of ground motion and the duration of shaking are drastically increased when the sediment/bedrock interface is rough and irregular relatively to the case where it is flat.

Introduction

In recent years several methods using boundary integral equations or boundary elements have been developed to calculate the propagation of seismic waves through complex geological structures (e.g. Sanchez-Sesma and Esquivel, 1979; Dravinski, 1983; Bouchon, 1985; Campillo and Bouchon, 1985; Campillo, 1987; Bravo et al., 1988; Kawase, 1988; Coutant, 1989; Kawase and Aki, 1989; Gaffet and Bouchon, 1989, 1991; Papageorgiou and Kim, 1991; Sanchez-Sesma and Campillo, 1991; Mossessian and Dravinski, 1992; Schultz and Toksöz, 1993; Pedersen et al., 1994). One common feature of these techniques is that they require the solution of a linear system of equations which expresses the boundary conditions and which, when applied to real cases, can be very large. The size of this system is indeed the most limiting factor in the applicability of the method.

The aim of the present study is to investigate ways of reducing the size of the system of linear equations inherent to the boundary integral equations formulation. We shall show that this can be achieved simply by removing from the equations the Green function terms which lie below a certain amplitude threshold and which do not contribute significantly to the solution. We shall limit the scope of this study to the case of SH waves and we shall present an application of the method to regional seismic wave propagation.

Irregular surface topography

We begin the presentation with a rather simple case which involves a plane SH wave vertically incident on an irregular topography. Denoting by x and z the horizontal and vertical axes, the reflected and diffracted displacement wavefield, at a particular frequency ω, may be written in the form of an integral over the surface S of a source density function q times the medium Green function G, that is:

$$V(x,z) = \int_S q(s) G(x,z;x_s,z_s) ds \quad (1)$$

Using the discrete wavenumber method to evaluate the Green function (Bouchon and Aki, 1977) and discretizing the surface at equal Δx interval along the x-axis, equation (1) may be expressed in the form (Bouchon, 1985):

$$V(x,z) = \frac{1}{2\mu L} \sum_{j=1}^{N} Q_j \sum_{m=-N/2}^{N/2} \frac{e^{-i\gamma_m |z-z_j|} e^{-ik_m(x-x_j)}}{i\gamma_m} \quad (2)$$

with:

$$k_m = \frac{2\pi m}{L},$$

$$\gamma_m = \left(\frac{\omega^2}{\beta} - k_m^2\right)^{1/2}, \quad Im(\gamma_m) \leq 0 .$$

and where μ is the shear modulus, β is the shear wave velocity, L is the required periodicity length of the surface topography, and where the Q_j are the unknown strengths of the antiplane forces located at the discretized points (x_j,z_j) of the surface. These forces represent the sources of the scattered wavefield. In this formulation, the surface is assumed to have a periodic shape. In practice this periodicity length (like the size of the model in finite-differences methods) is chosen large enough so that repeated topographies do not affect the time domain solution. N is the number of discretized points and is required to be an odd integer. The discretization interval $\Delta x = \frac{L}{N}$ is set according to the wavelength considered.

The unknown strengths Q_j of the forces are determined by matching the boundary conditions of free stress at each one of the surface points. In order to write down the corresponding equations, let us denote by V_{ij} and σ_{ij} the displacement and surface stress produced at a point i of the surface by the surface force distribution element Q_j acting at point

j. We have, using the discrete wavenumber formalism of equation (2) and denoting by n_x and n_z the x and z components of the normal to the surface:

$$V_{ij} = \frac{Q_j}{2\mu L} \sum_{m=-N/2}^{N/2} \frac{e^{-i\gamma_m|z_i-z_j|}e^{-ik_m(x_i-x_j)}}{i\gamma_m} \qquad (3)$$

$$\sigma_{ij} = \mu(n_{x_i}\frac{dV_{ij}}{dx_i} + n_{z_i}\frac{dV_{ij}}{dz_i}) \qquad (4)$$

that is:

$$\sigma_{ij} = -\frac{Q_j}{2L} \sum_{m=-N/2}^{N/2} [n_{x_i}\frac{k_m}{\gamma_m} + sgn(z_i-z_j)n_{z_i}]e^{-i\gamma_m|z_i-z_j|}e^{-ik_m(x_i-x_j)} \qquad (5a)$$

with $sgn(z_i-z_j)=1$ for $z_i \geq z_j$, $=-1$ for $z_i < z_j$.

When i=j the derivation expressed by equation (4) is undefined and equation (5a) must be replaced by (Bouchon and Coutant, 1994):

$$\sigma_{ii} = -\frac{Q_i}{2}\frac{N}{L} \qquad (5b)$$

Let us now consider the case where a vertically monochromatic plane SH wave is incident upon the surface. The incident displacement and stress at a point i of the surface may be written in the form:

$$V_{oi} = e^{i\frac{\omega}{\beta}z_i}$$

and   (6)

$$\sigma_{oi} = i\frac{\mu}{\beta}n_{z_i}\omega e^{i\frac{\omega}{\beta}z_i}$$

39

The boundary conditions require that the stress associated with the scattered wave field cancells the incident stress along the surface, that is:

$$\sum_{j=1}^{N} \sigma_{ij} = -\sigma_{oi} \text{ , for } i=1,N \qquad (7)$$

which may be written in matrix form:

$$C \, Q = F \qquad (8)$$

with:

$$C_{ij} = -\frac{1}{2L} \sum_{m=-N/2}^{N/2} [n_{x_i} \frac{k_m}{\gamma_m} + sgn\,(z_i - z_j) n_{z_i}] e^{-i\gamma_m|z_i - z_j|} e^{-ik_m(x_i - x_j)} \qquad \text{for } i \neq j$$

$$C_{ii} = -\frac{1}{2} \frac{N}{L}$$

$$F_i = -\sigma_{oi} \, .$$

The amplitude of the C matrix elements is largest for the diagonal terms and, on average, decreases with increasing $[i-j]$ separation.

In order to investigate whether all the terms of the matrix are necessary to yield an accurate solution, we performed the inversion of the system after retaining only the high amplitude terms of the matrix. This makes C a sparse matrix and mostly retains the terms closest to the diagonal. We then use the conjugate gradient method to invert the now sparse linear system. A description of the conjugate gradient method and the corresponding software can be found in Press et al. (1994). A comparison of the results obtained with the corresponding full matrix inversion is presented in Figure 1. The topography considered is a 200m high hill with a cosine shape and a base length of 800m. The shear wave velocity is

1000m/s. A vertically propagating Ricker-type SH pulse with 5Hz center frequency is incident on the surface. The periodicity length chosen is 4000m. The calculation is done for a time window length T of 2s and over 32 frequencies starting at 0Hz and spaced at equal $\Delta f = \dfrac{1}{T}$ interval. Characteristic of the discrete wavenumber method and later removed from the time domain solution, a constant imaginary part equal to $-i\dfrac{\pi}{T}$ is added to the angular frequency. The number of discretized points N is equal to 201.

The traces displayed in the bottom half of Figure 1 are the results of the full matrix inversion. They correspond to receivers located along the topography, from the top of the hill to 2000m away from the summit. These seismograms are compared with those shown in the upper half of the figure which are obtained by retaining only 15% of the matrix elements C_{ij}. In this case the removal of elements is achieved using a simple amplitude criterion: Only the 15% elements with the highest amplitude are kept. The 15% threshold used here is somewhat arbitrary but it shows that a good solution is reached by retaining only the high amplitude terms of the matrix. Doing so reduces drastically the size of the system of equations and results in a considerable gain in memory space and computer time.

Laterally-varying layered medium

Let us now consider the case of a multilayered medium where the shape of the interfaces is irregular. If we denote by $Q^t(l)$ and $Q^b(l)$ the unknown force distributions respectively at the top and at the bottom of layer l, and by $S^t(l)$ and $S^b(l)$ the eventual source displacement-stress vectors incident respectively on the top and bottom interfaces of layer l, the boundary conditions of continuity of displacement and stress across the interface separating layer l (above) from layer $l+1$ (below) may be written:

$$\sum_{j=1}^{N} a_{ij}^{bt}(l)\, Q_j^t(l) + \sum_{j=1}^{N} a_{ij}^{bb}(l)\, Q_j^b(l) + S_i^b(l) = \sum_{j=1}^{N} a_{ij}^{tt}(l+1)\, Q_j^t(l+1) + \sum_{j=1}^{N} a_{ij}^{tb}(l+1)\, Q_j^b(l+1) + S_i^t(l+1)$$

for $i=1,2N$ (9)

where the $a_{ij}(l)$ are the displacement and stress Green functions for medium l. The superscript bt indicates that the point of evaluation of the field (first index) is at the bottom of the layer while the point of application of the force (second index) is at the top of the layer, and so on.

Thus, using the discrete wavenumber formalism described above, we have:

$$a_{ij}(l) = \frac{1}{2\mu_l L} \sum_{m=-N/2}^{N/2} \frac{e^{-i\gamma_m |z_i - z_j|} e^{-ik_m(x_i - x_j)}}{i\gamma_m}$$

$$a_{i+N,j}(l) = -\frac{1}{2L} \sum_{m=-N/2}^{N/2} [n_{x_i} \frac{k_m}{\gamma_m} + sgn\,(z_i - z_j) n_{z_i}] e^{-i\gamma_m |z_i - z_j|} e^{-ik_m(x_i - x_j)} \quad \text{for } i \neq j$$

$$a_{i+N,i}(l) = -\frac{1}{2}\frac{N}{L}$$

for $i=1,N$; $j=1,N$ (10)

with:

$$\gamma_m = (\frac{\omega^2}{\beta_l} - k_m^2)^{1/2}, \; Im(\gamma_m) \leq 0$$

$sgn\,(z_i - z_j) = 1$ for $z_i \geq z_j$, $=-1$ for $z_i < z_j$, for a^{tt}, a^{bt}

$sgn\,(z_i - z_j) = 1$ for $z_i > z_j$, $=-1$ for $z_i \leq z_j$, for a^{bb}, a^{tb}

Let us consider the case where the free surface is flat and located at $z=0$. The boundary conditions at the bottom of the first layer may then be expressed:

$$\sum_{j=1}^{N} d_{ij}^{bb}(l) Q_j^b(1) + S_i^b(1) = \sum_{j=1}^{N} a_{ij}^{tt}(2) Q_j^t(2) + \sum_{j=1}^{N} a_{ij}^{tb}(2) Q_j^b(2) + S_i^t(2) \quad (11)$$

where d_{ij}^{bb} are the half-space displacement and stress Green functions for medium 1, that is, in discrete wavenumber form:

$$d_{ij}^{bb}(1) = \frac{1}{2\mu_1 L}\sum_{m=-N/2}^{N/2} \frac{[e^{-i\gamma_m|z_i-z_j|}+e^{-i\gamma_m(z_i+z_j)}]}{i\gamma_m}e^{-ik(x_i-x_j)}$$

$$d_{i+N,j}^{bb}(1) = -\frac{1}{2L}\sum_{m=-N/2}^{N/2}[(n_{x_i}\frac{k_m}{\gamma_m}+sgn\,(z_i-z_j)n_{z_i})e^{-i\gamma_m|z_i-z_j|} + (n_{x_i}\frac{k_m}{\gamma_m}+n_{z_i})e^{-i\gamma_m(z_i+z_j)}]e^{-ik_m(x_i-x_j)},$$

$i \neq j$

$$d_{i+N,i}^{bb}(1) = -\frac{1}{2}\frac{N}{L}(1+n_{z_i}e^{-2i\gamma_m z_i})$$

for $i=1,N$, $j=1,N$.

Equations (9) and (11) lead to a linear system of the form:

$$C\,Q = F \qquad (12)$$

where, denoting by nl the number of layers:

$$C = \begin{bmatrix} A^{bb}(1) & -A^{tt}(2) & -A^{tb}(2) & 0 & 0 & 0 & \dots\dots\dots \\ 0 & A^{bt}(2) & A^{bb}(2) & -A^{tt}(3) & -A^{tb}(3) & 0 & 0 \quad \dots\dots \\ \dots\dots\dots\dots\dots\dots\dots\dots\dots\dots\dots\dots \\ \dots\dots\dots\dots\dots\dots\dots\dots\dots\dots 0 & A^{bt}(nl-1) & A^{bb}(nl-1) & -A^{tt}(nl) \end{bmatrix}$$

and

$$F = \begin{bmatrix} S^t(2)-S^b(1) \\ S^t(3)-S^b(2) \\ \dots\dots\dots\dots\dots \\ S^t(nl)-S^b(nl-1) \end{bmatrix}$$

The dimension of the linear system expressed by equation (12) is $2N\text{x}(nl-1)$. The number of discretized points N representing each interface varies with the frequency considered. At low

frequencies, this number is set to a minimum value, and, as the frequency increses, its value is chosen such that there are at least 2.5 points per seismic wavelength, that is:

$$N = 2.5 \times L \times \frac{frequency}{minimum\ wave\ velocity} \qquad (13)$$

In general, a different value of N is defined for each interface, according to the minimum shear wave velocity in the surrounding layers. The 2.5 points per seismic wavelength criterion arises from tests of accuracy performed for the configurations considered in this study.

Because of the linear dependency of N on distance and frequency, numerical simulations of high frequency seismic wave propagation over long distance ranges cannot be attempted through a straighforward inversion of equation (12), as the inversion of the complete system using classical methods would be prohibitive. Thus we proceed as for the topography case. After normalization, we retain only the largest terms of the Green function matrix C and use the conjugate gradient method to solve the resulting sparse system. The configuration studied is displayed at the bottom of Figure 2. The medium consists of a three-layers crust overlying a mantle half-space. In this simulation we investigate the effect that a highly irregular subsurface topography between sediments and bedrock has on ground motion. For this reason we assume that the other two interfaces are flat although they are similarly treated in the boundary integral equation scheme. The source is a line of shear dislocation across a vertical fault plane perpendicular to the laterally-varying structure and located at a depth of 10km. The source displacement-stress wavefield incident on the top and bottom interfaces of the source layer l_s, expressed in discrete wavenumber form, is given by:

$$S_i^{t,b}(l_s) = V_{oi} = \frac{M_o}{2\mu L} \sum_{m=-N/2}^{N/2} \frac{k_m}{\gamma_m} e^{-i\gamma_m |z_i - z_o|} e^{-ik_m(x_i - x_o)}$$

and (14)

$$S^{t,b}_{i+N}(l_s) = \sigma_{oi} = -\frac{iM_o}{2L}\sum_{m=-N/2}^{N/2} k_m[n_{x_i}\frac{k_m}{\gamma_m}+sgn\,(z_i-z_o)n_{z_i}]e^{-i\gamma_m|z_i-z_o|}e^{-ik_m(x_i-x_o)}$$

where M_o is the source seismic moment and (x_o, z_o) denote the source coordinates.

Equations (14) are obtained by derivation of equations (3) and (5a) with respect to x_o after replacing the index j of the diffracting source by the primary source index o.

In order to make sure that, like for the topography case, the size of the system can be reduced and still yield a good solution, we compare in Figure 2 the surface displacement obtained by full matix inversion with the one calculated by retaining only the largest terms of the matrix. We choose as a criterion - rather arbitrarily - to eliminate all the matrix elements which have an amplitude smaller than 1% of the amplitude of the largest term in the row (which is the diagonal element). We perform this comparison at a frequency of 2Hz, which is the median value of the frequency range considered.

As the agreement between the two solutions is satisfactory, we extend this 1% amplitude threshold criterion to all frequency calculations above 2Hz. Below 2Hz we choose to retain the full matrix as the size of the system is then small enough to carry out the full system inversion. The results obtained are showed in Figure 3a. They display the horizontal ground velocity in the direction tangential to the plane of propagation. The source has a step-like time dependence and the frequency range considered extends from 0Hz to 4Hz. The periodicity length is $L=275$km. The number of elements considered at each frequency is showed in Figure 4. At low frequencies a minimum number corresponding to a minimum discretization interval Δx of 1km designed to provide an accurate representation of the interfaces geometry is assumed. The abrupt change of curve beyond 2Hz corresponds to the application of the threshold criterion. At the highest frequency only 12% of the non-zero elements of the matrix are utilized to calculate the solution.

In order to assess the effect of the irregular sediments-basement topography on the ground motion we also simulated the case where this interface is flat. The results are displayed in Figure 3b. The configuration is the same as the one simulated in Figure 3a except that the sediment thickness is constant and equal to 2km. The calculation is performed with the same parameters as in Figure 3a, but with the plane layers reflection and transmission coefficients. The differences between the two simulations are quite dramatic. The change from a flat basement topography to an irregular one considerably enhances the ground motion, particularly the duration of ground shaking. The irregular shape of the interface diffracts the organized incoming seismic energy into rays which travel in all directions. Many of these rays stay trapped in the sediments where they give rise to surface waves which propagate laterally across the sedimentary structures as has been shown in several numerical simulation experiments (Bard and Bouchon, 1980a,b; Hill and Levander,1984; Levander and Hill, 1985; Benz and Smith, 1988; Chavez-Garcia and Bard, 1989; Hill et al., 1990; Papageorgiou and Kim, 1991; Gaffet and Bouchon, 1991; Frankel and Vidale, 1992; Graves and Clayton, 1992; Kawase and Sato, 1992; Frankel, 1993; Jongmans and Campillo, 1993). One such train of Love waves can be clearly seen propagating forward in the basin closest to the source, then being reflected at the edge of the basin and propagating backward across it before being reflected again at the other edge. Likewise, much of the surface seismic motion over the basins can be attributed to Love waves. Between the basins, in the regions of bedrock outcrops, the seismic motion is greatly reduced, before the amplitudes pick up again in the next basin. This pattern is strikingly similar to the one observed by Hanks (1975) and Liu and Heaton (1984) and subsequently studied by Vidale and Helmberger (1988) on recordings of the San Fernando earthquake made across the San Fernando and the Los Angeles basins, although in that case Rayleigh waves play the role held by Love waves in our study.

The case where the deeper crustal interfaces are also irregular is displayed in Figure 5.

The velocity and density of the layers as well as the shape of the sediment/bedrock interface are the same as in the previous example, but the upper crustal discontinuity and the Moho are now also irregular. All three interfaces are represented by the same number of discretized points as in the previous case and the same amplitude threshold criterion is applied. The resulting surface motion resembles the one calculated in Figure 3a, indicating that the surface motion is much more sensitive to the topography of the sediment/bedrock interface than to the shape of the deeper crustal and crust/mantle discontinuities. In order to assess the effect of removing the low-amplitude terms of the matrix system for this configuration, we compare in Figure 6 the seismograms obtained by inverting the full matrix with those obtained by retaining all the matrix terms up to 1Hz and removing the ones below a 1% amplitude threshold between 1Hz and 4Hz. Here again the agreement is quite satisfactory for many applications.

Conclusion

We have tried to extend the range of applications of seismic wave propagation problems which can be studied using boundary integral equation formulation by reducing the size of the linear system which expresses the boundary conditions and which is usually the factor which limits the extent and the complexity of the geological models which can be investigated. We have shown that only the 10 to 20% highest amplitude terms of the system are important to obtain a good solution. The removal of the other terms does not significantly affect the results. The inversion of the very sparse system is then performed iteratively using the conjugate gradient approach. As an application of the method, we have shown the drastic effect that an irregular sediment/bedrock interface has on the amplitude and duration of seismic ground shaking.

Acknowledgements

References

Bard, P.Y., and M. Bouchon (1980a). The seismic response of sediment-filled valleys. Part 1. The case of incident SH waves, Bull. Seism. Soc. Am. 70, 1263-1286.

Bard, P.Y., and M. Bouchon (1980b). The seismic response of sediment-filled valleys. Part 2. The case of incident P and SV waves, Bull. Seism. Soc. Am. 70, 1921-1941.

Benz, H.M., and R.B. Smith (1988). Elastic-wave propagation and site amplification in the Salt Lake Valley, Utah, from simulated normal faulting earthquakes, Bull. Seism. Soc. Am. 78, 1851-1874.

Bouchon, M. (1985). A simple complete numerical solution to the problem of diffraction of SH waves by an irregular surface, J. Acoust. Soc. Am. 44, 1-5.

Bouchon, M, and K. Aki (1977). Discrete wavenumber representation of seismic source wave fields, Bull. Seism. Soc. Am. 67, 259-277.

Bouchon, M., and O. Coutant (1994). Calculation of synthetic seismograms in a lateraly-varying medium by the boundary element - discrete wavenumber method, Bull. Seism. Soc. Am., in press.

Bravo, M.A., F.J. Sanchez-Sesma, and F.J. Chavez-Garcia (1988). Ground motion on stratified alluvial deposits for incident SH waves, Bull. Seism. Soc. Am. 78, 436-450.

Campillo, M. (1987). Lg wave propagation in a laterally varying crust and the distribution of the apparent quality factor in central France, J. Geophys. Res. 92, 12604-12614.

Campillo, M., and M. Bouchon (1985). Synthetic SH seismograms in a laterally varying medium by the discrete wavenumber method, Geophys. J. Roy. Astr. Soc. 83, 307-317.

Chavez-Garcia, F.J., and P.Y. Bard (1989). Effect of random thickness variations

on the seismic response of a soft soil layer: Applications to Mexico City, in Engineering Seismology and Site Response, A.S. Cakmak and I. Herrera (Editors), Computational Mechanics Publications, Southampton, 247-261.

Coutant, O. (1989). Numerical study of the diffraction of elastic waves by fluid-filled cracks, J. Geophys. Res. 94, 17805-17818.

Dravinski, M. (1983). Scattering of plane harmonic SH wave by dipping layers of arbitrary shape, Bull. Seism. Soc. Am. 73, 1303-1319.

Frankel, A. (1993). Three-dimensional simulations of ground motions in the San Bernardino Valley, California, for hypothetical earthquakes on the San Andreas fault, Bull. Seism. Soc. Am. 83, 1020-1041.

Frankel, A., and J. Vidale (1992). A three-dimensional simulation of seismic waves in the Santa Clara Valley, California, from a Loma Prieta aftershock, Bull. Seism. Soc. Am., 82, 2045-2074.

Gaffet, S., and M. Bouchon (1989). Effects of two-dimensional topographies using the discrete wavenumber - boundary integral equation method in $P-SV$ cases, J. Acoust. Soc. Am. 85, 2277-2283.

Gaffet, S., and M. Bouchon (1991). Source location and valley shape effects on the P-SV displacement field using a boundary integral equation - discrete wavenumber representation method, Geophys. J. Int. 106, 341-355.

Graves, R.W., and R.W. Clayton (1992). Modeling path effects in three-dimensional basin structures, Bull. Seism. Soc. Am., 82, 81-103.

Hanks, T.C. (1975). Strong ground motion of the San Fernando, California, earthquake: Ground displacements, Bull. Seism. Soc. Am. 65, 193-225.

Hill, J., H. Benz, M. Murphy, and G. Schuster (1990). Propagation and resonance of SH waves in the Salt Lake Valley, Utah, Bull. Seism. Soc. Am. 80, 23-42.

Hill, N.R., and A.R. Levander (1984). Resonances of low-velocity layers with lateral variations, Bull. Seism. Soc. Am. 74, 521-537.

Jongmans, D., and M. Campillo (1993). The response of the Ubaye Valley (France) for incident SH and SV waves: Comparison between measurements and modeling, Bull. Seism. Soc. Am. 83, 907-924.

Kawase, H. (1988). Time-domain response of a semicircular canyon for incident SV, P, and Rayleigh waves calculated by the discrete wavenumber boundary element method, Bull. Seism. Soc. Am. 78, 1415-1437.

Kawase, H., and K. Aki (1989). A study of the response of a soft basin for incident S, P, and Rayleigh waves with special reference to the long duration observed in Mexico City, Bull. Seism. Soc. Am. 79, 1361-1382.

Kawase, H., and T. Sato (1992). Simulation analysis of strong motions in the Ashigara Valley considering one- and two-dimensional geologic structures, J. Phys. Earth 40, 27-56.

Levander, A.R., and N.R. Hill (1985). P-SV resonances in irregular low-velocity surface layers, Bull. Seism. Soc. Am. 75, 847-864.

Liu, H.L., and T. Heaton (1984). Array analysis of the ground velocities and accelerations from the 1971 San Fernando, California, earthquake, Bull. Seism. Soc. Am. 74, 1951-1968.

Mossessian, T.K., and M. Dravinski (1992). A hybrid approach for scattering of elastic waves by three-dimensional irregularities of arbitrary shape, J. Phys. Earth 40, 241-261.

Papageorgiou, A.S., and J. Kim (1991). Study of the propagation and amplification of seismic waves in Caracas Valley with reference to the 29 July 1967 earthquake: SH waves, Bull. Seism. Soc. Am. 81, 2214-2233.

Pedersen, H.A., F.J. Sanchez-Sesma, and M. Campillo (1994). Three-dimensional

scattering by two-dimensional topographies, Bull. Seism. Soc. Am. 84, 1169-1183.

Press, W.H., B.P. Flannery, S.A. Teukolsky, and W.T. Vetterling (1994).

Numerical recipes, Cambridge University Press, Cambridge.

Sanchez-Sesma, F.J., and J. Esquivel (1979). Ground motion on alluvial valleys

under incident plane SH waves, Bull. Seism. Soc. Am. 69, 1107-1120.

Sanchez-Sesma, F.J., and M. Campillo (1991). Diffraction of P, SV, and Raileigh

waves by topographic features: a boundary integral formulation, Bull. Seism. Soc. Am.

81, 2234-2253.

Schultz, C.A., and M.N. Toksöz (1993). Enhanced backscattering of seismic waves

from a highly irregular, random interface: SH case, Geophys. J. Int. 114, 91-102.

Vidale, J.E., and D.V. Helmberger (1988). Elastic finite-difference modeling of

the 1971 San Fernando, California erathquake, Bull. Seism. Soc. Am. 78, 122-141.

Figure legends

Figure 1

Ground motion produced by a SH pulse vertically incident on a hill-shaped topography. The upper half of the figure corresponds to the sparse matrix solution while the lower half displays the full matrix solution.

Figure 2

Source-medium configuration considered and corresponding amplitude and phase of the surface displacement at 2Hz. The source location is indicated by the star. The curves (amplitude) and symbols (phase) display the comparison between the full matrix solution and the 1% amplitude threshold solution.

Figure 3

(a) Ground horizontal velocity produced by an antiplane dislocation for the crustal model of Figure 2. The epicentral distance range extends from 0 to 100km. A reduced velocity of 3600m/s is applied to the traces. (b) Same as (a) when the sediment/bedrock interface is flat.

Figure 4

Number of elements considered as a function of frequency for the calculation of Figure 3a.

Figure 5

Ground horizontal velocity produced by an antiplane dislocation and corresponding crustal model. The epicentral distance range extends from 0 to 100km. A reduced velocity of 3600m/s is applied to the traces.

Figure 6

Comparison of ground velocity time histories calculated by inverting the full matrix with those obtained after removing the terms which lay below a 1% amplitude threshold for frequencies between 1Hz and 4Hz. The crustal structure geometry is the one depicted in Figure 5. Only the shape of the upper crustal discontinuities is shown here.
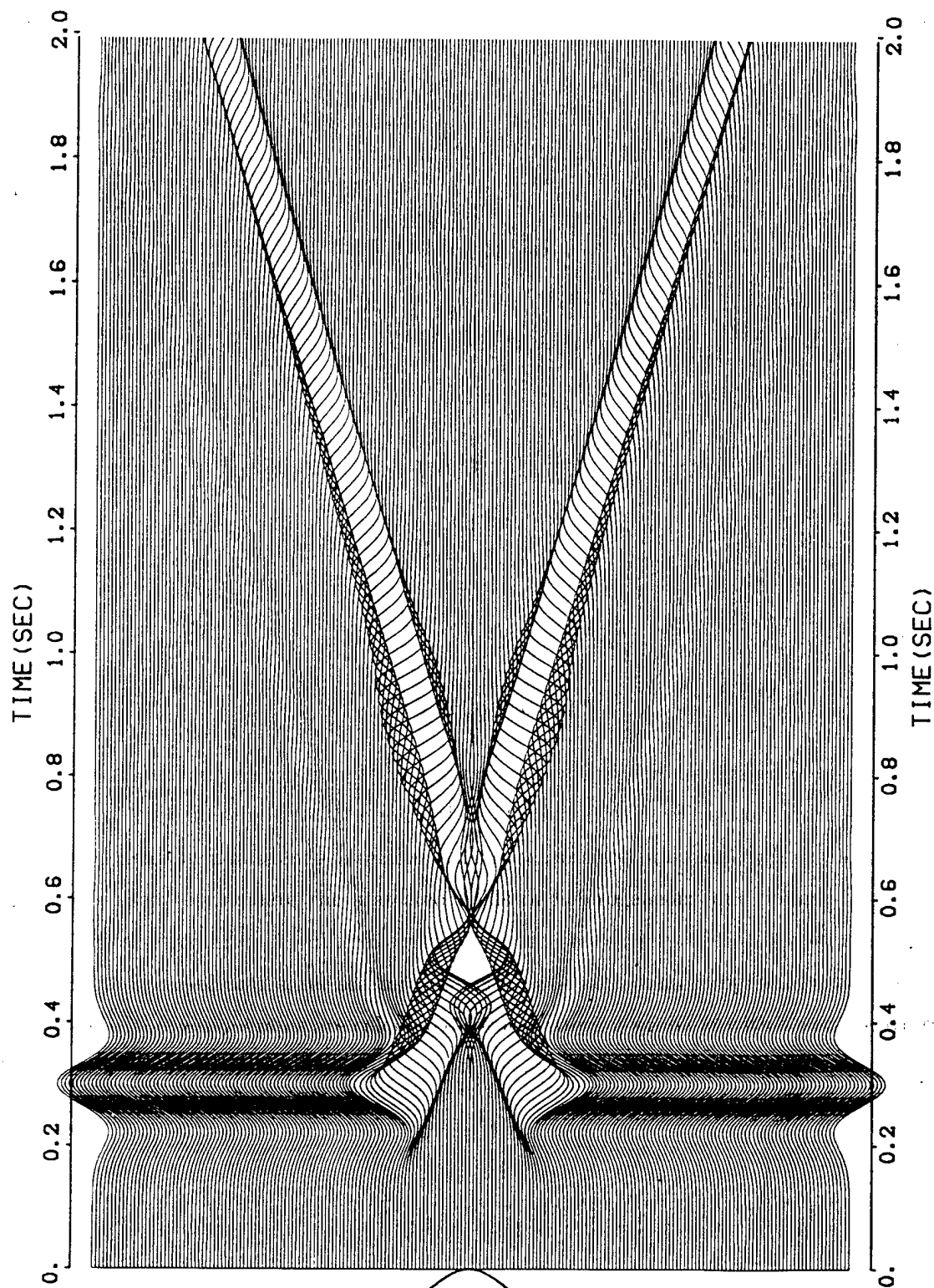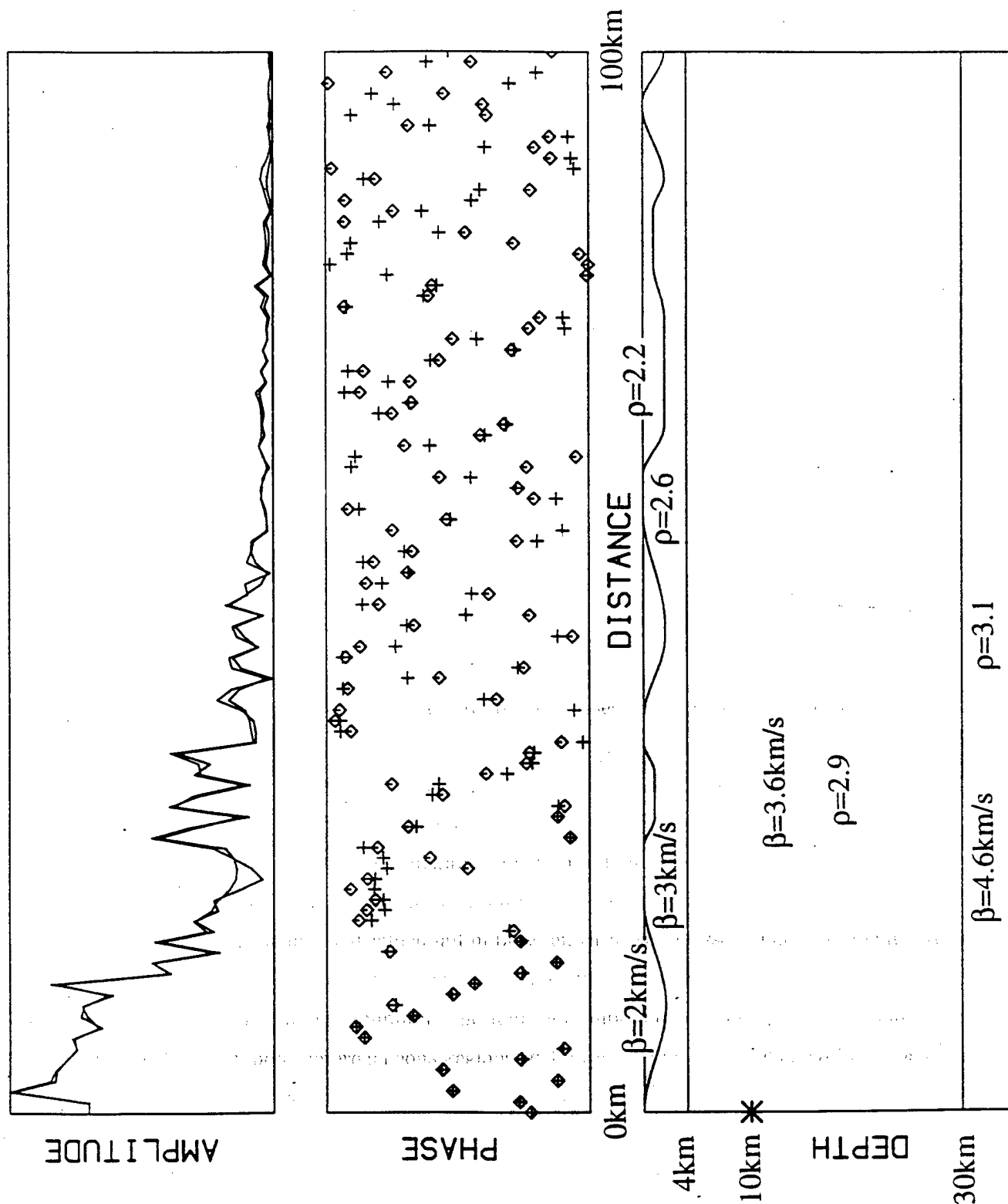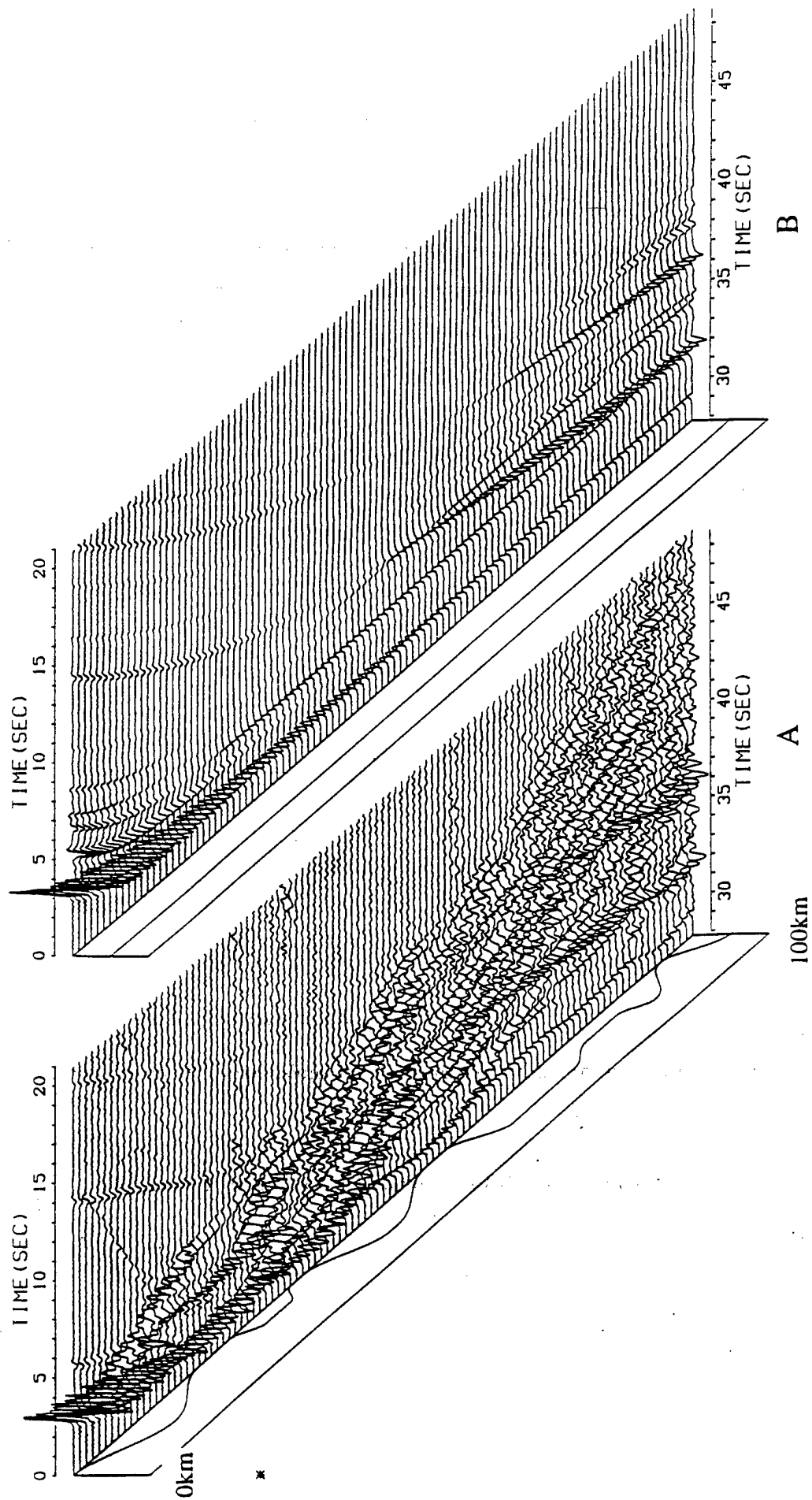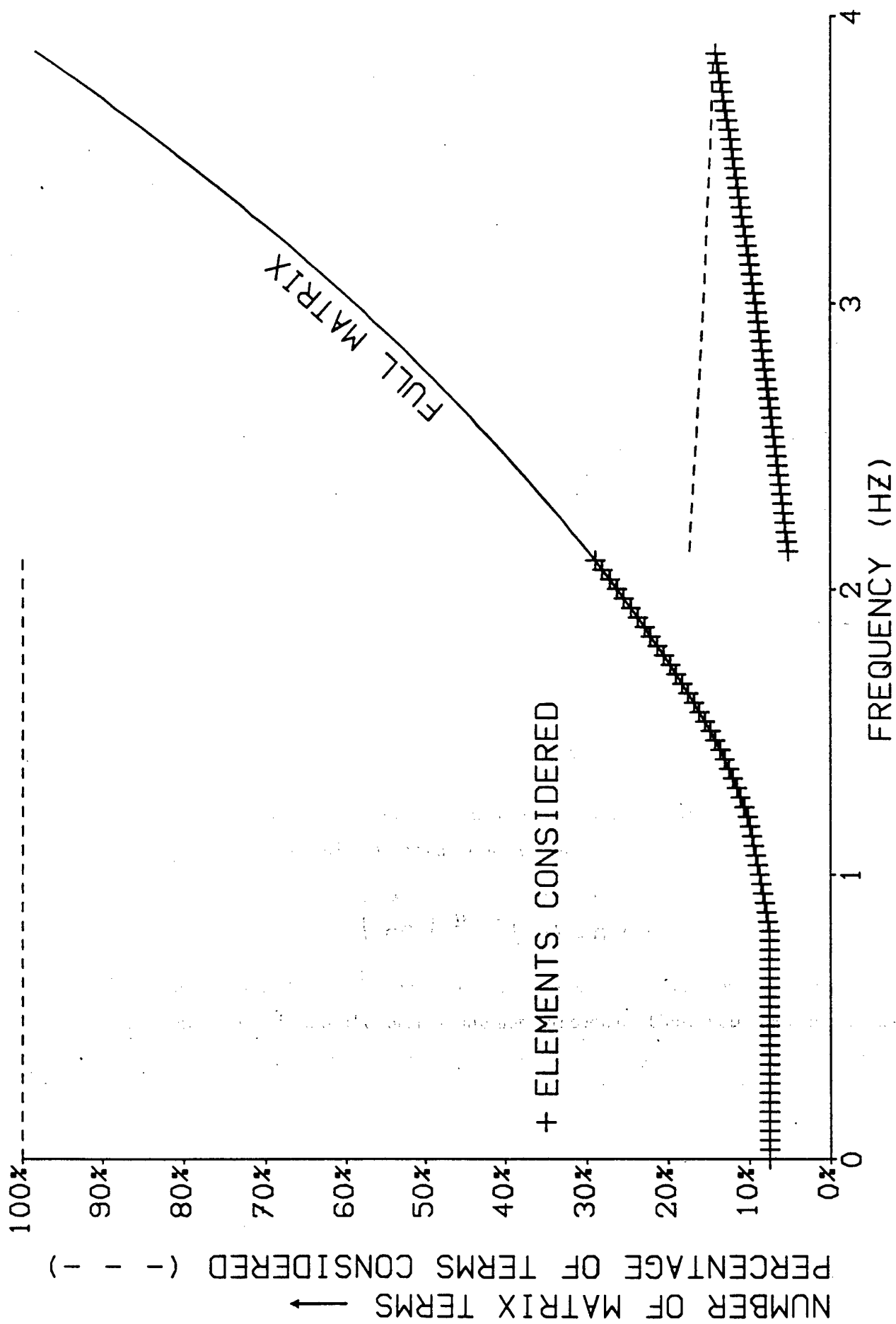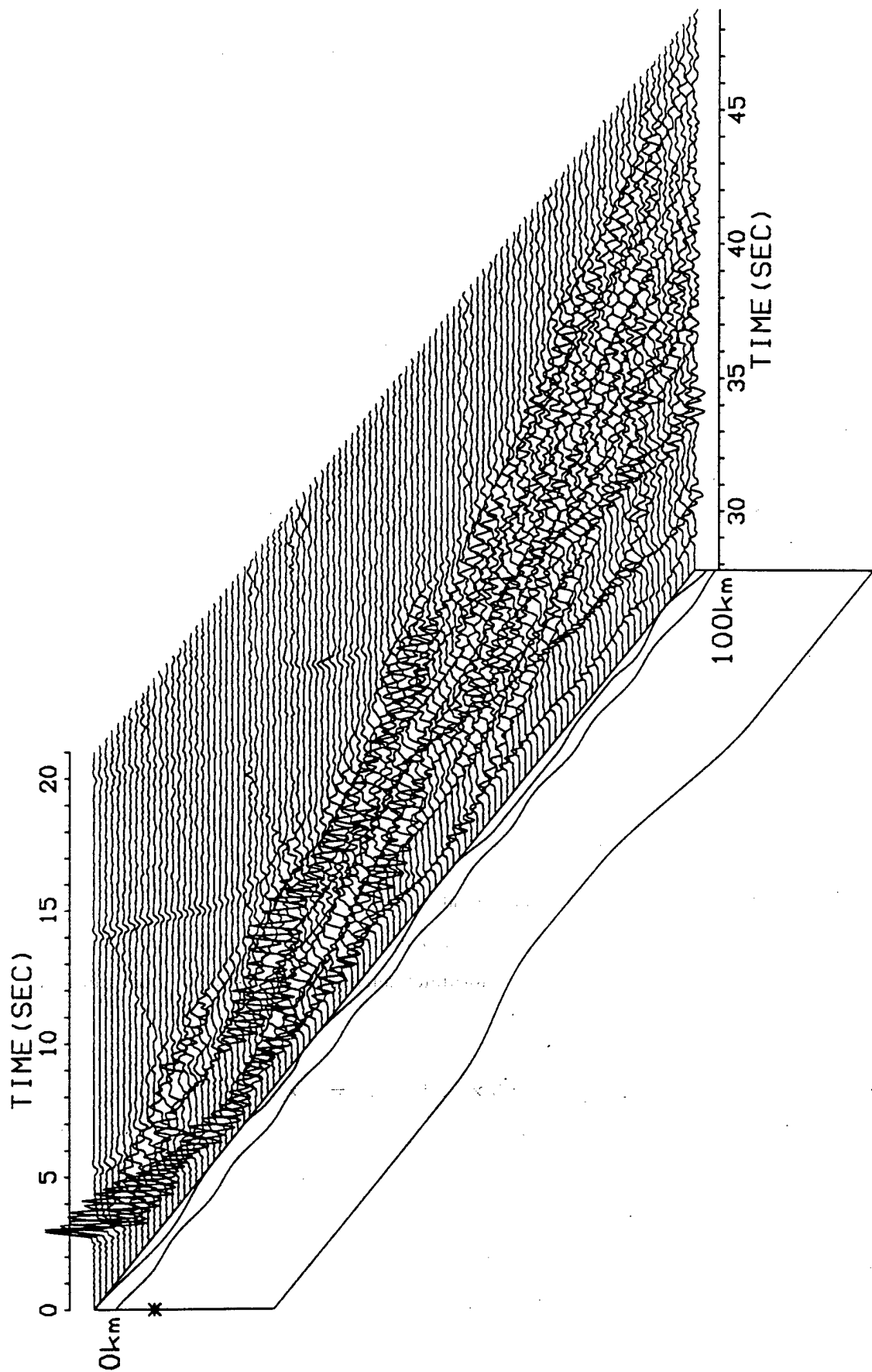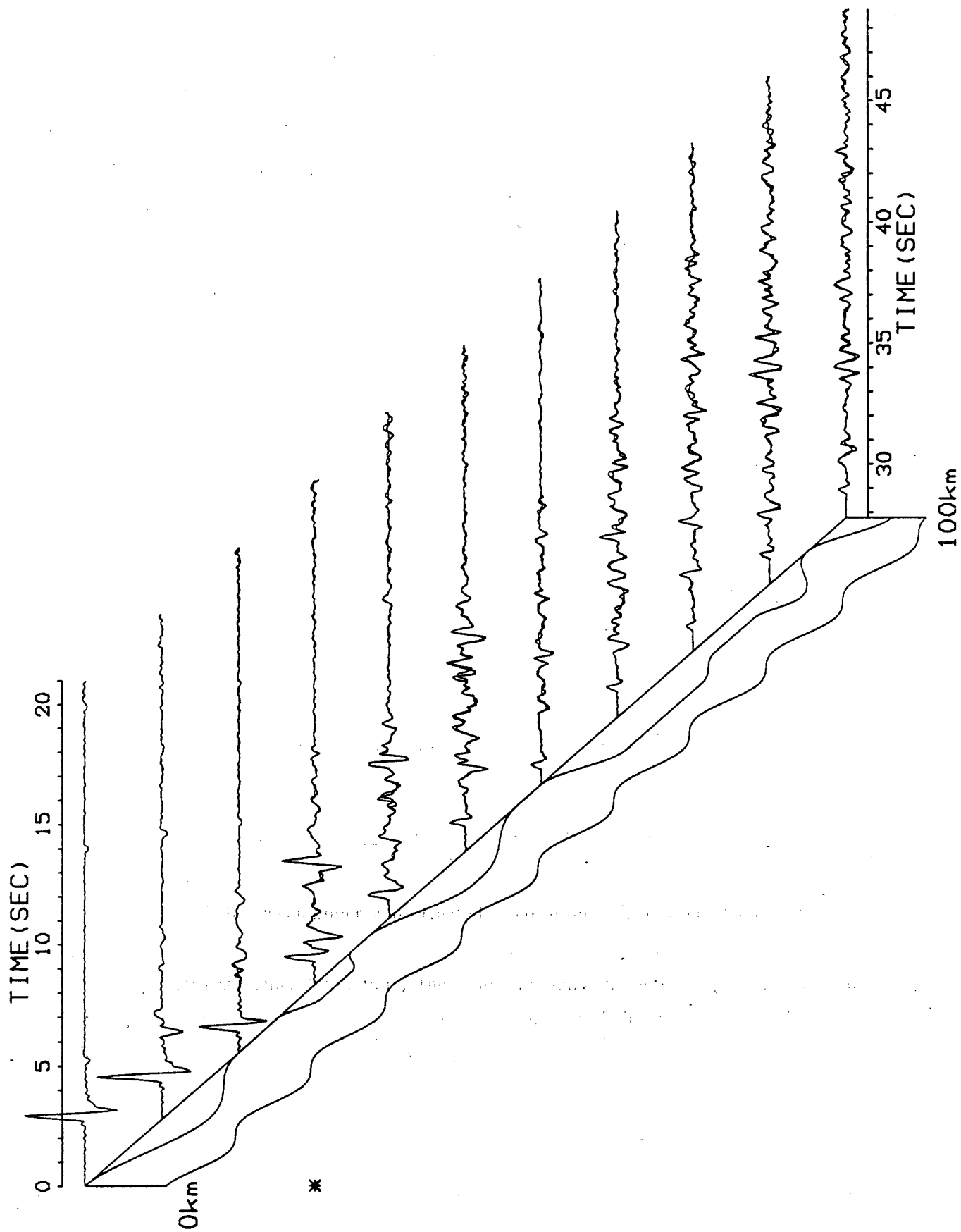
TIME (SEC)

TIME (SEC)

55

Fig 1

AMPLITUDE

PHASE

DISTANCE

0km   100km

β=2km/s.

β=3km/s

ρ=2.2

ρ=2.6

β=3.6km/s

ρ=2.9

β=4.6km/s

ρ=3.1

4km

10km

30km

DEPTH

56

Fig 2

Fig 3

Fig 4

TIME (SEC)

TIME (SEC)

0km

100km

0   5   10   15   20

30   35   40   45

Fig 5

TIME (SEC)

0km

100km

TIME (SEC)

60

Fig 6

SCATTERING OF ACOUSTIC AND ELASTIC WAVES USING A HYBRID MULTIPLE MULTIPOLE EXPANSIONS-FINITE ELEMENT TECHNIQUE

Matthias G. Imhof

Earth Resources Laboratory

Department of Earth, Atmospheric, and Planetary Sciences

Massachusetts Institute of Technology

42 Carleton Street

Cambridge, MA 02142 - 1324

ABSTRACT

In this paper, two different methods to solve scattering problems in acoustic or elastic media are coupled to enhance their usefulness. The multiple multipole (MMP) expansions are used to solve for the scattered fields in homogeneous regions which are possibly unbounded. The finite element (FE) method is used to calculate the scattered fields in heterogeneous but bounded scatterers. As the MMP method requires, the different regions and methods are coupled together in the least squares sense. For some examples, the scattered fields are calculated and compared to the analytical solutions. Finally, the seismograms are calculated for a scattering problem with several scatterers, and complex geometries. Thus, the hybrid MMP-FEM technique is a very general and useful tool to solve complex, two-dimensional scattering problems.

INTRODUCTION

Wave scattering problems have been investigated by different techniques. Analytical solutions to the integral equations do generally not exist except for some very simple geometries. Analytical mode expansion is limited to geometries such as circular cylinders or spheres where the modes decouple (Pao and Mow, 1973). Therefore, numerical schemes seem to be the most direct procedure for arbitrary geometries. Numerical boundary integral techniques (Schuster and Smith, 1985), the T-matrix method (Waterman, 1969, 1976) and MMP expansions (Hafner, 1990; Imhof, 1995a,b) are examples thereof. Unfortunately, they all depend on either Greens functions or other solutions to the wave equation which tend to be hard or impossible to find for heterogeneous or anisotropic media. Thus, these methods are normally limited to scattering between homogeneous scatterers embedded in a homogeneous background. As an advantage, these methods do not encounter problems with unbounded domains. No artificial radiating boundary conditions have to be enforced. In fact, the scattered fields can be evaluated anywhere.

In cases where the medium is heterogeneous, finite element (FE) (Zienkiewicz, 1977; Schwarz, 1988; Murphy and Chin-Bing, 1989, 1991; Marfurt, 1984) or finite differences (FD) (Marfurt, 1984; Kelly *et al.*, 1976; Virieux, 1986) techniques are routinely used to calculate the scattered wavefields. Opposed to the boundary methods mentioned priorly, FE and FD encounter serious problems with unbounded domains. The domain has to be truncated and radiating boundary conditions have to be enforced. Even if the domains are bounded, they are limited due to computer memory and runtime considerations. For many problems the distance, between inhomogeneities, source and receivers are rather large and thus result in prohibitive computation times and memory requirements.

Many scattering problems exist which fall in between these two classes. These problems involve heterogeneous regions which are bounded and embedded in a homogeneous background. Therefore, there is an obvious interest in combining methods for unbounded, homogeneous domains with methods which can handle heterogeneous regions of limited extent (Su, 1983; Dubus, 1994). In the present paper, such a combination is made between the MMP expansions and the FE method (FEM).

We will apply the hybrid technique to both acoustic and elastic in-plane scattering problems where one or multiple heterogeneities are embedded in a homogeneous medium. Both source and receiver are in the homogeneous region. All the ideas presented will also hold if the source and

receiver are located in the heterogeneity. We could then use the combined MMP-FEM technique to construct the radiating boundary condition. In this work, we will not investigate this usage of the technique. Also, we will neglect the case of anti-plane wave motion (SH) because it can easily be derived from the acoustic case.

This paper is structured as follows: First, we will review both MMP expansions and the finite element method for the acoustic case. Next, we combine the methods for the acoustic case. Then, we review MMP and FEM in the elastic case and present the combination thereof. Finally, we discuss some details of the implementation on a computer, present solutions to some scattering problems and compare them to analytical solutions where available.

ACOUSTIC THEORY

We would like to model how an incident wavefield $p^{inc}(\vec{x}, \omega)$ of angular frequency ω scatters from an object. The situation is depicted in Figure 1. The scatterer Ω^I is heterogeneous and embedded in a homogeneous background Ω^O. For the sake of clarity, we will suppress the time factor $e^{-i\omega t}$ in all following expressions. Where necessary, the superscripts ^{O}, ^{B} and ^{I} will denote quantities which belong to the homogeneous outside, lie on the boundary between the domains or are inside the heterogeneous region, respectively. Quantities marked with a tilde are either transformed quantities (e.g., LU decomposed) or local quantities for one particular little element $\tilde{\Omega}$ where the context allows to infer the correct meaning.

Homogeneous Regions: Multiple Multipole Expansions

In a homogeneous region Ω^O, expansions for the pressure fields are made with exact solutions to the homogeneous wave equation

$$P^O(\mathbf{x}) = \sum_{j=1}^{J^O} p_j^O P_j^O(\mathbf{x}) \quad \text{where} \quad \forall P_j^O : (\nabla^2 + k_O^2)P_j^O = 0 \tag{1}$$

where $k_O = \omega/\alpha_O$ is the wave number and α_O the wave velocity in the homogeneous region. The factors p_j^O are complex valued weighting coefficients for the different expansion functions P_j^O. As the name of the method implies, several multipole solutions centered at different positions are often used as expansion functions. The reason to use multiple multipole expansions is their local behavior

and thus their ability to model wavefields scattered from complex geometries (Imhof, 1995a).

$$P^O(\mathbf{x}) = \sum_{m=1}^{M} \sum_{n=-N}^{N} p_{mn}^O e^{in\varphi} H_{|n|}^{(1)} (k_O |\mathbf{x} - \mathbf{x}_m|) \tag{2}$$

The function $H_{|n|}^{(1)}$ is the Hankel function of the first kind and order n radiating outward. Each summation over the index n builds up one multipole. To enhance the convergence, M different expansion centers located at $\mathbf{x}_m$ are used. Since the Hankel functions have a singularity at their origin, the centers of expansions $\mathbf{x}_m$ may not be located in the homogeneous region Ω^O. For each expansion center, all orders between $-N \leq n \leq +N$ are used as basis functions.

However, additional expansion functions, such as plane waves or other special modes, can be included. As a result, MMP expansions have, in general, a smaller number of unknowns than comparable methods. Equations for the weighting coefficients p_j^O are obtained by enforcing boundary conditions for the pressure and the normal displacement on discrete matching points $\mathbf{m}_i$ on the boundaries between domains. The boundary conditions between two domains Ω^O and Ω^X are

$$\sum_{1}^{J^O} p_j^O P_j^O(\mathbf{m}_i) + P^{inc}(\mathbf{m}_i) = P^X(\mathbf{m}_i) \tag{3}$$

$$\frac{-1}{k_O^2 \lambda^O} \hat{n}_i \cdot \sum_{1}^{J^O} p_j^O \nabla P_j^O(\mathbf{m}_i) + \frac{-1}{k_O^2 \lambda^O} \hat{n}_i \cdot \nabla P^{inc}(\mathbf{m}_i) = \frac{-1}{k_X^2 \lambda^X} \hat{n}_i \cdot \nabla P^X(\mathbf{m}_i) \tag{4}$$

where it is assumed that the only source is the incident field P^{inc} in the homogeneous domain Ω^O. Thus, we can build the following linear equation system

$$\begin{pmatrix} \mathbf{P}^O \\ \mathbf{U}^O \end{pmatrix} \cdot \mathbf{p}^O = \begin{pmatrix} \mathbf{P}^X - \mathbf{P}^{inc} \\ \mathbf{U}^X - \mathbf{U}^{inc} \end{pmatrix} \tag{5}$$

where the submatrices P_{ij}^O and U_{ij}^O contain P_j^O and $\frac{-1}{k_O^2 \lambda^O} \hat{n}_i \cdot \nabla P_j^O$ evaluated at the matching points $\mathbf{m}_i$. In general, expansions of the form (1) are not orthogonal. Thus, more matching points than needed are used and the resulting overdetermined linear system (5) is solved in the *least square sense* minimizing the overall error in the boundary conditions. Due to their definition, the matrices $\mathbf{P}^O$ and $\mathbf{U}^O$ are rectangular and dense matrices.

Heterogeneous Regions: Finite Elements

Neglecting source terms, waves propagating in an heterogeneous region Ω^I are governed by the general Helmholtz equation.

$$\nabla \cdot \left\{ \rho^{-1} \, \nabla P \right\} + \rho^{-1} k^2 \, P = 0) \tag{6}$$

where $\rho = \rho(\mathbf{x})$ and $k = k(\mathbf{x})$ denote density and wave number, respectively.

To solve this equation, we partition heterogeneous domain Ω^I into small and nonoverlapping elements $\tilde{\Omega}$ (Zienkiewicz, 1977; Schwarz, 1988; Murphy and Chin-Bing, 1989). Commonly, one chooses triangular or quadrangular elements. In each element, the pressure field $\tilde{P}$ is approximated by an interpolation function. For a quadrangular element, the most simple interpolation function to use is the bilinear one:

$$\tilde{P}(\mathbf{x}) = a_0 + a_1 x + a_2 z + a_3 xz \tag{7}$$

Instead of directly using the coefficients a_j, the polynomial (7) is transformed into the sum of simple shape functions $\tilde{N}_j(\mathbf{x})$ having local support only. For example, in a rectangular element of unit size, $\tilde{N}_3(\mathbf{x}) = xz$. This shape function is visualized in Figure 2. The other ones are obtained by rotations of $-180°$, $-90°$ and $90°$.

$$\tilde{P}(\mathbf{x}) = \sum_{j=1}^{4} \tilde{p}_j \tilde{N}_j(\mathbf{x}) \tag{8}$$

In fact, the complex valued weighting coefficients $\tilde{p}_j$ are the pressure values at the element's corners $\tilde{\mathbf{x}}_i$. They are also known as node points. The coefficients $\tilde{p}_j$ are called node variables. Also, the interpolation functions have to satisfy the following conditions:

$$\tilde{N}_j(\tilde{\mathbf{x}}_i) = \delta_{ij} \tag{9}$$

$$\sum_{j=1}^{4} \tilde{N}_j(\mathbf{x}) = 1 \quad \text{for} \quad \mathbf{x} \in \tilde{\Omega} \tag{10}$$

Thus, the pressure in the Helmholtz equation (6) is replaced by the interpolation (8). Applying Galerkin's method, we multiply the resulting expression by the test function $\tilde{N}_i(\mathbf{x})$ and integrate over the element $\tilde{\Omega}$.

$$\sum_{j=1}^{4} \left\{ \iint_{\tilde{\Omega}} \rho^{-1} \, \nabla \tilde{N}_i \cdot \nabla \tilde{N}_j \, dA - \iint_{\tilde{\Omega}} \rho^{-1} k^2 \, \tilde{N}_i \tilde{N}_j \, dA \right\} \tilde{p}_j - \int_{\tilde{\Gamma}} \rho^{-1} \tilde{N}_i \frac{\partial P}{\partial n} \, dl = 0 \tag{11}$$

where the divergence theorem is used to transform the first integral. The integrals are over the surface $\tilde{\Omega}$ or around the boundary $\tilde{\Gamma}$ of the element $\tilde{\Omega}$, respectively. Evaluating (11) for all four $\tilde{N}_i(\mathbf{x})$ will yield a set of four equations for the four unknown node variables $\tilde{p}_j$.

These three integrals define the local stiffness matrix $\tilde{\mathbf{S}}$, the local mass matrix $\tilde{\mathbf{M}}$ and the local force vector $\tilde{\mathbf{f}}$.

$$\tilde{S}_{ij} = \iint_{\tilde{\Omega}} \rho^{-1}\, \nabla \tilde{N}_i \cdot \nabla \tilde{N}_j \, dA \tag{12}$$

$$\tilde{M}_{ij} = \iint_{\tilde{\Omega}} \rho^{-1} k^2 \, \tilde{N}_i \tilde{N}_j \, dA \tag{13}$$

$$\tilde{f}_i = \int_{\tilde{\Gamma}} \rho^{-1} \tilde{N}_i \frac{\partial P}{\partial n} \, dl \tag{14}$$

For elements that are in the interior, the boundary integral (14) is not zero, but its contributions will exactly cancel with like terms coming from neighboring elements. One only need to recall that the term $\rho^{-1}\frac{\partial P}{\partial n}$ is proportional to the normal displacement. But both the normal displacement and the pressure are continuous across boundaries. Therefore, only on the domain boundary the line integral has to be taken into account since it is not cancelled by another term.

If the element $\tilde{\Omega}$ is adjacent to a rigid domain, the boundary integral (14) will vanish, since $\tilde{N}_i = 0$. If the element is adjacent to a void domain, the integral (14) also vanishes because $\frac{\partial P}{\partial n} = 0$. In all other cases, the boundary integral (14) has to be included. Assuming that $\frac{\partial P}{\partial n}$ can be approximated by a function similar to $\tilde{N}_i$ along the boundary, we can replace (14) by

$$\tilde{f}_i = \sum_{j=1}^{4} \tilde{F}_{ij} \frac{\partial P(\mathbf{x}_j)}{\partial n} \qquad \tilde{F}_{ij} = \int_{\tilde{\Gamma}} \rho^{-1} \tilde{N}_i \tilde{N}_j \, dl. \tag{15}$$

If the density ρ and the wavenumber k are treated as constants within each element, $\tilde{\mathbf{S}}$, $\tilde{\mathbf{M}}$ and $\tilde{\mathbf{F}}$ can be evaluated exactly. Once the contribution of the various elements is determined, the global system of equations is formed by mapping the local node numbers onto the global node numbers, giving rise to the global pressure vector $\mathbf{p}$, and combining all of the subsystems $\tilde{\mathbf{S}}$, $\tilde{\mathbf{M}}$ and $\tilde{\mathbf{f}}$ into their global counterparts $\mathbf{S}$, $\mathbf{M}$ and $\mathbf{f}$ (Schwarz, 1988). Both matrices $\mathbf{S}$ and $\mathbf{M}$ are sparse, banded and symmetric. Each row of the global matrix system can then be reduced to

$$\sum_{j=1}^{J} \left\{ (S_{ij} - M_{ij}) \cdot p_j - F_{ij} \cdot \frac{\partial P(\mathbf{x}_j)}{\partial n} \right\} = 0 \tag{16}$$

where J is the total number of node variables or in simpler matrix form

$$\mathbf{K} \cdot \mathbf{p} - \mathbf{f} = 0 \qquad (17)$$

where $\mathbf{K} = \mathbf{S} - \mathbf{M}$ and the vector $\mathbf{p}$ contains all the unknown, global nodal values p_j.

Coupling the Regions

The vector $\mathbf{p}$ obtained from the finite elements containing the node variables can be split into two subvectors $\mathbf{p}^I$ and $\mathbf{p}^B$. The node variables from inside the domain Ω^I are collected in the vector $\mathbf{p}^I$. The subvector $\mathbf{p}^B$ accommodates the node variables whose nodal points $\mathbf{x}_i$ lie on the boundary $\partial \Omega^B$. Since the boundary $\partial \Omega^B$ belongs to both domains, the respective wavefields P^O and P^B have to match along the boundary.

Thus we replace the node variables p_i^B by

$$p_i^B = \sum_{k=1}^{J^O} p_k^O P_k(\mathbf{x}_i) + P^{inc}(\mathbf{x}_i) \qquad (18)$$

Furthermore, we can also find $\frac{\partial P(\mathbf{x}_i)}{\partial n}$ by evaluating

$$\frac{\partial P(\mathbf{x}_i)}{\partial n} = \sum_{k=1}^{J^O} p_k^O \hat{n}_i \nabla P_k(\mathbf{x}_i) + \hat{n}_i \nabla P^{inc}(\mathbf{x}_i) \qquad (19)$$

Combining (16), (18) and (19) yields the hybrid matrix system

$$\sum_{j=1}^{J^I} \left\{ K_{ij} \cdot p_j \right\} + \sum_{j=J^B}^{J} \left\{ K_{ij} \cdot \sum_{k=1}^{J^O} p_k^O P_k(\mathbf{x}_j) - F_{ij} \cdot \sum_{k=1}^{J^O} p_k^O \hat{n}_j \nabla P_k(\mathbf{x}_j) \right\} =$$
$$\sum_{j=J^B}^{J} \left\{ F_{ij} \cdot \hat{n}_j \nabla P^{inc}(\mathbf{x}_j) - K_{ij} \cdot P^{inc}(\mathbf{x}_j) \right\} \quad (20)$$

where J^I is the total number of node variables inside the heterogeneous region Ω^I. J^B is the node number of the first nodal point lying on the boundary $\partial \Omega^B$. The value of J^B is $J^I + 1$. As before, J is the total number of node points. Finally, J^O is the total number of functions used for the MMP expansion of the outside field. The complete system can be written in a more compact form as

$$\begin{pmatrix} \mathbf{A}^{II} & \mathbf{A}^{IO} \\ \mathbf{A}^{OI} & \mathbf{A}^{OO} \end{pmatrix} \cdot \begin{pmatrix} \mathbf{p}^I \\ \mathbf{p}^O \end{pmatrix} = \begin{pmatrix} \mathbf{f}^I \\ \mathbf{f}^O \end{pmatrix} \qquad (21)$$

where $\mathbf{A}^{II}$ is a sparse, diagonally dominant and symmetric matrix. Both $\mathbf{A}^{IO}$ and $\mathbf{A}^{OI}$ are sparse and rectangular, while $\mathbf{A}^{OO}$ is rectangular, but dense matrix. The force vector $\mathbf{f}^I$ is sparse, while $\mathbf{f}^O$ is completely filled.

The matrix $\mathbf{A}^{II}$ and the solution vector $\mathbf{p}^I$ stem from the interior problem which is solved by FE. It contains as many equations as unknowns and can be solved exactly. The matrices $\mathbf{A}^{IO}$ and $\mathbf{A}^{OI}$ couple the interior problem to the exterior problem and vice versa. The matrix $\mathbf{A}^{OO}$ and the solution vector $\mathbf{p}^O$ stem from the exterior problem which is solved by MMP expansions. It has to be solved in the least squares sense because there are more equations needed than unknowns given. Therefore, the complete matrix system (21) can not be solved exactly. Contrarily, it does neither mathematically nor physically make sense to solve the complete system (21) in the least squares sense. Prior experience with MMP methods shows that at least twice as many equations as unknowns are needed to obtain a reasonable solution (Imhof, 1995b). Unfortunately, there are in general more unknowns in the interior than in the exterior. Thus, it is nearly impossible to obtain more than twice as many equations as unknowns. Furthermore, the solution in the interior is already an approximation to the wave equation. Solving the complete system in the least squares sense distributes the errors evenly over all unknowns which corrupts the solution in the interior further.

Therefore, the system (21) is solved in two steps: first, the interior node variables $\mathbf{p}^I$ are eliminated by a partial Gaussian elimination. Because the corresponding submatrix $\mathbf{A}^{II}$ is derived with the finite elements method and thus diagonally dominant, the Gaussian elimination can be performed without additional pivoting.

$$
\begin{pmatrix} \tilde{\mathbf{A}}^{II} & \tilde{\mathbf{A}}^{IO} \\ \mathbf{0} & \tilde{\mathbf{A}}^{OO} \end{pmatrix} \cdot \begin{pmatrix} \tilde{\mathbf{p}}^I \\ \tilde{\mathbf{p}}^O \end{pmatrix} = \begin{pmatrix} \tilde{\mathbf{f}}^I \\ \tilde{\mathbf{f}}^O \end{pmatrix} \tag{22}
$$

The submatrix $\tilde{\mathbf{A}}^{II}$ is now an upper triangular matrix. The remaining system can then be solved in the least squares sense using the normal equations

$$
\left(\tilde{\mathbf{A}}^{OO} \right)^H \cdot \tilde{\mathbf{A}}^{OO} \cdot \mathbf{p}^O = \left(\tilde{\mathbf{A}}^{OO} \right)^H \cdot \tilde{\mathbf{f}}^O \tag{23}
$$

where the superscript ^{H} denotes the complex conjugate transpose. If desired, the values of the node variables $\mathbf{p}^I$ are found by back-substitution.

$$
\tilde{\mathbf{A}}^{II} \cdot \mathbf{p}^I = \tilde{\mathbf{f}}^I - \tilde{\mathbf{A}}^{IO} \cdot \mathbf{p}^O \tag{24}
$$

Practically, the system (21) is solved by a combined, row-wise LU-QR algorithm. From each new row, the interior node variables are Gaussian eliminated. Then, Givens row updating (schwarz, 1989) is performed on the remaining row. The scheme is equal to normal Givens updating with the first J^I Givens rotations replaced by Gaussian eliminations instead. Thus, the first J^I rows are only LU decomposed. All other rows are additionally Givens rotated.

Remark: An Alternative Solver Scheme

Alternatively, the system (21) can be solved by the iterative scheme:

$$\mathbf{A}^{II} \cdot \mathbf{p}_n^I = \mathbf{f}^I - \mathbf{A}^{IO} \cdot \mathbf{p}_{n-1}^O \tag{25a}$$

$$\mathbf{A}^{OO} \cdot \mathbf{p}_n^O = \mathbf{f}^O - \mathbf{A}^{OI} \cdot \mathbf{p}_{n-1}^I \tag{25b}$$

Optimally, each of (25a) and (25b) is also solved by an iterative scheme such as the conjugate gradient method (Hestenes and Stiefel, 1952). The first part (25a) is square, symmetric and sparse. The second part (25b) is rectangular and dense, but relatively small compared to (25a). The scheme (25) offers an alternative to (21), but this has not yet been tried.

ELASTIC THEORY

Homogeneous Regions: Multiple Multipole Expansions

In a homogeneous region Ω^O, expansions for the displacement fields $\mathbf{w}(\mathbf{x}) = (u(\mathbf{x}), v(\mathbf{x}))$ are made with exact solutions to the homogeneous wave equation (Imhof, 1995b).

$$\mathbf{w}(\mathbf{x}) = \sum_{j=1}^{J^O} \left\{ \phi_j \mathbf{w}_j^\Phi(\mathbf{x}) + \psi_j \mathbf{w}_j^\Psi(\mathbf{x}) \right\} \tag{26}$$

where

$$\mathbf{w}_j^\Phi(\mathbf{x}) = \nabla \Phi_j(\mathbf{x}) \tag{27a}$$

$$\mathbf{w}_j^\Psi(\mathbf{x}) = \nabla \times (\hat{y}\Psi_j(\mathbf{x})) \tag{27b}$$

and each expansion function Φ_j or Ψ_j satisfies a Helmholtz equation

$$(\nabla^2 + k_O^2)\Phi_j = 0 \tag{28a}$$

$$(\nabla^2 + l_O^2)\Psi_j = 0 \tag{28b}$$

69

where k_O and l_O are the the wave numbers of the P-, respective S-wave in the homogeneous region. The factors ϕ_j and ϕ_j are complex valued weighting coefficients for the different expansion functions Φ_j and Ψ_j. Similar to the acoustic MMP expansions (2), we choose multipole expansions for Φ_j and Ψ_j.

$$\Phi(\mathbf{x}) \;=\; \sum_{m=1}^{M} \sum_{n=-N}^{N} \phi_{mn} e^{in\varphi}\, H_{|n|}^{(1)}\left(k_O\,|\mathbf{x} - \mathbf{x}_m|\right) \tag{29a}$$

$$\Psi(\mathbf{x}) \;=\; \sum_{m=1}^{M} \sum_{n=-N}^{N} \psi_{mn} e^{in\varphi}\, H_{|n|}^{(1)}\left(l_O\,|\mathbf{x} - \mathbf{x}_m|\right) \tag{29b}$$

Equations for the weighting coefficients ϕ_j and ψ_j are obtained by enforcing boundary conditions along discrete matching points $\mathbf{m}_i$ on the boundaries between domains. The boundary conditions between two domains Ω^O and Ω^X are continuity of displacement and stresses in normal and tangential directions:

$$\sum_{j=1}^{J^O} \left\{ \phi_j u_j^{\Phi}(\mathbf{m}_i) + \psi_j u_j^{\Psi}(\mathbf{m}_i) \right\} + u^{inc}(\mathbf{m}_i) \;=\; u^X(\mathbf{m}_i) \tag{30}$$

$$\sum_{j=1}^{J^O} \left\{ \phi_j v_j^{\Phi}(\mathbf{m}_i) + \psi_j v_j^{\Psi}(\mathbf{m}_i) \right\} + v^{inc}(\mathbf{m}_i) \;=\; v^X(\mathbf{m}_i) \tag{31}$$

$$\sum_{j=1}^{J^O} \hat{n}_i \left\{ \phi_j \sigma_j^{\Phi}(\mathbf{m}_i) + \psi_j \sigma_j^{\Psi}(\mathbf{m}_i) \right\} \hat{n}_i + \hat{n}_i\, \sigma^{inc}(\mathbf{m}_i)\, \hat{n}_i \;=\; \hat{n}_i\, \sigma^X(\mathbf{m}_i)\, \hat{n}_i \tag{32}$$

$$\sum_{j=1}^{J^O} \hat{t}_i \left\{ \phi_j \sigma_j^{\Phi}(\mathbf{m}_i) + \psi_j \sigma_j^{\Psi}(\mathbf{m}_i) \right\} \hat{n}_i + \hat{t}_i\, \sigma^{inc}(\mathbf{m}_i)\, \hat{n}_i \;=\; \hat{t}_i\, \sigma^X(\mathbf{m}_i)\, \hat{n}_i \tag{33}$$

where $\sigma_j^{\Phi}(\mathbf{m}_i)$, $\sigma_j^{\Psi}(\mathbf{m}_i)$, $\sigma^{inc}(\mathbf{m}_i)$ and $\sigma^X(\mathbf{m}_i)$ denote the stresses evaluated at $\mathbf{m}_i$ due to the displacements $\mathbf{w}_j^{\Phi}(\mathbf{m}_i)$, $\mathbf{w}_j^{\Psi}(\mathbf{m}_i)$, $\mathbf{w}_j^{inc}(\mathbf{m}_i)$ and $\mathbf{w}_j^X(\mathbf{m}_i)$, respectively. Accordingly, we can build a linear equation system

$$\begin{pmatrix} \mathbf{U}^{\Phi} & \mathbf{U}^{\Psi} \\ \mathbf{V}^{\Phi} & \mathbf{V}^{\Psi} \\ \Sigma_n^{\Phi} & \Sigma_n^{\Psi} \\ \Sigma_t^{\Phi} & \Sigma_t^{\Psi} \end{pmatrix} \cdot \begin{pmatrix} \phi \\ \psi \end{pmatrix} = \begin{pmatrix} \mathbf{U}^X - \mathbf{U}^{inc} \\ \mathbf{V}^X - \mathbf{V}^{inc} \\ \Sigma_n^X - \Sigma_n^{inc} \\ \Sigma_t^X - \Sigma_t^{inc} \end{pmatrix} \tag{34}$$

where the submatrices contain equations (30–33) evaluated at all matching points $\mathbf{m}_i$.

Heterogeneous Regions: Finite Elements

Again neglecting source terms, the equations of motion for elastic medium for the displacement components u and v are

$$\omega^2 \rho u + \left(c_{11} u_{,x} + c_{12} v_{,z}\right)_{,x} + c_{33} \left(u_{,z} + v_{,x}\right)_{,z} = 0 \qquad (35a)$$

$$\omega^2 \rho v + c_{33} \left(u_{,z} + v_{,x}\right)_{,x} + \left(c_{12} u_{,x} + c_{22} v_{,z}\right)_{,z} = 0 \qquad (35b)$$

where the density ρ and the elastic constants $c_{11} = c_{22} = \lambda + 2\mu$, $c_{12} = \lambda$ and $c_{33} = \mu$ are all spatially varying. The subscripts $_{,x}$ and $_{,z}$ denote partial derivatives with respect to x or z, respectively.

As in the acoustic case (8), the displacements inside the elements $\tilde{\Omega}$ are approximated by interpolation functions (Zienkiewicz, 1977; Schwarz, 1988; Murphy and Chin-Bing, 1991):

$$\tilde{u} = \sum_{j=1}^{4} \tilde{u}_j \tilde{N}_j(\mathbf{x}) \qquad (36a)$$

$$\tilde{v} = \sum_{j=1}^{4} \tilde{v}_j \tilde{N}_j(\mathbf{x}) \qquad (36b)$$

The complex valued weighting coefficients $\tilde{u}_j$ and $\tilde{u}_j$ are the components of the displacements at the element's corners $\tilde{\mathbf{x}}_i$. The shape functions $\tilde{N}_j(\mathbf{x})$ are the same as in the acoustic case, e.g. $\tilde{N}_3(\mathbf{x}) = xz$ (Figure 2).

In the equation of motion (35), we replace the displacements u and v by the interpolations (36). Applying Galerkin's method for each element $\tilde{\Omega}$, we multiply the resulting expression by the test function $\tilde{N}_i(\mathbf{x})$ and integrate over the element $\tilde{\Omega}$.

$$\sum_{j=1}^{4} \left\{ \iint_{\tilde{\Omega}} \left(c_{11} \tilde{N}_{i,x} \tilde{N}_{j,x} + c_{33} \tilde{N}_{i,z} \tilde{N}_{j,z}\right) dA - \iint_{\tilde{\Omega}} \rho \omega^2 \, \tilde{N}_i \tilde{N}_j \, dA \right\} \tilde{u}_j \; +$$

$$\sum_{j=1}^{4} \left\{ \iint_{\tilde{\Omega}} \left(c_{12} \tilde{N}_{i,x} \tilde{N}_{j,z} + c_{33} \tilde{N}_{i,z} \tilde{N}_{j,x}\right) dA \right\} \tilde{v}_j - \int_{\tilde{\Gamma}} \tilde{N}_i \hat{x} \sigma \hat{n} \, dl = 0 \quad (37a)$$

$$\sum_{j=1}^{4} \left\{ \iint_{\tilde{\Omega}} \left(c_{12} \tilde{N}_{i,z} \tilde{N}_{j,x} + c_{33} \tilde{N}_{i,x} \tilde{N}_{j,z}\right) dA \right\} \tilde{u}_j \; -$$

$$\sum_{j=1}^{4} \left\{ \iint_{\tilde{\Omega}} \left(c_{33} \tilde{N}_{i,x} \tilde{N}_{j,x} + c_{22} \tilde{N}_{i,z} \tilde{N}_{j,z}\right) dA - \iint_{\tilde{\Omega}} \rho \omega^2 \, \tilde{N}_i \tilde{N}_j \, dA \right\} \tilde{v}_j - \int_{\tilde{\Gamma}} \tilde{N}_i \hat{z} \sigma \hat{n} \, dl = 0 \quad (37b)$$

71

where we used the divergence theorem to transform some of the volume integrals into line integrals. The quantity σ denotes the stress tensor along the boundary. Thus, evaluating (37) for all $\tilde{N}_i(\mathbf{x})$ will yield a set of equations for the unknown node variables $\tilde{u}_j$ and $\tilde{v}_j$. Again, equation (37) defines the stiffness matrices $\tilde{\mathbf{S}}^{ij}$, mass matrices $\tilde{\mathbf{M}}^{ii}$ and the force vectors $\tilde{\mathbf{f}}^i$:

$$\tilde{M}_{ij}^{11} = \tilde{M}_{ij}^{22} = \iint_{\tilde{\Omega}} \rho \omega^2 \, \tilde{N}_i \tilde{N}_j \, dA \tag{38}$$

$$\tilde{S}_{ij}^{11} = \iint_{\tilde{\Omega}} \left(c_{11} \tilde{N}_{i,x} \tilde{N}_{j,x} + c_{33} \tilde{N}_{i,z} \tilde{N}_{j,z} \right) dA \tag{39}$$

$$\tilde{S}_{ij}^{22} = \iint_{\tilde{\Omega}} \left(c_{33} \tilde{N}_{i,x} \tilde{N}_{j,x} + c_{22} \tilde{N}_{i,z} \tilde{N}_{j,z} \right) dA \tag{40}$$

$$\tilde{S}_{ij}^{12} = \tilde{S}_{ji}^{21} = \iint_{\tilde{\Omega}} \left(c_{12} \tilde{N}_{i,x} \tilde{N}_{j,z} + c_{33} \tilde{N}_{i,z} \tilde{N}_{j,x} \right) dA \tag{41}$$

$$\tilde{f}_i^1 = \int_{\tilde{\Gamma}} \tilde{N}_i \hat{x} \sigma \hat{n} \, dl \tag{42}$$

$$\tilde{f}_i^2 = \int_{\tilde{\Gamma}} \tilde{N}_i \hat{z} \sigma \hat{n} \, dl \tag{43}$$

If the density ρ and the elastic constants c_{11}, c_{22}, c_{12} and c_{33} are treated as constants within each element $\tilde{\Omega}$, all integral (38-41) can be evaluated exactly. For elements which are in the interior, the boundary integrals (42,43) are not zero, but its contributions will exactly cancel with like terms coming from neighboring elements because displacements and stresses are continuous across boundaries. Therefore, the line integrals have to be taken into account only on the domain boundary. Assuming that $\hat{x}\sigma\hat{n}$ and $\hat{z}\sigma\hat{n}$ can be approximated by functions similar to $\tilde{N}_i$ along the boundary, we can replace (42,42) by

$$\tilde{f}_i^1 = \sum_{j=1}^{4} \tilde{F}_{ij} \hat{x} \sigma(\mathbf{x}_j) \hat{n} \tag{44}$$

$$\tilde{f}_i^2 = \sum_{j=1}^{4} \tilde{F}_{ij} \hat{z} \sigma(\mathbf{x}_j) \hat{n} \tag{45}$$

$$\tilde{F}_{ij} = \int_{\tilde{\Gamma}} \tilde{N}_i \tilde{N}_j \, dl \tag{46}$$

which can also be evaluated analytically. Mapping all the local contributions of $\tilde{\mathbf{S}}^{ij}$, $\tilde{\mathbf{M}}^{ii}$ and $\tilde{\mathbf{f}}^i$ into global node numbers yields the global matrices $\mathbf{S}^{ij}$, $\mathbf{M}^{ii}$, $\mathbf{f}^i$ and the global nodal vectors $\mathbf{u}$ and $\mathbf{v}$. Writing $\mathbf{K}^{ij} = \mathbf{S}^{ij} - \delta_{ij}\mathbf{M}^{ii}$, the global matrix system reduces to the simpler system

$$\mathbf{K}^{11}\mathbf{u} + \mathbf{K}^{12}\mathbf{v} - \mathbf{f}^1 = 0 \tag{47a}$$

$$\mathbf{K}^{21}\mathbf{u} + \mathbf{K}^{22}\mathbf{v} - \mathbf{f}^2 = 0. \tag{47b}$$

Coupling the Regions

Each vector $\mathbf{u}$ and $\mathbf{v}$ obtained from the finite elements is split into two subvectors $\mathbf{u}^I$, $\mathbf{u}^B$ and $\mathbf{v}^I$, $\mathbf{v}^B$, respectively. The node variables u_i and v_i from inside the domain Ω^I are collected in the vectors $\mathbf{u}^I$ and $\mathbf{v}^I$, respectively. The subvectors $\mathbf{u}^B$ and $\mathbf{u}^B$ accommodate the node variables whose nodal points $\mathbf{x}_i$ lie on the boundary $\partial\Omega^B$. Since the boundary $\partial\Omega^B$ belongs to both domains, the respective wavefields $\mathbf{w}^O$ and $\mathbf{w}^B$ have to match along the boundary and we can replace the node variables u_j^B and v_j^B by

$$u_j^B = \cdot \sum_{k=1}^{J^O} \left\{ \phi_k u_k^\Phi(\mathbf{x}_j) + \psi_k u_k^\Psi(\mathbf{x}_j) \right\} + u^{inc}(\mathbf{x}_j) \tag{48a}$$

$$v_j^B = \hat{z} \cdot \sum_{k=1}^{J^O} \left\{ \phi_k v_k^\Phi(\mathbf{x}_j) + \psi_k v_k^\Psi(\mathbf{x}_j) \right\} + v^{inc}(\mathbf{x}_j). \tag{48b}$$

Furthermore, we find $\boldsymbol{\sigma}(\mathbf{x}_j)$ by evaluating

$$\boldsymbol{\sigma}(\mathbf{x}_j) = \sum_{k=1}^{J^O} \left\{ \phi_k \sigma_k^\Phi(\mathbf{x}_j) + \psi_k \sigma_k^\Psi(\mathbf{x}_j) \right\} + \sigma^{inc}(\mathbf{x}_j) \tag{49}$$

Combining (47), (48) and (49) yields the coupled MMP-FEM system. For the sake of clarity, we explicitly expand (47a):

$$\sum_{j=1}^{J^I} \left\{ K_{ij}^{11} \cdot u_j + K_{ij}^{12} \cdot v_j \right\} +$$

$$\sum_{j=J^B}^{J} \left\{ K_{ij}^{11} \cdot \sum_{k=1}^{J^O} \left\{ \phi_k u_k^\Phi(\mathbf{x}_j) + \psi_k u_k^\Psi(\mathbf{x}_j) \right\} + K_{ij}^{12} \cdot \sum_{k=1}^{J^O} \left\{ \phi_k v_k^\Phi(\mathbf{x}_j) + \psi_k v_k^\Psi(\mathbf{x}_j) \right\} \right\} -$$

$$\sum_{j=J^B}^{J} \left\{ F_{ij} \cdot \sum_{k=1}^{J^O} \hat{x} \left\{ \phi_k \sigma_k^\Phi(\mathbf{x}_j) + \psi_k \sigma_k^\Psi(\mathbf{x}_j) \right\} \hat{n} \right\} =$$

$$\sum_{j=J^B}^{J} \left\{ F_{ij} \cdot \hat{x}\sigma^{inc}(\mathbf{x}_j)\hat{n} - K_{ij}^{11} \cdot u^{inc}(\mathbf{x}_j) - K_{ij}^{12} \cdot v^{inc}(\mathbf{x}_j) \right\} \tag{50}$$

where J^I is the number of node variables inside the heterogeneous region Ω^I. J^B is the node number of the first nodal point lying on the boundary $\partial\Omega^B$. The value of J^B is $J^I + 1$. As before, J is the total number of node points. Finally, J^O is the total number of functions used for the MMP

expansion of the outside field. The rows of (47b) follow the same outline. The resulting combined system of equations is of similar form as (21) and can be solved using the same scheme.

$$
\begin{pmatrix}
\mathbf{K}_{11}^I & \mathbf{K}_{12}^I & \Phi_1^I & \Psi_1^I \\
\mathbf{K}_{21}^I & \mathbf{K}_{22}^I & \Phi_2^I & \Psi_2^I \\
\mathbf{K}_{11}^O & \mathbf{K}_{12}^O & \Phi_1^O & \Psi_1^O \\
\mathbf{K}_{21}^O & \mathbf{K}_{22}^O & \Phi_2^O & \Psi_2^O
\end{pmatrix}
\cdot
\begin{pmatrix}
\mathbf{u} \\
\mathbf{v} \\
\phi \\
\psi
\end{pmatrix}
=
\begin{pmatrix}
\mathbf{f}_1^I \\
\mathbf{f}_2^I \\
\mathbf{f}_1^O \\
\mathbf{f}_2^O
\end{pmatrix}
\tag{51}
$$

As in the acoustic case, the submatrices K^I resulting from the interior problem are sparse and square. All other submatrices are rectangular. We reduce the above system by Gaussian elimination of the node variables $\mathbf{u}$ and $\mathbf{v}$ which yields a new system.

$$
\begin{pmatrix}
\tilde{\mathbf{K}}_{11}^I & \tilde{\mathbf{K}}_{12}^I & \tilde{\Phi}_1^I & \tilde{\Psi}_1^I \\
0 & \tilde{\mathbf{K}}_{22}^I & \tilde{\Phi}_2^I & \tilde{\Psi}_2^I \\
0 & 0 & \tilde{\Phi}_1^O & \tilde{\Psi}_1^O \\
0 & 0 & \tilde{\Phi}_2^O & \tilde{\Psi}_2^O
\end{pmatrix}
\cdot
\begin{pmatrix}
\mathbf{u} \\
\mathbf{v} \\
\phi \\
\psi
\end{pmatrix}
=
\begin{pmatrix}
\tilde{\mathbf{f}}_1^I \\
\tilde{\mathbf{f}}_2^I \\
\tilde{\mathbf{f}}_1^O \\
\tilde{\mathbf{f}}_2^O
\end{pmatrix}
\tag{52}
$$

The lower half of (52) can now be solved in the least squares sense by QR decomposition.

$$
\begin{pmatrix}
\tilde{\Phi}_1^O & \tilde{\Psi}_1^O \\
\tilde{\Phi}_2^O & \tilde{\Psi}_2^O
\end{pmatrix}
\cdot
\begin{pmatrix}
\phi \\
\psi
\end{pmatrix}
=
\begin{pmatrix}
\tilde{\mathbf{f}}_1^O \\
\tilde{\mathbf{f}}_2^O
\end{pmatrix}
\tag{53}
$$

The node variables in the heterogeneous, interior region are recovered by back-substitution, the upper half of (52) is already in upper triangular form.

$$
\begin{pmatrix}
\tilde{\mathbf{K}}_{11}^I & \tilde{\mathbf{K}}_{12}^I \\
0 & \tilde{\mathbf{K}}_{22}^I
\end{pmatrix}
\cdot
\begin{pmatrix}
\mathbf{u} \\
\mathbf{v}
\end{pmatrix}
=
\begin{pmatrix}
\tilde{\mathbf{f}}_1^I - \tilde{\Phi}_1^I \phi - \tilde{\Psi}_1^I \psi \\
\tilde{\mathbf{f}}_2^I - \tilde{\Phi}_2^I \phi - \tilde{\Psi}_2^I \psi
\end{pmatrix}
\tag{54}
$$

IMPLEMENTATION

Because the technique is a mixture of MMP expansions and the FE method, the finite element method is merged into the prior MMP codes (Imhof, 1995a,b). Thus, the method is implemented on a nCUBE2 parallel computer using the computer language C++. The object oriented design has the advantage, that the coupling as described in (20) and (50) is basically hidden in objects for node variables, finite elements and the expansion functions for the exterior. First, the objects for the finite elements calculate the local $\tilde{\mathbf{M}}$, $\tilde{\mathbf{S}}$ and $\tilde{\mathbf{F}}$ matrices. Then, the resulting coefficients have mapped

74

into the global equation system. Objects for internal node variables simply map the coefficients $\tilde{K}^{ij}$ for the p_j^I into the global system of equations. In contrast, objects for node variables on the boundary automatically evaluate the MMP expansion at the node point as described in equations (18),(19) or (48),(49), weight the expansion with the appropriate $\tilde{K}^{ij}$ or $\tilde{F}^{ij}$ coefficient and map the resulting coefficients for p_j^O or ϕ_j, ψ_j into the global system.

To reduce numerical noise, the materials are made slightly lossy by adding a small imaginary component ω^I to the angular frequency. If seismograms are calculated by Fourier synthesis, the true amplitude is recovered by a multiplication with $e^{\omega_I t}$.

NUMERICAL RESULTS: ACOUSTICS

As a first test, we simply embed a homogeneous region in a homogeneous fullspace. The wavefield in the embedded region is modelled by FE. The wavefields in the fullspace are expanded into a MMP series. The material parameters in both regions are the same. Hence, all coefficients of the MMP expansion should be zero, while the FE solution should simply interpolate the incoming field. Clearly, due to the discretization of the field in the interior, the solution in the interior will deviate from the incident field and thus, an additional scattered field will be induced. The strength of this induced field is both a function of the number of elements per wavelength and the angle of incidence of the source field. The embedded region consists of $18 * 18$ elements, each $4m * 4m$ in size. The MMP expansion is (2) with $M = 4$ and $N = 4$. Altogether, 36 expansion functions are used. Figure 3 shows the exact position of node points and expansion centers. The source field is a plane wave, where the angle of incidence ranges from $0°$ up to $45°$. As a measure for the error, we use $< (P - P^{inc})/P^{inc}) >$ along the boundary of the inclusion. Starting with 250 elements per wavelength (EPW), the number of EPW is steadily decreased down to 2 EPW. The results are shown in Figure 4. As can be seen, the error increases slowly until the induced fields are of similar size to the source field. Using 10 EPW yields an error of about 5%. Also, the error becomes slightly smaller the more the incident plane wave propagates in the diagonal direction.

To test the accuracy of the MMP-FE technique, we compare the scattering from an acoustic cylinder with the well-known analytical series solution (Pao and Mow, 1973). The velocity inside the cylinder is 3000m/s; the velocity outside the cylinder the velocity is 2000m/s. In both regions, the density is kept constant at 2000kg/m^3. The radius a of the cylinder is 44m. To simplify the

generation of the FE mesh, a square region larger than the actual cylinder is discretized by 24 elements in either direction. Due to the symmetry of the problem, only one multipole (2), where $M = 1$ and $N = 20$, located at the origin, is used. The geometry is shown in Figure 5. The size of the elements is 4m. Two different wavelengths are used: 25m and 100m. Magnitude and phase are presented in Figures 6 and 7. In the case of $ka = 10$, the deviations of the FE-MMP solution from the analytical one are due to the finite element size. Reducing the element size reduces the deviations. Furthermore, the largest deviations correlate with the smallest magnitudes as can be observed in both Figures 6 and 7. This is an effect of the least-squares solving procedure. The solver uniformly minimizes the misfit at each boundary point. Thus, if the average misfit is ϵ, any true field value smaller than ϵ is lost in the misfit. If better accuracy is desired, the solution should be calculated again with the equations scaled by the reciprocal field obtained before. Basically, $\mathbf{A}^{OI}$ and $\mathbf{A}^{OO}$ should be scaled by $\frac{1}{p_i}$. Further details on scaling can be found in the prior paper (Imhof, 1995a).

Lastly, we calculate the seismogram for a complex geometry depicted in Figure 8. The scatterers are roughly 180m long and 35m thick. The velocity and density in the background are 2000m/s and 2000kg/m^3, respectively. The velocity and the density in the two scatterers are 3000m/s and 2000kg/m^3, respectively. Each finite element is 3m by 3m in size. For each scatterer, five centers of expansion are used. At each center $\mathbf{x}_m$, an expansion of the form

$$\sum_{n=-8}^{8} p_{mn}^O e^{in\varphi} H_{|n|}^{(1)} \left(k_O \left| \mathbf{x} - \mathbf{x}_m \right| \right)$$

is set up. The incident field p^{inc} is an explosive line source modulated with a Ricker wavelet (Ricker, 1977) of 50 Hz center frequency. Altogether, 64 receivers will measure the pressure of the scattered field. The resulting seismogram is shown in Figure 9.

NUMERICAL RESULTS: ELASTICS

As in the acoustic case, the first test is to embed a homogeneous region in a homogeneous fullspace. The wavefields in the embedded region are modelled by FE, while the wavefields in the fullspace are expanded into a MMP series. Because the material parameters in both regions are the same, all coefficients of the MMP expansion should be zero and the FE solution should perfectly interpolate the incoming field. Clearly, due to the discretization of the fields in the interior, the solution will

deviate from the incident field and thus, additional scattered fields will be induced. The strength of these induced fields is both a function of the number of elements per wavelength and the angle of incidence of the source field. The embedded region consists of $18 * 18$ square elements, each $4m * 4m$ in size. The MMP expansion is the same as (29) with $M = 4$ and $N = 4$. Altogether, $2 * 36$ expansion functions are used. Figure 3 shows the exact position of node points and expansion centers.

As source fields, we use plane waves of purely P or S polarization. Either experiment is performed twice, first for an angle of incidence of $0°$, then $45°$. Scanning through a range of frequencies allows is to see how polarization, orientation of the elements, and the number of elements per wavelength affect the solution. As a measure for the error, we use $< (|\mathbf{w} - \mathbf{w}^{inc}|)/|\mathbf{w}^{inc}| >$ along the boundary of the inclusion. Again, we start with 250 elements per P-wavelength (EPW) and decrease the number of EPW down to 2. The results are shown in Figure 10. As expected, the errors increase with increasing frequency. Interestingly, incident S waves of very low frequency are less affected than incident P waves of the same frequency. But with increasing frequency, the rate with which the error grows is larger for incident S- than incident P-waves. If less than 5 EPW are used, the S-waves are aliased and the results become meaningless. In general, waves incident at $45°$ are less affected by the grid size than waves incident in the normal direction. Using 25 EPW yields an error of about 8%.

To test the accuracy of the MMP-FE technique in the elastic case, we compare the scattering from a cylinder with the analytical series solution (Pao and Mow, 1973). Inside the cylinder, the P-velocity is 3000m/s and the S-velocity is 1700m/s. Outside the cylinder the P-velocity is 2000m/s and the S-velocity is 1300m/s. In both regions, the density is 2000kg/m^3 and the Poisson's ratio is $\frac{1}{4}$. The radius a of the cylinder is 12m. To simplify the generation of the FE mesh, a square region larger than the actual cylinder is discretized by 24 elements in either direction. Due to the symmetry of the problem, only one multipole (29), where $M = 1$ and $N = 20$, located at the origin, is used. The geometry is shown in Figure 5. The size of the elements is 1m. The wavelength of the incident P-wave is 50m and the wavelength of the incident S-wave is 32m. The magnitude and phase of the u and the v components are shown in Figures 11 and 12. For all incident phases, the match between the analytical solution and the results obtained from the MMP-FE method are excellent.

Lastly, we calculate the seismogram for a complex geometry depicted in Figure 13. A scatterer is illuminated by a line source. The scatterer is roughly 180m long and 35m thick. The P- and S-velocities and density in the background are 2000m/s, 1300m/s and 2000kg/m^3, respectively. The P- and S-velocities and density in the scatterer are 3000m/s, 1730m/s and 2000kg/m^3, respectively. The Poisson's ratio is $\sigma = 0.25$ in both the scatterer and in the background. Each finite element is 2m by 2m in size. In the scatterer, five expansions of the form (29) with $M = 5$ and $N = 7$ are used. Two different incident fields are chosen: a compressional and a rotational line source. Each source is modulated with a Ricker wavelet (Ricker, 1977) of 50 Hz center frequency. Altogether, 64 receivers measure the vertical displacement component of the total field. The resulting seismograms are shown in Figures 14 and 15.

SUMMARY

The MMP code has been successfully coupled with the FE method in both acoustic and elastic media. The coupling of the two methods enhances their usefulness for a range of problems. The FE technique allows the simulation of wave propagation in heterogeneous materials. The MMP expansions allow to calculate propagating waves in homogeneous (unbounded) regions in an efficient manner because they commonly need less unknowns to be evaluated and solved for than comparable methods.

Steady-state solutions, as well as seismograms obtained by Fourier synthesis, were calculated for a range of different problems for both acoustic and elastic media. Where available, the solutions obtained by the combined MMP-FEM scheme compared favorably with the analytical solutions.

The combined scheme compensates for the individual weaknesses of MMP and FEM and takes advantage of both their strengths. Thus, the method is well-suited to solve two-dimensional scattering problems for a range of problems which neither method could handle alone.

ACKNOWLEDGMENTS

REFERENCES

Dubus, B., Coupling finite element and boundary element methods on a mixed solid-fluid / fluid-fluid boundary for radiation or scattering problems, *J. Acoust. Soc. Am., 96,* 3792–3799, 1994.

Hafner, C., *The generalized Multipole Technique for Computational Electromagnetics,* Artech House, Inc., Boston, 1990.

Hestenes, M.R. and E. Stiefel, Methods of conjugate gradients for solving linear systems, *J. Res. National Bureau of Standards, 49,* 409–436, 1952.

Imhof, M.G., Multiple multipole expansions for acoustic scattering, *J. Acoust. Soc. Am., 97,* 754–763, 1995a.

Imhof, M.G., Multiple multipole expansions for elastic scattering, submitted to *J. Acoust. Soc. Am.,* 1995b.

Kelly, K.R., R.W. Ward, S. Treitel, and R.M. Alford, Synthetic seismograms: a finite difference approach, *Geophysics, 41,* 2–27, 1976.

Marfurt, K.J., Accuracy of finite-difference and finite-element modeling of the scalar and elastic wave equations, *Geophysics, 49,* 533–549, 1984.

Murphy, J.E. and S.A. Chin-Bing, A finite-element model for ocean acoustic propagation and scattering, *J. Acoust. Soc. Am., 86,* 1478–1483, 1989.

Murphy, J.E. and S.A. Chin-Bing, A seismo-acoustic finite element model for underwater acoustic propagation, in *Shear Waves in Marine Sediments,* J.M. Hovem, M.D. Richardson, and R.D. Stoll (eds.), Kluwer Academic Publishers, 463–470, Boston, 1991.

Pao, Y.H. and C.C. Mow, *Diffraction of Elastic Waves and Dynamic Stress Concentrations,* The Rand Corporation, New York, 1973.

Ricker, N.H., *Transient Waves in Visco-Elastic Media,* Elsevier Scientific Publishers, Amsterdam, 1977,

Schuster, G.T. and L.C. Smith, A comparison among four direct boundary integral methods, *J. Acoust. Soc. Am. 77* 850–864, 1985.

Schwarz, H.R., *Finite Element Methods,* Academic Press, San Diego, 1988.

Schwarz, H.R., *Numerical Analysis,* Wiley, New York, 1989.

Su, J.H., V.V. Varandan, and V.K. Varandan, Finite element eigenfunction method (feem) for elastic (sh) wave scattering, *J. Acoust. Soc. Am., 73,* 1499–1504, 1983.

Virieux, J., P-SV wave propagation in heterogeneous media: Velocity stress finite difference method, *Geophysics, 51,* 889–901, 1986.

Waterman, P.C., New formulation of acoustic scattering, *J. Acoust. Soc. Am., 45,* 1417–1429, 1969.

Waterman, P.C., Matrix theory of elastic wave scattering, *J. Acoust. Soc. Am., 60,* 567–580, 1976.

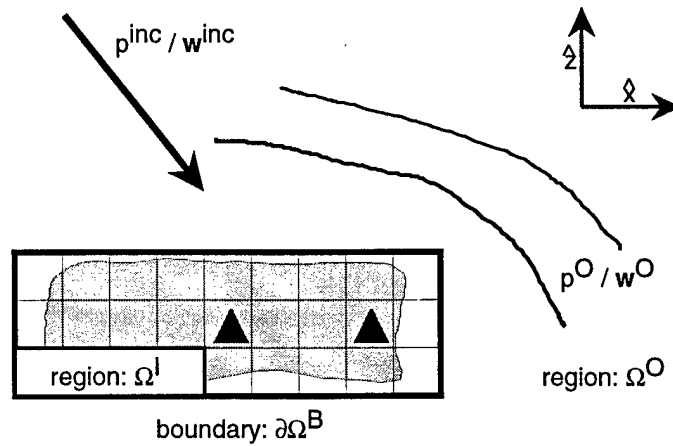Zienkiewicz, O.C., *The Finite Element Method,* McGraw-Hill, New York, 1977.

Figure 1: The generic scattering problem to be solved by the hybrid MMP-FEM technique. A heterogeneous scatterer Ω^I is embedded in a homogeneous background Ω^O. In the acoustic case, the incident field is p^{inc} and the scattered field is p^O. In the elastic case, the incident field is $\mathbf{w}^{inc}$ and the scattered field $\mathbf{w}^O$. The triangles symbolize expansion centers for the MMP.
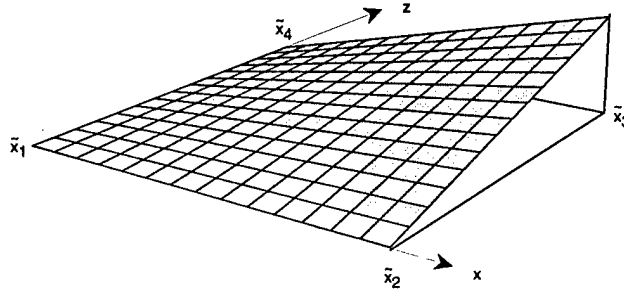
Figure 2: The shape function $\tilde{N}_3(\mathbf{x}) = xz$ for a square unit element $\tilde{\Omega}$ and bilinear interpolation. The other shape functions $\tilde{N}_1(\mathbf{x})$, $\tilde{N}_2(\mathbf{x})$ and $\tilde{N}_4(\mathbf{x})$ are obtained by rotations of $-180°$, $-90°$ and $90°$, respectively.
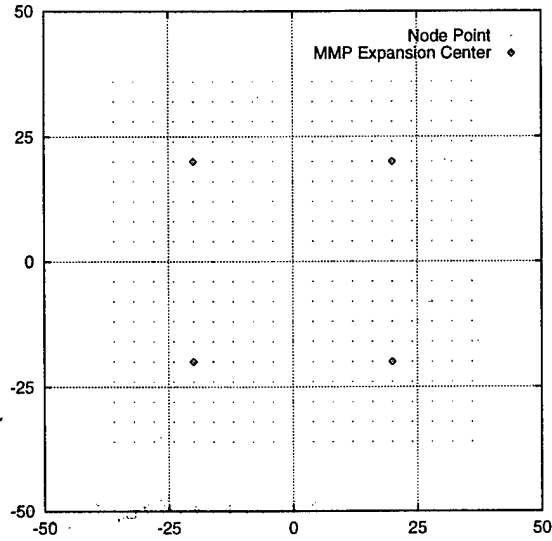

Figure 3: An embedded homogeneous region. Each dot represents a node point and each diamond a MMP expansion center. From each expansion center $\vec{x}_m$, we set up an expansion $\sum_{n=-4}^{4} p_{mn}^O e^{in\varphi} H_{|n|}^{(1)} (k_O |\vec{x} - \vec{x}_m|)$.

81
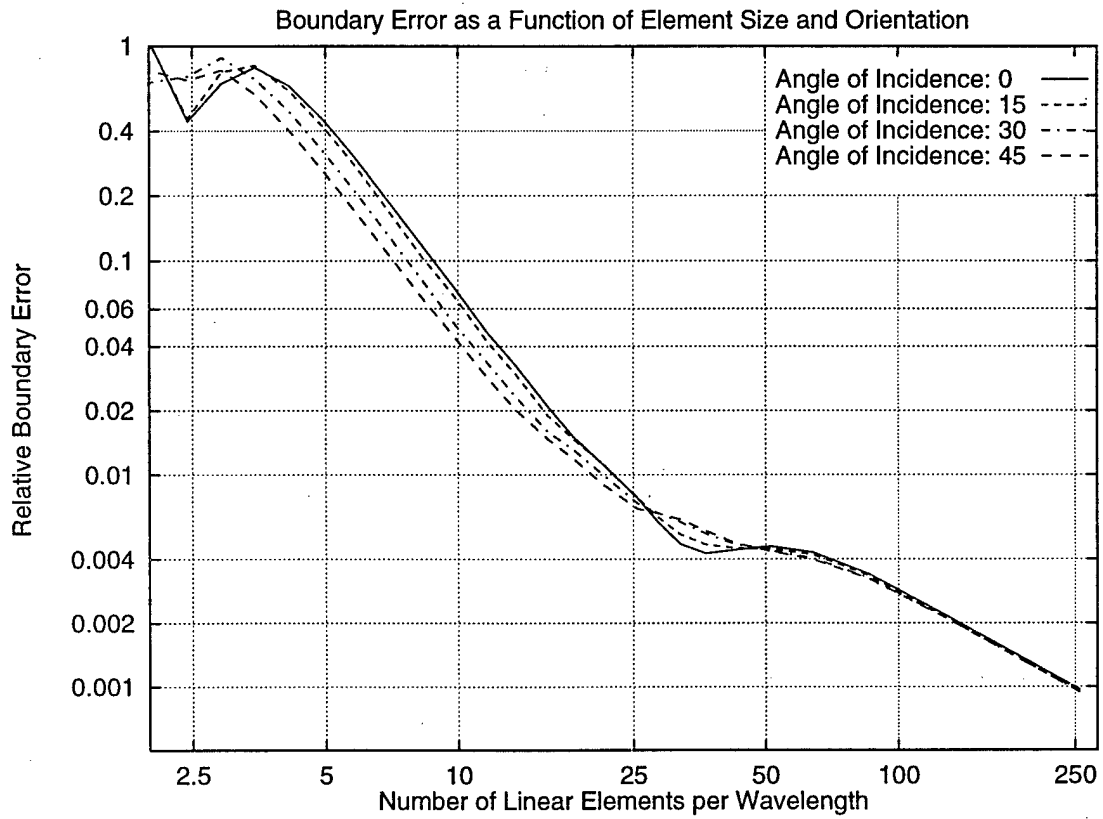
Figure 4: Relative boundary error $< (P - P^{inc})/P^{inc} >$ as a function of the number of elements per wavelength (EPW) and propagation angle of the incident field with respect to the finite elements. 10 EPW yields an error of 5%. Waves propagating diagonally are less affected by larger element sizes.
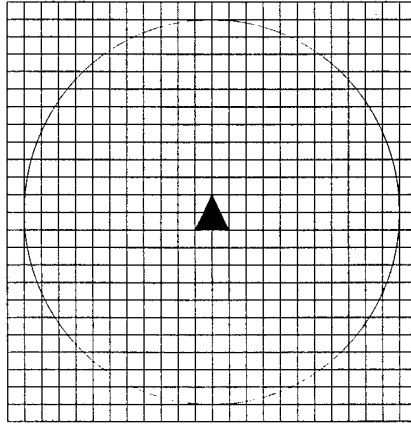
Figure 5: A cylindrical scatterer is illuminated by a plane wave. Outside, the velocity is 2000m/s; inside, the velocity is 3000m/s. The grid represents the finite elements used. The grid spacing is 4m and the radius of the cylinder is 44m. The triangle denotes the expansion center for the multipole.
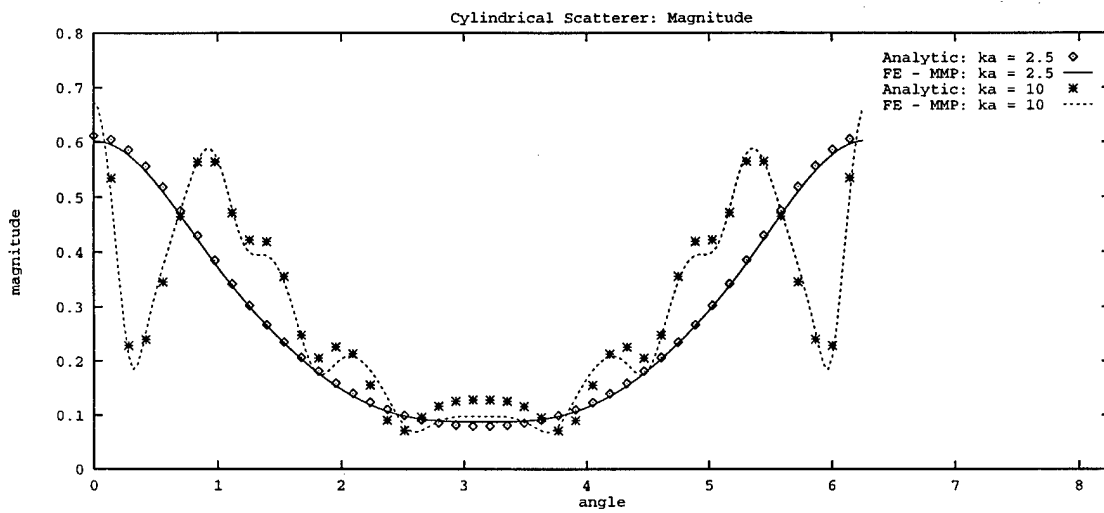

Figure 6: A cylindrical scatterer is illuminated by a plane wave propagating in the positive, horizontal direction. Shown is the magnitude $|P|$ for $ka = 2.5$ and $ka = 10$ as a function of angle.
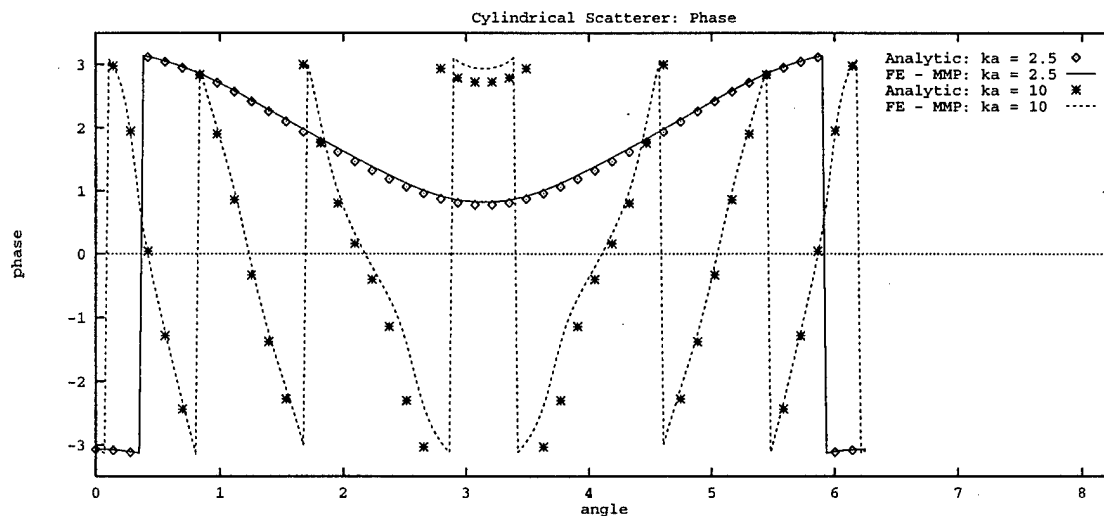
Cylindrical Scatterer: Phase

Figure 7: A cylindrical scatterer is illuminated by a plane wave propagating in the positive, horizontal direction. Shown is the phase $\arg(P)$ for $ka = 2.5$ and $ka = 10$ as a function of angle.
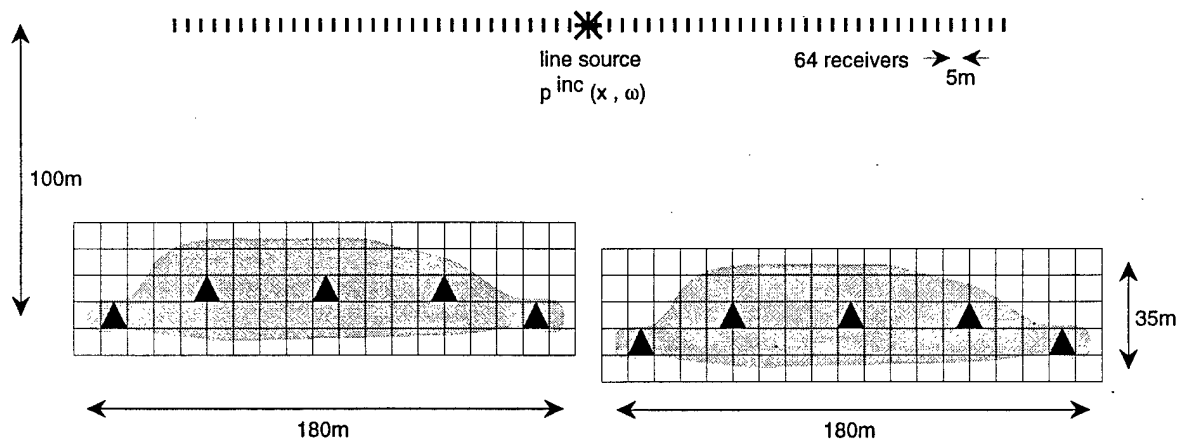

Figure 8: Generic scatterers used to calculate seismograms. Two homogeneous scatterers are embedded in a homogeneous background. The velocity and the density in the background are 2000m/s and 2000kg/m^3, respectively. The velocity and the density in the two scatterers are 3000m/s and 2000kg/m^3, respectively. The triangles show the location of the centers for the MMP expansion.
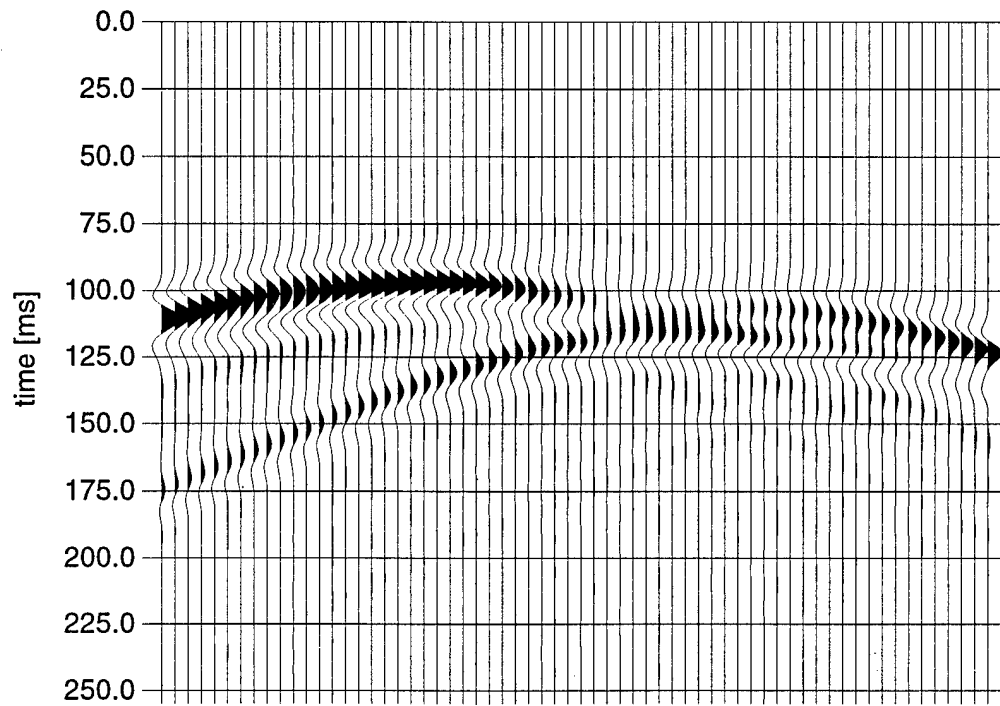
84

Figure 9: The resulting seismogram for the complex geometry depicted in Figure 8.
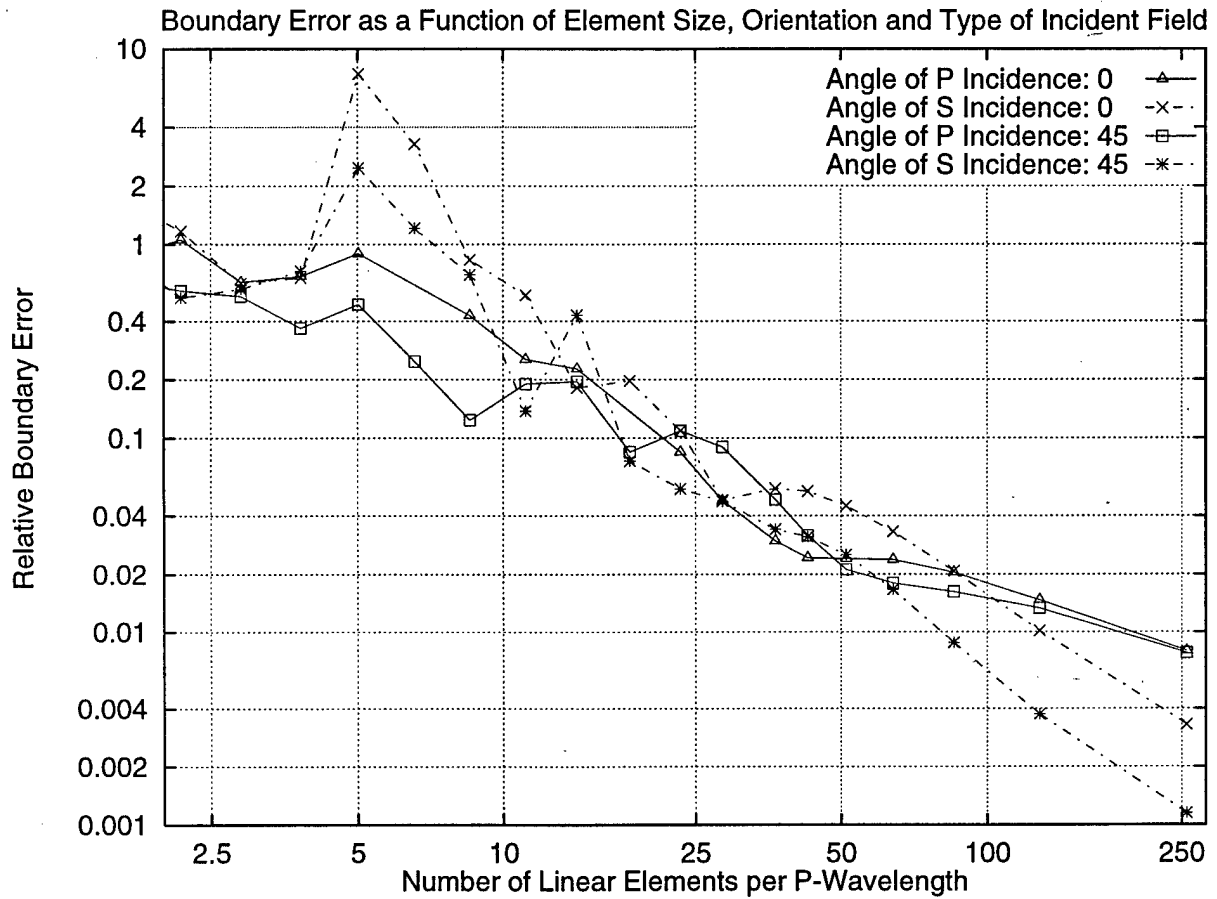
Figure 10: Relative boundary error $< |w - w^{inc}|/|w^{inc}| >$ as a function of the number of elements per P-wavelength (EPW) and propagation angle of the type of incident field with respect to the finite elements. 25 EPW yields an error of 8%. Waves propagating diagonally are less affected by larger element sizes. Also, an incident S wave is more affected by the element size because its wavelength is roughly half as long as the corresponding P wave's.
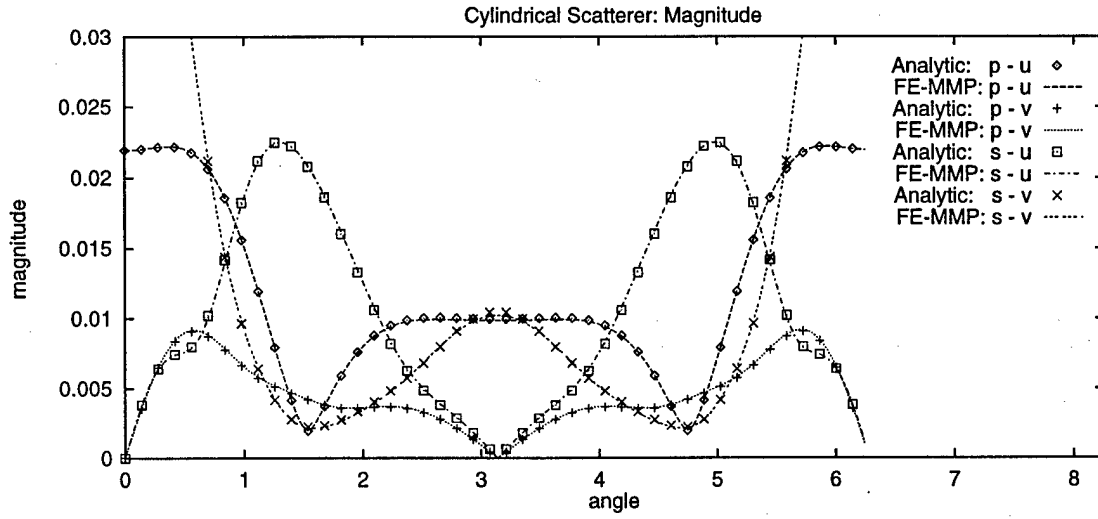
Figure 11: A cylindrical scatterer is illuminated by a plane wave propagating in the positive, horizontal direction. Both P and S modes are used as incident fields. Shown are the magnitude of $|u|$ and $|v|$ for $ka = 1.5$ and $la = 2.3$ as a function of angle.
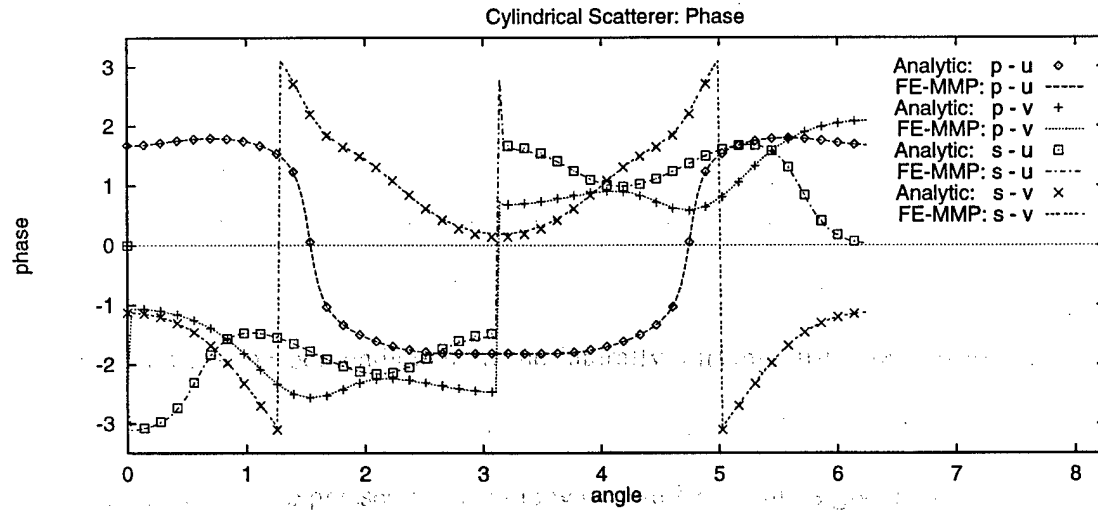

Figure 12: A cylindrical scatterer is illuminated by a plane wave propagating in the positive, horizontal direction. Both P and S modes are used as incident fields. Shown are the magnitude of $\arg(u)$ and $\arg(v)$ for $ka = 1.5$ and $la = 2.3$ as a function of angle.
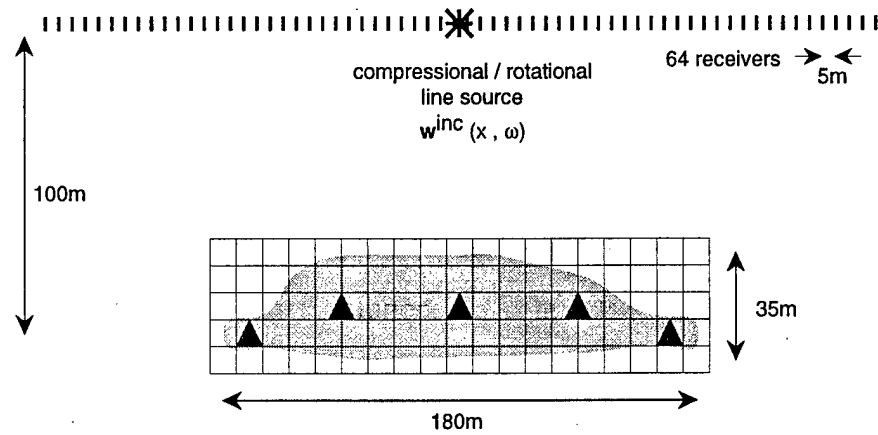
Figure 13: Generic scatterer used to calculate elastic seismograms. The scatterer is embedded in a homogeneous background. The P- and S-velocities and density in the background are 2000m/s, 1300m/s and 2000kg/m^3, respectively. The P- and S-velocities and density in the scatterer are 3000m/s, 1730m/s and 2000kg/m^3, respectively. Thus, Poison's ratio in the scatter is the same as in the background. The triangles show the location of the centers for the MMP expansion.

Figure 14: The vertical component of the seismogram for the complex geometry depicted in Figure 13. The incident field is a compressional line source.
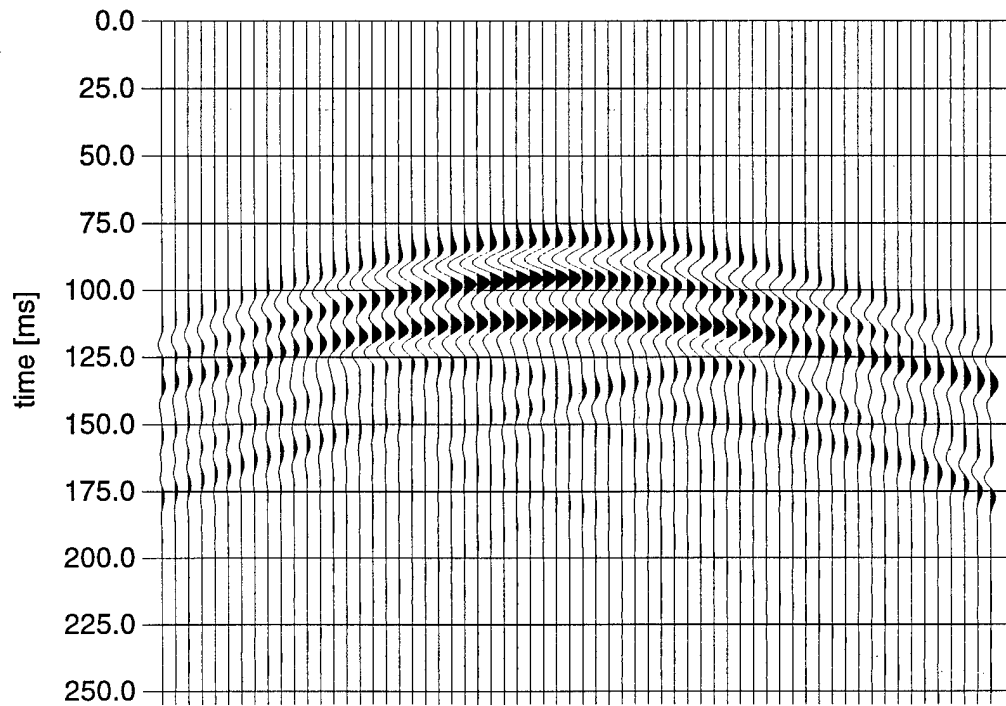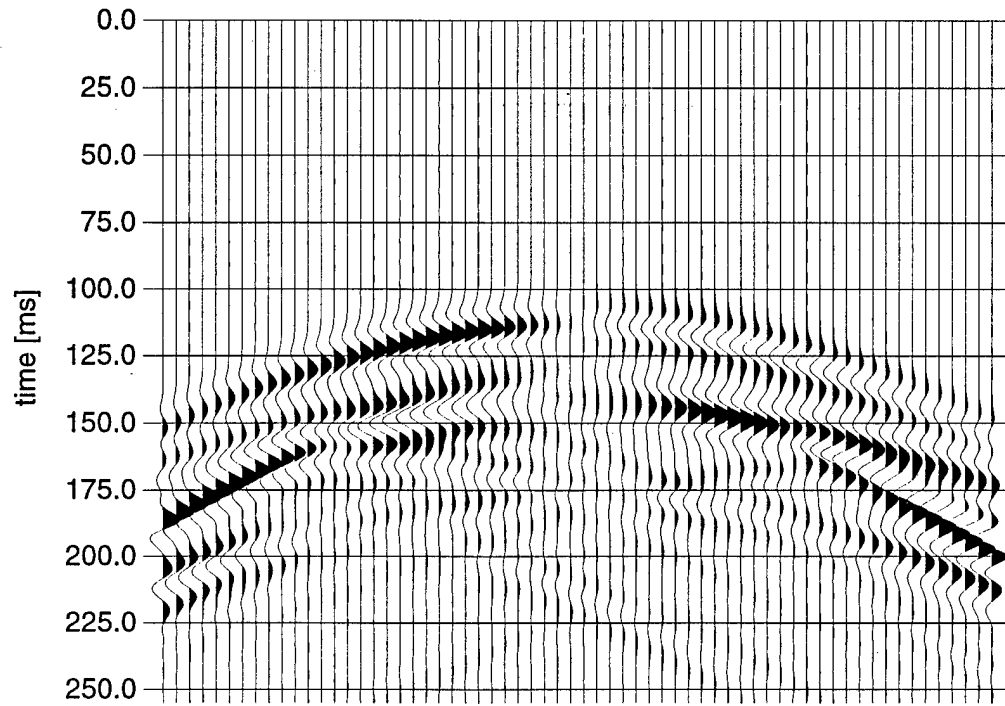
Figure 15: The vertical component of the seismogram for the complex geometry depicted in Figure 13. The incident field is a rotational line source.

A COMPARISON OF SCATTERING FROM 2-D AND 3-D ROUGH INTERFACE

Ningya Cheng, Craig A. Schultz, and M. Nafi Toksöz
Earth Resources Laboratory
Department of Earth, Atmospheric, and Planetary Sciences
Massachusetts Institute of Technology
Cambridge, MA 02139

ABSTRACT

In this paper we compared scattered waves from 2-D and 3-D interface structures. The modeling technique is the 3-D time domain finite difference method. The scheme is second-order accurate in time and fourth-order accurate in space. It is implemented on a massively parallel nCUBE computer. In order to investigate the characteristics of 2-D and 3-D rough surface scattering, we consider an acoustic-elastic boundary, which is described by a Gaussian autocorrelation function. The F-K analysis of reflected signals shows that 2-D scattering generates similar amounts of forward and back scattering, while in the 3-D case, more forward and less back scattering. The 3-D effects also show larger reflected energy than the 2-D case, especially near the normal incident. The out-of-plane scatterings are clearly demonstrated on the F-K spectra in the 3-D case. In the 2-D simulations, we have to keep in mind that it tends to overestimate the amount of backscattering energy.

91

INTRODUCTION

Many boundaries in the Earth may be characterized as irregular interfaces, such as the ocean floor, the Moho discontinuity, and surface terrain. The wave scattering from interfaces has become a subject of wide interest. The effects of scattering on the observations can often be identified on amplitudes, traveltimes, spectra, and waveforms. Although scattering from smooth interfaces is easily modeled and well-understood, the roughness inherent in many natural interfaces introduces an incoherent component into the wavefield, which is poorly understood. A number of theoretical approaches have been developed to help us understand the rough interface scattering problem. Reviews of these works were given by Ogilvy (1987) and Thorsos and Jackson (1989). These studies are based on the perturbation method. They require interface properties, such as the overall topography (amplitude and slope), to be small compared with the incident wavelength. Under the approximation these studies give analytical solutions to the problems. Full-waveform techniques, such as the boundary integral method, are implemented to model completely the wave interaction with the interface topography (Bouchon, 1985; Kawase, 1988; Gerstoft and Schmidt, 1991; Sanchez-Sesma and Campillo, 1991). The finite difference method has also become effective in studying scattering from a rough interface (Lavender and Hill, 1985; Burns and Stephen, 1990; Dougherty and Stephen, 1991; Fricke, 1993).

Most numerical modelings have focused on two-dimensional models, such as the ocean floor, ice sheet, and shallow crust. These 2-D simulations have demonstrated the basic effects of scattering and wave conversions at interfaces. Nature boundaries, however, are three dimensional. The 3-D scattering features, such as the out-of-plane effect, cannot be addressed adequately by 2-D modeling. It is important to understand the difference between 2-D and 3-D surface scattering. This knowledge can help us assess the limitations of 2-D modeling. It is the purpose of this paper to show an example of the differences between 2-D and 3-D rough surface scattering. We chose the finite difference method as the modeling technique. The finite difference method can propagate complete wave fields through arbitrarily complex media. However, the finite difference method is very computationally intensive, especially for the 3-D problem. Parallel computing makes the finite difference method a very attractive choice. The massively parallel computer is used in this paper to implement the 3-D finite difference scheme. We chose the rough interface as an acoustic-elastic boundary. The interface is changed from 1-D (flat) to 2-D (variation in one direction) and to 3-D

(variations in two directions) to do the numerical simulations. This enables us to compare the scattering from 2-D and 3-D rough surfaces directly.

3-D FINITE DIFFERENCE METHOD

Wave propagation in elastic media can be described by first-order hyperbolic equations in a Cartesian coordinate as:

$$
\begin{aligned}
\rho \frac{\partial v_x}{\partial t} &= \frac{\partial \tau_{xx}}{\partial x} + \frac{\partial \tau_{xy}}{\partial y} + \frac{\partial \tau_{xz}}{\partial z} \\
\rho \frac{\partial v_y}{\partial t} &= \frac{\partial \tau_{xy}}{\partial x} + \frac{\partial \tau_{yy}}{\partial y} + \frac{\partial \tau_{yz}}{\partial z} \\
\rho \frac{\partial v_z}{\partial t} &= \frac{\partial \tau_{xz}}{\partial x} + \frac{\partial \tau_{yz}}{\partial y} + \frac{\partial \tau_{zz}}{\partial z}
\end{aligned}
\tag{1}
$$

and

$$
\begin{aligned}
\frac{\partial \tau_{xx}}{\partial t} &= (\lambda + 2\mu)\frac{\partial v_x}{\partial x} + \lambda\frac{\partial v_y}{\partial y} + \lambda\frac{\partial v_z}{\partial z} \\
\frac{\partial \tau_{yy}}{\partial t} &= \lambda\frac{\partial v_x}{\partial x} + (\lambda + 2\mu)\frac{\partial v_y}{\partial y} + \lambda\frac{\partial v_z}{\partial z} \\
\frac{\partial \tau_{zz}}{\partial t} &= \lambda\frac{\partial v_x}{\partial x} + \lambda\frac{\partial v_y}{\partial y} + (\lambda + 2\mu)\frac{\partial v_z}{\partial z} \\
\frac{\partial \tau_{xy}}{\partial t} &= \mu(\frac{\partial v_x}{\partial y} + \frac{\partial v_y}{\partial x}) \\
\frac{\partial \tau_{xz}}{\partial t} &= \mu(\frac{\partial v_x}{\partial z} + \frac{\partial v_z}{\partial x}) \\
\frac{\partial \tau_{yz}}{\partial t} &= \mu(\frac{\partial v_y}{\partial z} + \frac{\partial v_z}{\partial y})
\end{aligned}
\tag{2}
$$

where v is velocity, ρ is density, and τ is stress. λ and μ are Lamé constants. The reason for formulating the second-order wave equations into the first-order hyperbolic system of equations is that once this system is discretized on a staggered grid, it is valid for any Poisson's ratio (Virieux, 1986). The fluid-solid boundary can be treated simply by setting shear modulus to zero.

The first-order hyperbolic equations (1) and (2) are discretized on a staggered grid (Madariaga, 1976), which is shown in Figure 1.We approximate the first-order time derivative by second order centered finite difference and the first-order spatial derivatives by fourth-order centered finite difference. The media parameters ρ, λ and μ are given at the grid point where the normal stresses $\tau_{xx}, \tau_{yy}, \tau_{zz}$ are assigned (see Figure 1).In the calculation to update velocities, the needed density

values are obtained from the average of the two assigned densities nearby. The shear moduli used to update the shear stress are determined by the harmonic average of the four shear moduli nearby instead of the arithmetic average (Kostek, 1991). This harmonic average method can automatically put the shear modulus zero at the fluid-solid boundary.

The dispersion analysis shows that the fourth-order finite difference has much less dispersion and grid anisotropy than the second-order one for both P and S waves. The rule of thumb is that we need five samples per wavelength for the fourth-order finite difference to control the dispersion and the anisotropy at less than 1%. The stability condition of the scheme is given by (Cheng, 1994)

$$\Delta t < \frac{\Delta}{\sqrt{3}\alpha(|\eta_1| + |\eta_2|)} \qquad (3)$$

under the condition of grid size $\Delta x = \Delta y = \Delta z = \Delta$, where $\eta_1 = \frac{9}{8}$ and $\eta_2 = -\frac{1}{24}$ are the coefficients of the fourth-order finite difference approximation to the first-order derivative. α is the maximum P wave velocity in the model. The absorbing boundary condition is applied to the outside boundaries of the grid to minimize the reflections. Higdon's absorbing boundary condition is used (Higdon, 1990).

Parallel computing provides a new means to overcome the limitations of the memory and the speed of a single processor. In the finite difference method all the calculations involve only local interactions of the velocities and stresses. For example, in the fourth-order finite difference scheme only two nearby grid points data are needed to update the current grid point. This can be efficiently executed on a multiple instruction and multiple data (MIMD) parallel computer. A staggered-grid fourth-order finite difference scheme discussed above is paralleled on nCUBE 2S massively parallel computer (Cheng, 1994).

NUMERICAL EXAMPLES AND F-K ANALYSIS

Test of the Finite Difference Method

We consider a fluid-filled cylindrical borehole embedded in a homogeneous elastic formation. The finite difference results are compared with the discrete wavenumber method. The physical property of the fluid and solid are listed in Table 1. The borehole radius is 0.1 m. A point explosion source and the pressure receivers are located at the center of the borehole. The Kelly wavelet at center

frequency 14 kHz is used as the source time function (Kelly *et al.*, 1976). A grid size of 0.01 m and a time step of 0.001 ms were chosen. The second-order Higdon's absorbing boundary condition is used to reduce the artificial boundary reflections. The local P and S wave velocities are used at the absorbing boundary. A grid of $70 \times 70 \times 200$ is used to build the borehole model. The finite difference results are compared with the discrete wavenumber solutions (Cheng and Toksöz, 1981) in Figure 2.There are body waves (refracted P and S) and guided waves (Stoneley and pseudo-Rayleigh) propagated inside the borehole. The comparison shows excellent agreement between the two solutions. This test shows the finite difference scheme handled the sharp fluid-solid boundary very well. Even if the borehole is approximated by a rough edged circle in the finite difference method, we still can get a good match between the two methods.

Synthetic Reflection Data

In order to investigate the reflection characteristics from the rough surface, we consider an irregular fluid-solid interface. There are only reflected P waves in the fluid. This will greatly simplify the analysis of reflected signals. The property of the fluid and the solid are listed in Table 1 and a 3-D view of the model is shown in Figure 3.The source time function of a point explosion is a Kelly wavelet with a center frequency of 15 Hz. We choose the grid discretization interval to be one-tenth the shortest wavelength at the source center frequency, which is 100 m. The time step is 0.001 s and the size of the model is $200 \times 200 \times 100$.

In this study, we place a 2-D pressure receiver array (64×64) in a plane parallel to the interface and on one side of the source. The array receiver spacing is 20 m. We adopt a Gaussian surface to describe the fluid and solid boundary. It has a Gaussian spatial correlation function and a Gaussian distribution about the mean (Frankel and Clayton, 1986). This interface can be described by two properties: the correlation length, a, and the standard deviation in height, δ. The correlation length corresponds to the average distance between nearby peaks and valleys along the interface, and the standard deviation gives the root mean square (rms) deviation of the interface height from its mean, which is set to zero. The rms slope ϕ of the interface is given by

$$\tan(\phi) = \sqrt{2}\frac{\delta}{a} \tag{4}$$

where the correlation length is set equal to the central incident wavelength (100 m) and rms slope is set at 30 °.

A 3-D rough surface is introduced with the correlation length in the X and Y direction both equal to 100 m, while the 2-D rough interface has a correlation length in the X direction of 100 m, and of ∞ in the Y direction. The 2-D Gaussian rough surface is plotted in Figure 4b.and the 3-D rough surface is plotted in Figure 4b.The 2-D rough surface is inherited from the 3-D one. It is simply obtained by extending the 3-D rough surface at Y=1 in the Y direction. This will make the amplitude comparison interesting later. In that case we obtain the amplitudes from 3-D scattering at the plane which has the exactly same surface profile as the 2-D one. The source-receiver plane is 600 m above the mean height of the rough interface.

We have calculated the synthetic data set first for a flat interface, as shown in Figure 5a.Figures 5b and c show the seismogram obtained from 2-D and 3-D rough interface models. These plots are a 2-D slice of the 3-D data set for fixed Y. The direct arrivals from the finite difference calculation are removed, and they are not shown in the plots. The coda waves in Figures 5b and c show the effect of the rough interface. The coda generated from the 2-D rough interface have more structures than the 3-D one. Also the clear reflections from the flat interface are smeared in the 2-D and 3-D rough surface cases. The F-K analysis of the reflected signals will follow.

F-K Analysis of the Reflected Data

F-K analysis is a useful technique to illustrate the magnitude and direction of energy arriving at the array. It is widely used in the seismic coda analysis, and Dainty and Toksöz (1990) give a good summary of this approach. In this case we use a simple 3-D Fourier transform algorithm on the synthetic data, transforming in both spatial directions, and in time. The data is displayed at a given frequency to show the magnitude and direction of the scattered waves. The source center frequency will be of interest here. Before we analyze the reflected data from the interfaces, we first look at the direct arrivals (Figure 6a).The direct arrivals are propagated straight from the source to the receivers on the same plane. A radius of 10 corresponds to the direct wave arriving with a horizontal phase velocity of 1.5 km/s at 15 Hz. Only half of the circle is shown on the figure. This is because the receivers are only on one side of the source. For the purpose of comparison the F-K spectra of the reflections from the flat surface is shown in Figure 6b. The small wavenumber range is because of the limited aperture of the receiver array.

Figures 6c and d give the F-K spectra for the seismograms recorded over the 2-D and 3-D

interfaces. The F-K spectra for the 2-D interface clearly shows that similar amounts of both backscattered and forward scattered energy are present in the seismogram. This distribution is in agreement with the numerical mean reflection coefficients presented for the 2-D interface by Schultz and Toksöz (1993a), which show similar amounts of both forward and back scattering. The structure of the spectra is parallel to the K_y just like the rough surface is parallel to the Y axis. The F-K spectra for the 3-D interface also shows a large amount of both forward and back scattered energy. However, the forward scattered energy appears to be dominant. This suggests that more forward scattering appears to exist. However, one must remember that it is possible for energy, which is diffracted back towards the seismic line from a side scatterer, to appear with a positive K_x wavenumber. Thus, in the 3-D case, out-of-plane scattering can give the appearance of more forward scattering and less backscattering. Nevertheless, these results appear to support the results of Schultz and Toksöz (1993b), which showed, based on experimental data, that 3-D interfaces tend to show a more rapid decrease in backscattering combined with a more rapid increase in forward scattering as an incident wave arrives at larger incident angles (with respect to the vertical). In the 3-D case the wide spread of energy in the F-K spectra clearly demonstrates the out-of-plane reflections.

Figure 7 gives the rms amplitude of the primary reflection versus incident angle. The seismogram section is taken from Y=1, where the 3-D and the 2-D surface have the same profile. The geometric spreading is compensated according to the flat interface. The rms amplitudes of the first cycle is shown in Figure 7a. The 2-D and 3-D rms amplitudes are similar, but they are both smaller than the flat interface amplitude. This is exactly what we expected. As we add more cycles into the rms amplitude (Figure 7b), more scattered energy is accounted for. It clearly shows that the extra degree of freedom associated with the 3-D interface geometry can result in a larger contribution of scattered energy. The 3-D variation of the interface topography results in a larger amplitude than the 2-D one near normally incident angles. This gives a first estimate of the scaling differences between the 2-D and 3-D reflection coefficients studied by Schultz (1994) in his thesis, where the rms amplitude from 2-D numerical calculations and 3-D ultrasonic experiments are compared. The out-of-plane contributions from 3-D topography also result in the amplitude being larger than the flat interface.

SUMMARY

The 3-D time domain finite difference method is used to investigate the rough fluid-solid interface scattering. The scheme is implemented on the nCUBE 2S massively parallel computer. The synthetic reflection data is analyzed by the F-K spectra. The 2-D scattering clearly shows the similar amount of forward and backward scattering, while in the 3-D case out-of-plane reflections give more forward scattering and less back scattering. The 3-D effects are also shown on the larger reflected rms amplitude than the 2-D case near normally incident angles. This is because of the contributions from out-of-plane scattering from 3-D topography. This 3-D out-of-plane scattering can be easily identified on the F-K spectra.

In this paper we only take a first step to demonstrate the difference of 2-D and 3-D surface scattering. More thorough investigations are needed. For example, we need to test a large amount of realizations of the interface to obtain statistical insight into 2-D and 3-D rough surface scattering. In our simulation we only consider the point source. To achieve high angular resolution of the reflection, we need to form a beam to the interface instead of the point source (Stephen and Swift, 1994). This will give us a more quantitative measure of the 2-D and 3-D reflection.

ACKNOWLEDGMENTS

REFERENCES

Bouchon, M., 1985, A simple, complete numerical solution to the problem of diffraction of SH waves by an irregular surface, *J. Acoust. Soc. Am.* 77. 1–5.

Burns, D.R. and Stephen, R.A., 1990, Three-dimensional numerical modeling of geoacoustic scattering from seafloor topography, *J. Acoust. Soc. Am., 88,* 2338–2345

Cheng, N., 1994, Borehole wave propagation in isotropic and anisotropic media: 3-D finite difference approach, *Ph.D. Thesis*, Massachusetts Institute of Technology, Cambridge, MA.

Cheng, C.H. and Toksöz, M.N., 1981, Elastic wave propagation in a fluid-filled borehole and synthetic acoustic logs, *Geophysics, 46,* 1042–1053.

Dainty, A.M. and Toksöz, M.N., 1990, Array analysis of seismic scattering, *Bull. Seis. Soc. Am., 80,* 2242–2260.

Dougherty, M.E. and Stephen, R.A., 1991, Seismo/acoustic propagation through rough seafloors *J. Acoust. Soc. Am., 90.* 2637–2651.

Frankel, A. and Clayton, R., 1986, Finite difference simulations of seismic scattering: Implications for the propagation of short-period seismic waves in the crust and models of crustal heterogeneity, *J. Geophys. Res., 91,* 6465–6489.

Fricke, J.R., 1993, Acoustic scattering from elemental arctic ice features: Numerical modeling results, *J. Acoust. Soc. Am., 93,* 1784–1796.

Gerstoft, P. and Schmidt, H., 1991, A boundary element approach to ocean seismoacoustic facet reverberation, *J. Acoust. Soc. Am., 89,* 1629–1642.

Higdon, R.L., 1990, Radiation boundary conditions for elastic wave propagation, *SIAM J. Numer. Anal., 27,* 831–870.

Kawase, H., 1988, Time-domain response of a semi-circular canyon for incident SV, P and Rayleigh waves calculated by the discrete wavenumber boundary element method, *Bull. Seis. Soc. Am., 78,* 1415–1437.

Kelly, K.R., Ward, R.W., Treitel, S., and Alford, R.M., 1976, Synthetic seismograms: A finite-difference approach, *Geophysics, 41,* 2–27.

Kostek, S., 1991, Modelling of elastic wave propagation in a fluid-filled borehole excited by a piezoelectric transducer, *Masters Thesis*, Massachusetts Institute of Technology, Cambridge, MA.

Lavender, A.R. and Hill, N.R., 1985, P-SV resonances in irregular low velocity surface layers, *Bull. Seism. Soc. Am., 75*, 847–864.

Madariaga, R., 1976, Dynamics of an expanding circular fault, *Bull. Seism. Soc. Am., 65*, 163–182.

Ogilvy, J.A., 1987, Wave scattering from rough surfaces, *Rep. Prog. Phys., 50*, 1553–1608.

Sanchez-Sesma, F.J. and Campillo, M., 1991, Diffraction of P, SV and Rayleigh waves by topographical features: A boundary integral formulation, *Bull. Seis. Soc. Am., 81*. 2234–2253.

Schultz, C.A., 1994, Enhanced backscattering of seismic waves from irregular interfaces, *Ph.D. Thesis*, Massachusetts Institute of Technology, Cambridge, MA.

Schultz, C.A. and Toksöz, M.N., 1993a, Enhanced backscattering of seismic waves from a highly irregular, random interface: SH case, *Geophys. J. Int., 114*. 91–102.

Schultz, C.A. and Toksöz, M.N., 1993b, Enhanced backscattering of seismic waves from a highly irregular, random interface: P-SV case, *Geophys. J. Int., 117*. 783–810.

Stephen, R.A. and Swift, S.A., 1994, Modeling seafloor geoacoustic interaction with a numerical scattering chamber, *J. Acous. Soc. Am., 96*, 973–990.

Thorsos, E.I. and Jackson, D.R., 1989, The validity of the perturbation approximation for rough surface scattering using a Gaussian roughness spectrum, *J. Acous. Soc. Am., 86*, 261–277.

Virieux, J., 1986, P-SV wave propagation in heterogeneous media: Velocity-stress finite difference method, *Geophysics, 51*, 889–901.

	P wave velocity α (m/s)	S wave velocity β (m/s)	density ρ (g/c.c.)
Fluid	1500	—	1.0
Solid	4000	2300	2.3

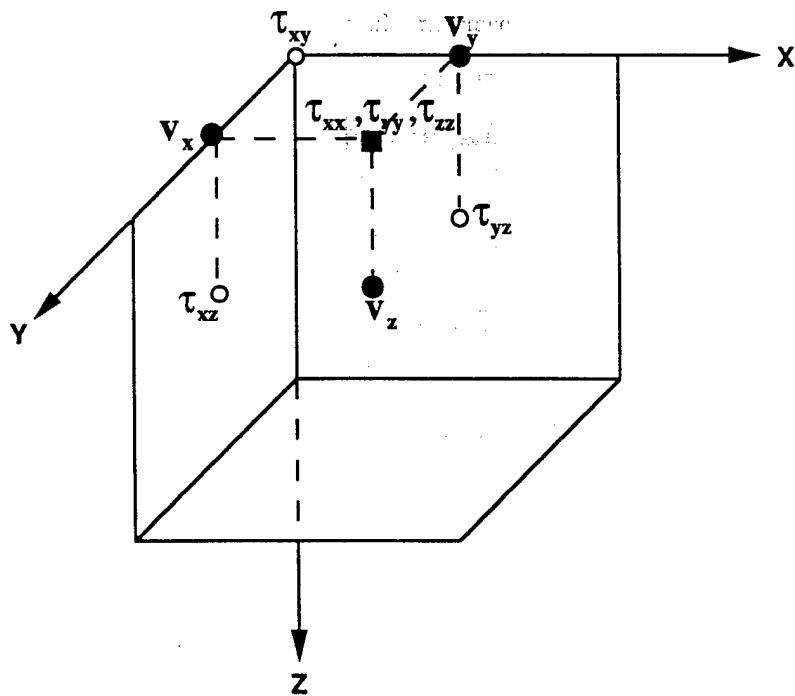Table 1: The velocity and the density values of the fluid and the solid.

Figure 1: Staggered grid used to discretize equations (2.5) and (2.6). Solid circles represent the velocities. Open circles represent the shear stresses. The solid square represents the normal stresses.
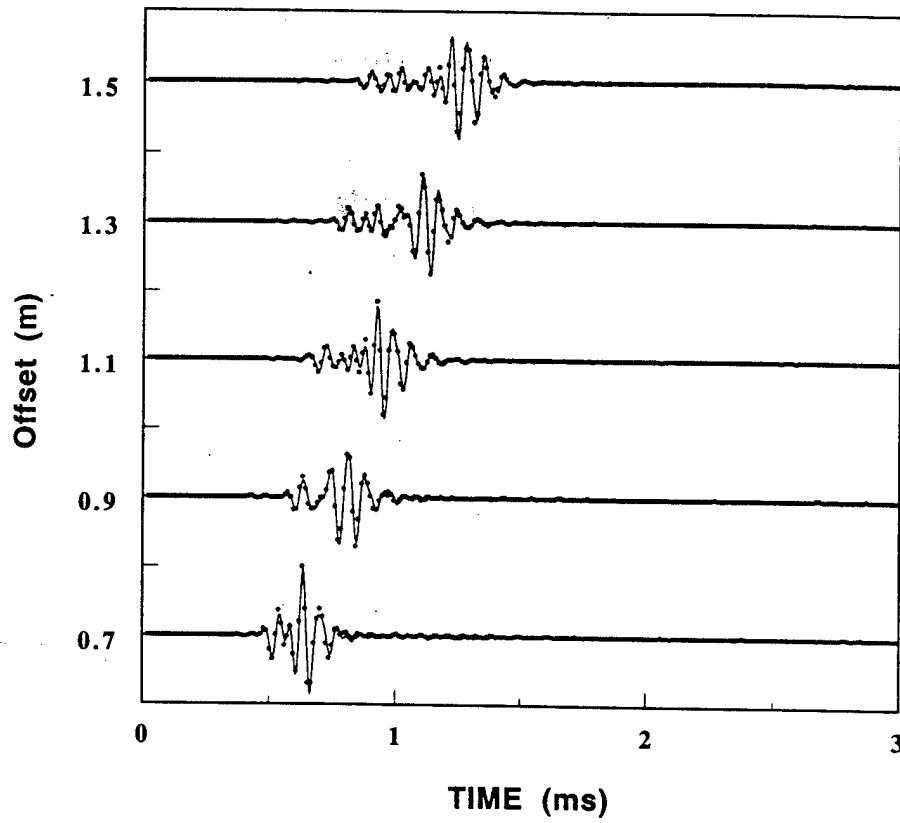
Figure 2: Comparison of the finite difference solutions (solid line) with the discrete wavenumber solutions (dot) in a fluid-filled borehole. The explosion source at center frequency 14 kHz is used. The amplitudes are normalized.
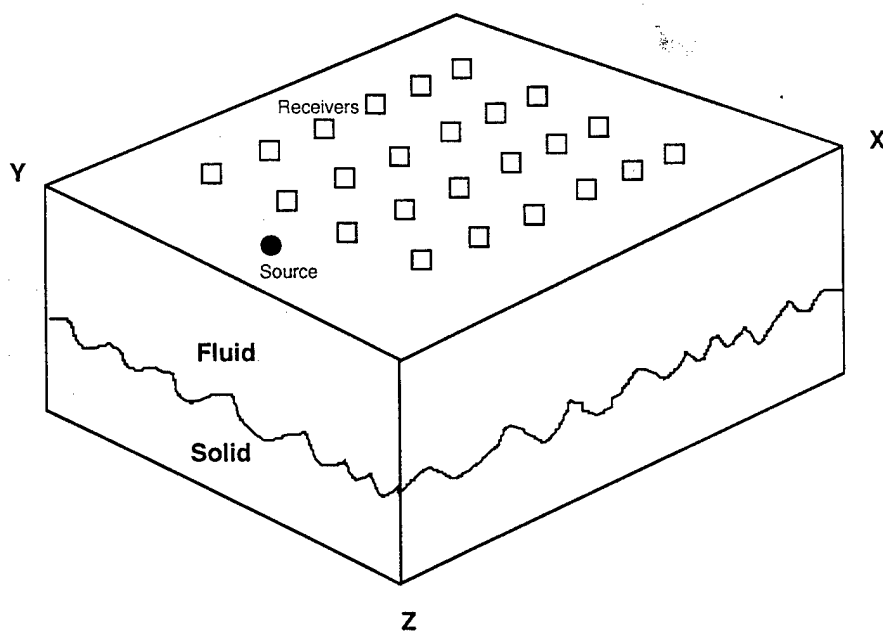
Figure 3: Schematic diagram of the model geometry used to compute the synthetic rough interface reflection data. The source-receiver arrangement is also shown.
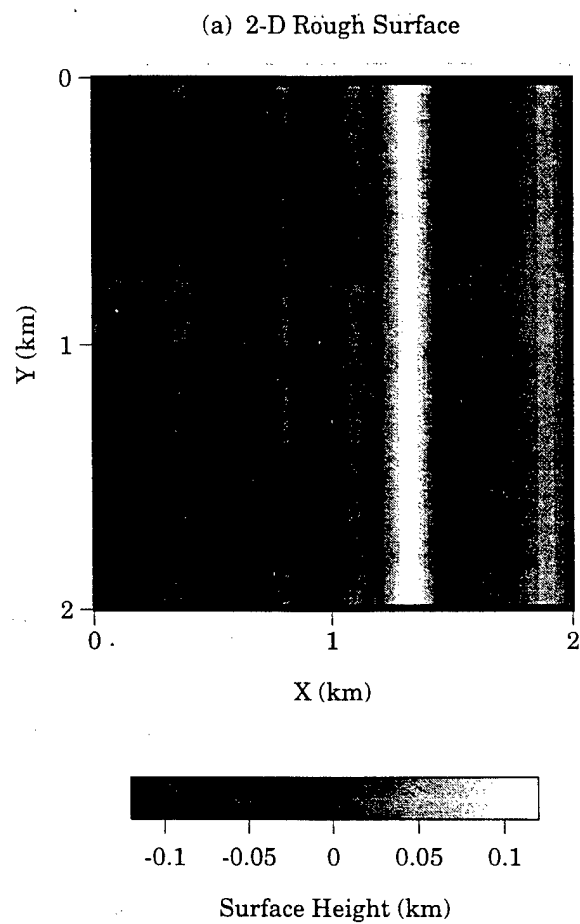
(a) 2-D Rough Surface

Figure 4: One example of a Gaussian rough surface. The correlation length is 100 m and the rms slope is 30 degrees. (a) 2-D rough interface, (b) 3-D rough interface.

(b) 3-D Rough Surface

Figure 4: continued

(a) Flat Interface

TIME (s)

X (km)
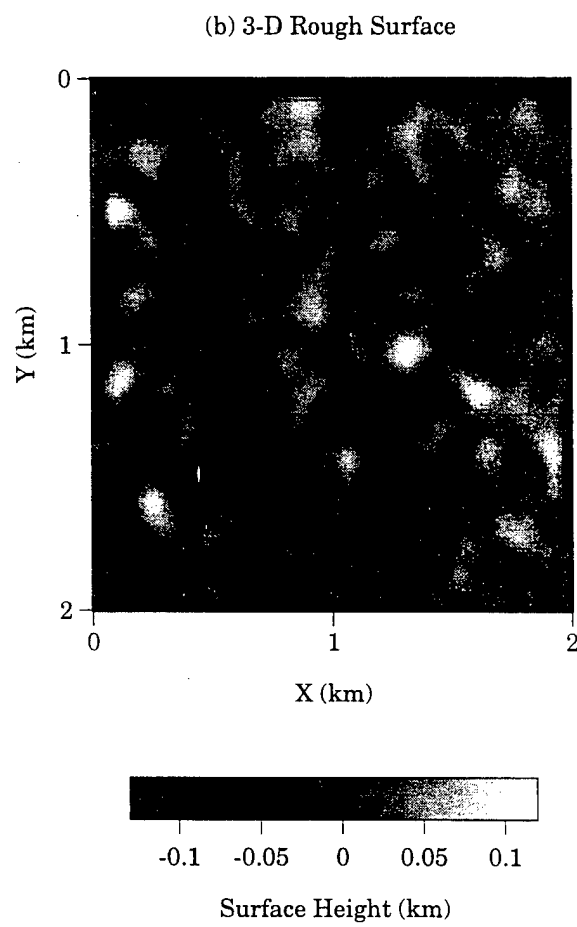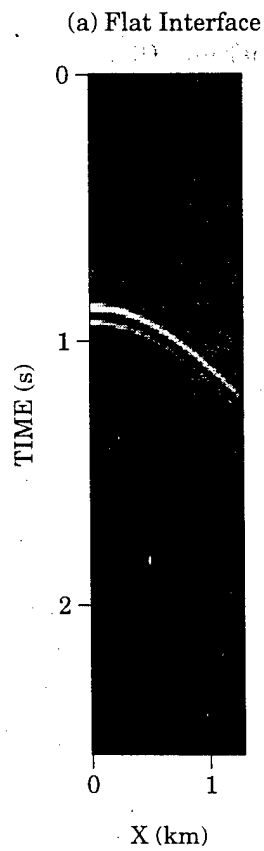
Figure 5: Synthetic seismograms of fluid-solid interface reflections. They are 2-D slices of the 3-D data set. The direct arrivals are removed from the data set. (a) flat interface, (b) 2-D rough interface, (c) 3-D rough interface.

(b) 2D Interface

Figure 5: continued

(c) 3D Interface

TIME (s)

X (km)

Figure 5: continued

(a) Direct Wave
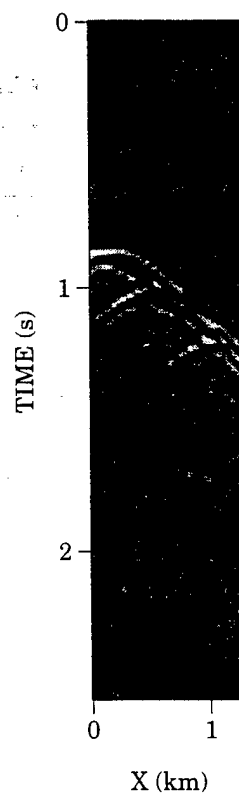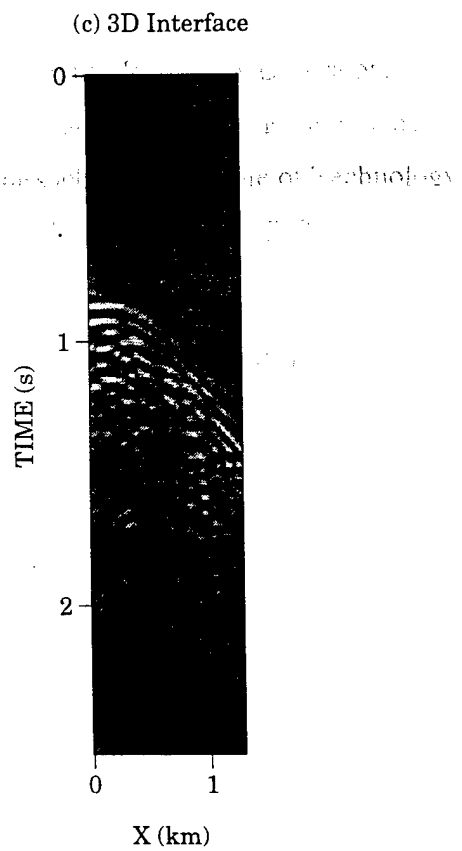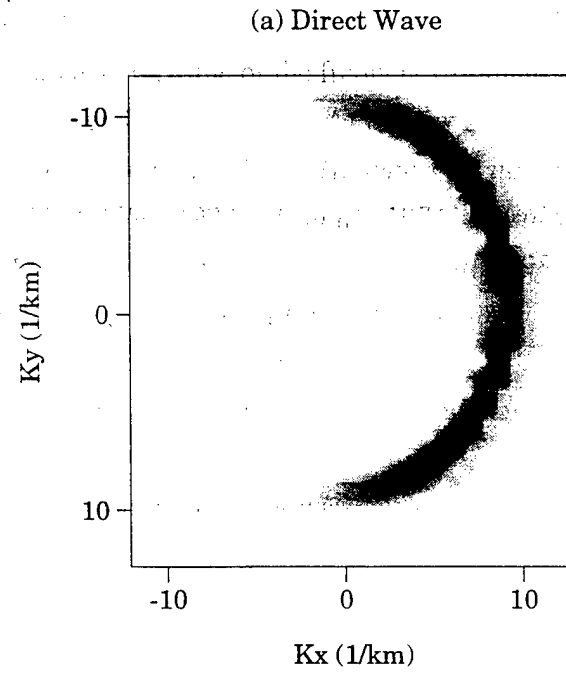
Figure 6: FK plots of synthetic data at frequency 15 Hz. (a) direct arrivals, (b) flat interface reflection, (c) 2-D rough interface reflection, (d) 3-D rough interface reflection.

110
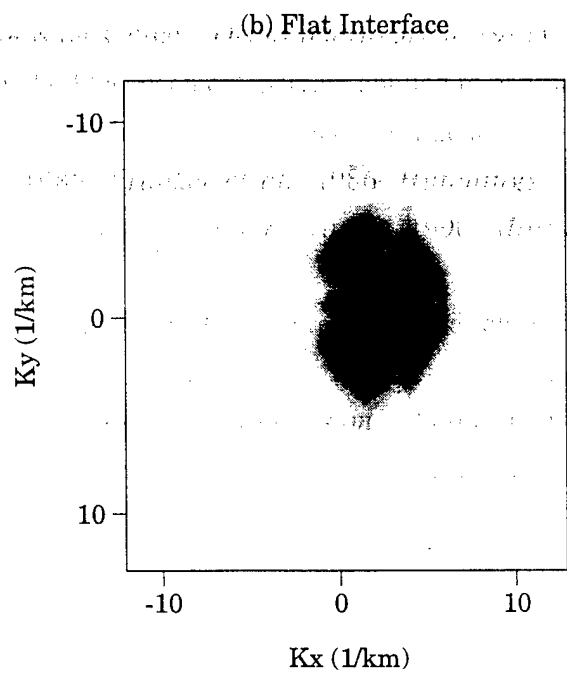
(b) Flat Interface

Figure 6: continued

(c) 2D Interface

Figure 6: continued

(d) 3D Interface

Figure 6: continued

Figure 7: Plot illustrating the rms amplitudes of the waves reflected from the flat, 2-D and 3-D interfaces. Amplitude scale is arbitrary. (a) first cycle of the primary reflection, (b) first 2 cycles of the primary reflection.

Source time functions of nuclear explosions and earthquakes in Central Asia determined using empirical Green's functions

Yingping Li, M. Nafi Toksöz, and William Rodi

Earth Resources Laboratory

Department of Earth, Atmospheric, and Planetary Sciences

Massachusetts Institute of Technology

Cambridge, MA 02139, USA

ABSTRACT

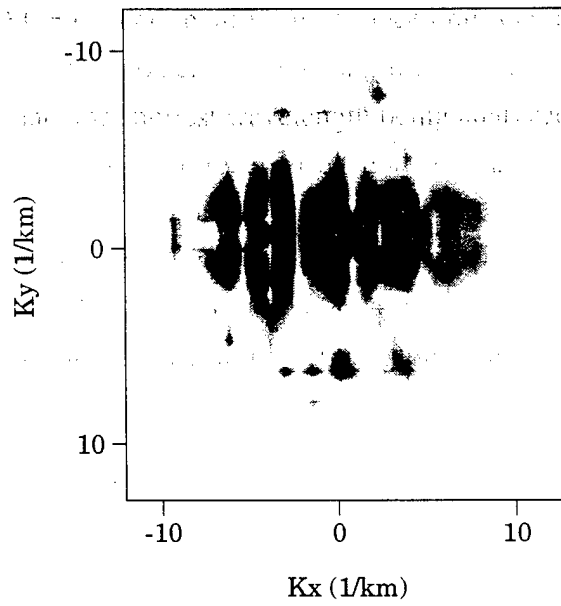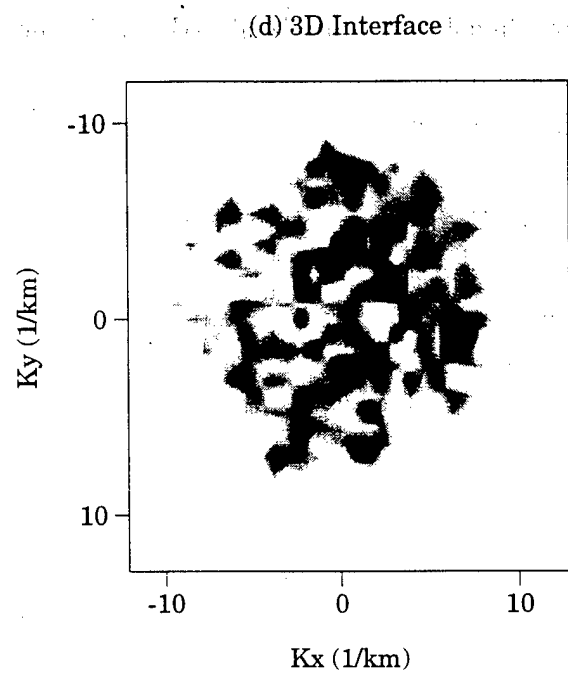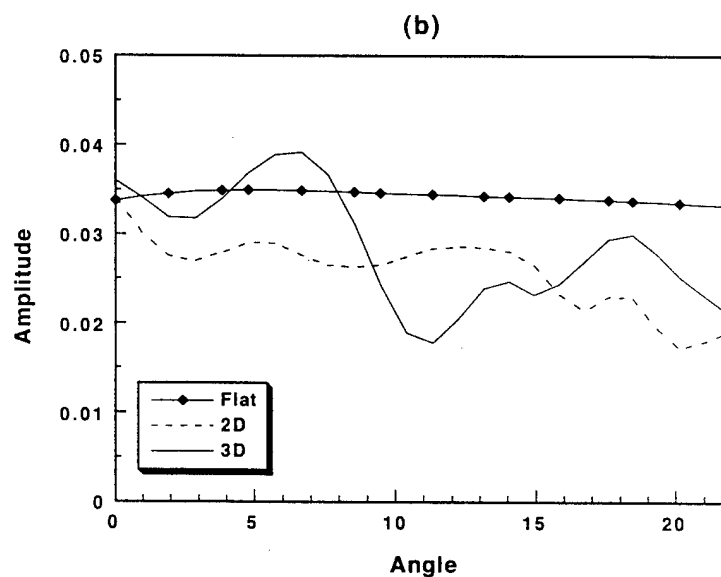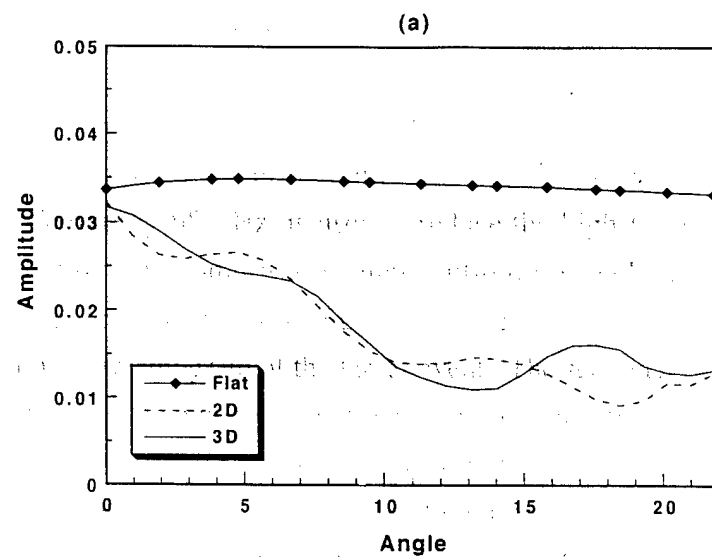Relative source time functions (RSTF) have been estimated for four underground nuclear explosions and seven earthquakes in Central Asia using broadband P waveforms of nearby smaller events as empirical Green's functions (EGF). RSTFs of the four explosions ($m_b = 5.3$ to 6.5) are each dominated by a simple pulse with a source duration of 0.4 to 0.8 s. RSTFs for two of the explosions show a significant secondary pulse with a pulse width similar to that of the first pulse. We conclude that the secondary phases are most likely associated with the spall slapdown phenomenon. Seismic moment releases by the spall phases are less than one third of those by the first explosion pulses. Elastic radii of the explosions are estimated to be about 0.25 to 0.5 km, and stress drops of the explosions range from 13 to 52 MPa. In contrast, RSTFs of earthquakes studied ($m_b = 5.5$ to 6.6) typically comprise multiple source pulses with a total source duration from a few to several tens of seconds, indicating that the complex source process involves a fault dimension of several tens of kilometers. Stress drops of the earthquakes are much smaller than those of the nuclear explosions, ranging from 0.5 to 3.5 MPa. Our study demonstrates the power of the EGF method for retrieving RSTFs and reveals that differences in RSTFs and source parameters can be used to distinguish large nuclear explosions from moderate to large earthquakes ($m_b \geq 5.5$).

INTRODUCTION

The seismic source time function (STF) of an underground nuclear explosion contains important parameters that characterize the complex physical processes that occur during the explosion [e.g., *Masse*, 1981; *Denny and Johnson*, 1991]. During the last three decades, seismologists have developed different methods to characterize the STFs and other source parameters of nuclear explosions in the time or the frequency domain and to compare them with those of natural earthquakes [e.g., *Brune and Pomeroy*, 1963; *Toksöz et al.*, 1964, 1965; *Haskell*, 1967; *Mueller and Murphy*, 1971; *Helmberger and Harkrider*, 1972; *von Seggern and Blandford*, 1972; *Müller*, 1973; *Aki et al.*, 1974; *Murphy*, 1977; *Burdick and Helmberger*, 1979; *Helmberger and Hadley*, 1981; *Lay et al.*, 1984a; *Der et al.*, 1987; *Denny and Goodman*, 1990; *Douglas*, 1991; *Patton*, 1991; *Stump and Reinke*, 1991].

Inference of the STF of a nuclear explosion from observed seismograms requires isolating the source effects from the effects of wave propagation through the Earth, recording site response, and instrument response. *Burdick and Helmberger* [1979] determined effective STFs for several megaton-class nuclear explosions by deconvolving the theoretical instrument response and Q operator. *Der et al.* [1987] developed a multiple-channel iterative deconvolution procedure to obtain effective STFs by removing a receiver structure response and the instrument response. *Stump and Reinke* [1991] used theoretical Green's functions to account for propagation effects and carried out a moment tensor inversion to determine the STF for explosion COALORA (< 20 kt). The success of these methods depends largely upon detailed knowledge of the Earth's structure and attenuation effects. As an alternative, we shall remove the responses of the Earth's structure and the seismic instrument from observed seismograms and estimate the STFs for several explosions in Central Asia by using the empirical Green's function (EGF) method. The great advantage of this approach is that detailed knowledge about the Earth's structure and attenuation is not required.

The essential idea behind the EGF approach is as follows. For two seismic events having a similar hypocenter and focal mechanism but different sizes (e.g., two nuclear explosions at the same test site, or an earthquake and its foreshock or aftershock), one can treat the waveform of the smaller event as EGF [*Hartzell*, 1978] and deconvolve it from that of the larger event to obtain a relative STF [*Mueller*, 1985]. Since the pair of events shares the same propagation path and is recorded at the same station, the deconvolution

procedure should result in a relative STF that is corrected for all path, site, and instrument effects. The retrieved STF represents the far-field displacement pulse, which is proportional to the time derivative of seismic moment [*Aki and Richards*, 1980]. Therefore the STF we use here is the reduced velocity potential (RVP) rather than the reduced displacement potential (RDP), which is commonly called the seismic source function in the literature of explosion sources [*Denny and Johnson*, 1991].

The EGF method has been extensively applied to estimate STFs and to retrieve source parameters for microearthquakes and large earthquakes, using local seismic network data [e.g., *Mueller*, 1985; *Frankel et al.*, 1986; *Hutchings*, 1987; *Li and Thurber*, 1988; *Hutchings and Wu*, 1990; *Mori and Frankel*, 1990; *Mori and Hartzell*, 1990; *Xie et al.*, 1991; *Hough et al.*, 1991; *Mori*, 1993], strong motion data [e.g., *Hartzell*, 1978; *Chen et al.*, 1991; *Kanamori et al.*, 1992], and regional and teleseismic waveforms [e.g., *Weidner and Aki*, 1973; *Patton*, 1980; *Hartzell*, 1989; *Ammon et al.*, 1993; *Li and Toksöz*, 1993; *Velasco et al.*, 1994]. *Burger and Langston* [1985] also applied the EGF method to study the source mechanism of the May 18, 1980, Mount St. Helens eruption from regional surface waves. However, few endeavors had been made to extract the STFs of nuclear explosions with the EGF deconvolution method until recently [*Li et al.*, 1993; *Toksöz et al.*, 1993; *Jiao and Wallace*, 1993]. In this paper, we shall retrieve the relative STFs of four nuclear explosions and seven earthquakes in Central Asia (Figure 1) using the teleseismic and regional broadband *P* waveforms of the smaller events with similar locations as the EGFs and compare the RSTFs of explosions with those of natural earthquakes to examine the potential value of this method in nuclear monitoring and discrimination.

DATA AND METHODS

The locations of nuclear explosion pairs in the Kazakhstan Test Site (KST) at Balapan, Kazakhstan, and in the Xinjiang Test Site (XTS) at Lop Nor, Xinjiang, China, and seven earthquake pairs in Central Asia, as well as locations of some of the seismic stations used in this study are shown in Figure 1. Tables 1 and 2 present hypocentral parameters and magnitudes from the U.S. Geological Survey (USGS) Preliminary Determination of Epicenters (PDE) for the explosions and earthquakes. The depths of burial (DOB) for explosions in Table 1 were estimated with the formula of *Jih and Wagner* [1991], $\log(DOB) = 0.31 m_b + 0.835$. The vertical component, very broadband (VBB) waveforms

used in this research were collected by the Incorporated Research Institutions for Seismology, Global Seismographic Network (IRIS GSN), Joint Seismic Program (JSP) and Chinese Digital Seismographic Network (CDSN) and were obtained through the IRIS Data Management Center (DMC). The IRIS instrument system amplitude response is typically flat to velocity from 360 s to 10 Hz and the sampling rate is 20 samples per second for the VBB channel.

Application of the EGF method requires the hypocentral separation between the larger event and the EGF event to be much smaller than the distance to a given receiver and comparable to, or less than, the shortest wavelength being analyzed, so that the two events share the same wave path to a given receiver except for small differences in the source region [e.g., *Patton*, 1980]. Based on the PDE locations for two pairs of explosions at KTS (Figure 2a), the separation between the 881112 (read as November 12, 1988: year, month, day) explosion (m_b = 5.3) and the 880614 explosion (EGF event, m_b = 5.0) is about 4 km; while the distance between the 880914 Joint Verification Experiment (JVE) explosion (m_b = 6.1) and the 890708 explosion (EGF event, m_b = 5.6) is about 7 km. However, SPOT satellite image analysis [*Thurber et al.*, 1993] indicates that the separations between these event pairs are approximately 1.5 and 3.5 km, respectively (Figure 2b). PDE locations for three explosions at XTS are shown in Figure 2c. The distance between the 920521 explosion (m_b = 6.5) and the 900816 explosion (EGF event, m_b = 6.2) is less than 5 km, and the separation between the m_b = 6.5 event and the 931005 explosion (EGF event, m_b = 5.9) is estimated to be 12 km. Unfortunately, no satellite image analysis is available for these events. To estimate the location separation independently, we fixed the explosion depths at the surface and used differences between R-P times (lags between P and Rayleigh waves) among the events from a few stations to derive the locations relative to the largest explosion. The cross-correlation technique [e.g., *Pechmann and Kanamori*, 1982; *Poupinet et al.*, 1984] is applied to P and Rayleigh wave windows for obtaining precise readings of relative arrival times of the waves from the VBB seismograms. Reading error is typically less than ±0.05 s, resulting in a location error less than 0.5 km. The relocations (Figure 2d) indicate that the distance between the 920521 and 900816 explosions is about 2 km, and the distance between the 920521 and 931005 explosions is about 7 km.

Assuming two nearby surface sources with epicenter separation ΔL in the N-S direction, the difference between two ray path lengths (ΔD) for the two events can be

118

simply written as $\Delta D \cong \Delta L(\sin\phi\cos\theta)$, where ϕ is the takeoff angle and q is the source-to-receiver azimuth. For an event pair recorded at a distance of 35° and $\theta = 0°$, the epicentral separation of 7 km will correspond to the maximum difference between two path lengths of about 2.8 km. Given an average P wave velocity in KTS and XTS of 6.5 km/s [*Quin and Thurber*, 1992; *Mangino and Ebel*, 1992] and the dominant frequencies of the explosion STFs ranging from 0.3 to 3 Hz, the shortest wavelength we resolve will be about 2.3 km, which is comparable to ΔD. For teleseismic and regional data used here, we find that events with source separations up to 7 km are still similar to each other and can be used as EGF events.

To illustrate the EGF deconvolution method, Figure 3 shows vertical component broadband P waveforms of two XTS explosions (920521 and 900816) recorded at station OBN, about 4000 km from the test site. We note that the first wavelets of the two explosions are very similar, reflecting intercorrelation [*Lay et al.*, 1984b] between the nearby explosions. The observed seismogram $U_l(t)$ of the larger explosion can be expressed as the convolution of its STF, $S_l(t)$, the impulse response of path $P(t)$, the receiver structure $R(t)$, and the instrument response $I(t)$:

$$U_l(t) = S_l(t) * P(t) * R(t) * I(t), \qquad (1)$$

where asterisk represents convolution. For an EGF event with its STF, $S_g(t)$, its seismogram $U_g(t)$ can be written as

$$U_g(t) = S_g(t) * P(t) * R(t) * I(t). \qquad (2)$$

The broadband P waveform of the smaller event is used as the EGF and deconvolved from that of the larger explosion to obtain a relative STF for the larger event. The deconvolution in the frequency domain is a spectral division:

$$\frac{U_l(\omega)}{U_g(\omega)} = \frac{S_l(\omega)}{S_g(\omega)} = S_r(\omega) \qquad (3)$$

where ω is the angular frequency and $S_r(\omega)$ is the spectrum of the RSTF of the larger event. The deconvolution procedure used here is similar to that of *Li and Thurber* [1988]

and *Li and Toksöz* [1993]. The *P* waveforms of both events are windowed to 20 s, zero padded to 8192 points, and then Fourier transformed. The spectrum of the large explosion is divided by that of the EGF event and then inverse transformed to obtain the RSTF, $S_r(t)$. To stabilize the deconvolution, we used a Gaussian filter to slightly smooth the spectra before the spectral division. After deconvolution, a fourth-order Butterworth low-pass filter, with a corner frequency of 3 Hz, is used to reduce the high-frequency noise. The RSTF of the 920521 explosion comprises a simple pulse followed by a secondary phase, with a total source duration of about 1.6 s (Figure 3b). We look back at Figure 3a and find a secondary arrival on the seismogram of the larger event. The secondary phase is possibly caused by spall slapdown or tectonic release. We will discuss this matter in detail later.

The deconvolved pulse is the RSTF, and its pulse width presents the relative source duration of the larger event compared to that of the EGF event [*Frankel et al.*, 1986]. The true STF of the larger event, $S_l(t)$, will be the convolution of the source pulse of the EGF event with the RSTF of the larger event

$$S_l(t) = S_r(t) * S_g(t). \tag{4}$$

$S_l(t) = S_r(t)$ only when $S_g(t) = d(t)$. If the source duration of the EGF event is short enough to approximate a delta function, then the RSTF can be approximately equal to the true STF. However, if the source duration of the EGF event is nonnegligible, larger error will be introduced for estimating the source duration from the RSTF, especially for the events which have relatively narrow deconvolved pulse width compared to the STF pulse width of the EGF event. We can obtain the true STF of the larger event from equation (4) if the STF of EGF event is known.

RELATIVE SOURCE TIME FUNCTIONS FOR EXPLOSIONS

With broadband *P* waveforms recorded at station WMQ ($\Delta = 9°$), we estimated the RSTF of the 881112 explosion ($m_b = 5.3$) in KTS using the 880614 explosion ($m_b = 5.0$) as the EGF event (Figure 4a). The RSTF of the 881112 explosion is a simple pulse with a source duration of 0.4 s, suggesting a rapid energy release of the nuclear explosion. We attributed the success of retrieving the RSTF to the selection of an appropriate EGF: the spatial separation between the two explosions is less than 1.5 km and the depth difference

is estimated at 0.06 km (Table 1 and Figure 2). Since only one regional-distance station was used to retrieve the RSTF, the background noise level in Figure 4a is relatively high. No obvious secondary phase can be resolved from the single-station estimate of the RSTF.

Broadband P waveforms from stations WMQ, LZH, HIA, and COL were used to extract the RSTF of the 880914 JVE explosion ($m_b = 6.1$) using the 890708 explosion ($m_b = 5.6$) as the EGF event. The results are shown in Figure 4b. The stacked estimate of the RSTF (bottom trace in Figure 4b) shows a major pulse with a total duration of about 1.2 s. The asymmetric pulse shape of the RSTF and its positive-polarity shoulder suggests that a secondary pulse with a much smaller amplitude and a similar pulse width follows the first explosion pulse.

The RSTF of 900816 explosion ($m_b = 6.2$) at XTS was extracted using the 931005 explosion ($m_b = 5.9$) as EGF event. We used broadband P waveforms recorded at stations OBN, KEV, and COL with epicentral distances ranging from 36° to 65°. The single-station estimates and the stacked STF (bottom trace) are presented in Figure 5a. The major feature of the STF is a simple pulse with a duration of 0.55 s. No significant secondary phase can be clearly identified on the stacked trace. However, we do observe the variation of the STFs among the single-station estimates, especially for the latter part of the STFs. This observation can be interpreted as either the tectonic release effect or the imperfection of the EGF caused by a relatively larger epicentral separation between the two events.

We retrieve the RSTF of the 920521 explosion ($m_b = 6.5$) at XTS with the broadband P waveforms of two nearby explosions (931005, $m_b = 5.9$ and 900816, $m_b = 6.2$) as the EGFs. This data set provides an opportunity not only to extract the RSTF with more than one EGF event but also to examine the conditions under which the EGF method can be successfully applied. The RSTF extracted using the 931005 explosion ($m_b = 5.9$) as the EGF event is shown in Figure 5b, while the RSTF retrieved using the 900816 explosion ($m_b = 6.2$) as the EGF event is presented in Figure 5c. The RSTFs of the 920521 explosion are dominated by a simple pulse with a duration about 0.8 s, followed by a significant secondary pulse with a smaller amplitude and a similar pulse width. The total source duration of the explosion is about 1.6 s. The area under the RSTF is proportional to the seismic moment release [*Aki and Richards*, 1980], and the seismic moment release of the $m_b = 6.5$ explosion is larger than those of two EGF event (931005 and 900816) by factors of 5.5 and 2.5, respectively. This result agrees with the fact that the seismic moment release ratio between the 900816 and 931005 explosion is about 2.2, which is

estimated using the area under the RSTF in Figure 5a, indicating that the EGF method can provide a reliable means to estimate the relative seismic moment release.

In spite of having used two events with different sizes (m_b = 5.9 and 6.2) and different hypocenters (depth = 0.46 and 0.57 km, ΔL = 7 and 2 km) as EGF events, the waveforms of the two stacked RSTFs for the 920521 explosion are almost identical except for the pulse amplitudes (Figures 5b and 5c), indicating that the EGF method can effectively correct the wave propagation effects through the Earth as well as the instrument effect, as long as one or more suitable EGF events are available. The successful extraction of the RSTF using the two EGF events, with spatial separations of about 2 and 7 km to the largest explosion (m_b = 6.5), also supports our earlier argument about the criteria of selecting suitable EGF events for applying the EGF method to the teleseismic and far-regional P waveform data.

With the m_b = 5.9 explosion as the EGF event, inferred RSTF pulse widths are 0.55 s and 1.6 s for the m_b = 6.2 and m_b = 6.5 explosions, respectively (Figures 5a and 5b). Thus, for explosions with a size difference of 0.3 magnitude units, the RSTF pulse width of the smaller event is narrower than that of the larger event by a factor of 3. If this is a linear relation and valid for the events with smaller magnitude, the RSTF pulse width for the m_b = 5.9 explosion is expected to be about 0.2 s. A scaling relation for the earthquakes in continental interiors [*Somerville et al.*, 1987] indicates that the source durations are expected to be 0.4 to 1.0 s for events with seismic moments of 5×10^{15} to 5×10^{16} Nm. The source duration estimated with the scaling relation is comparable to our extrapolation result, although the scaling relation for earthquake may not be entirely appropriate for the explosions. We have used two EGF events (m_b = 5.9 and 6.2) to retrieve the RSTF of the m_b = 6.5 explosion. The waveform shapes of the two RSTFs in Figures 5b and 5c are very similar, and the pulse width difference between the two RSTFs is hardly observed. This result implies that the STF pulses of two EGF events (m_b = 5.9 to 6.2) may have relatively short source duration comparing to the STF of the largest explosion and that the source pulse of an EGF event with a duration of 0.55 s may still be approximately treated as a delta function in this case.

To examine the effects of source pulses of EGF events on the true STF of the largest explosion, we convolve five assumed triangular source pulses of the EGF event, $S_g(t)$, with the RSTF, $S_r(t)$, in Figure 5c to predict the true STF, $S_l(t)$, for the largest explosion (Figure 6a). The source duration of $S_g(t)$ is from 0.2 to 1.0 s with an increment of 0.2 s

and the peak amplitudes of the triangular pulses are 10, 5, 0.33, 2.5, and 0.5, so that the areas under the STFs are one unit. The convolved STFs show a little variation of the pulse width of the predicted STFs (Figure 6a). For a source pulse of an EGF event with a duration of up to 0.8 s, the pulse width of the predicted STF is broadened only by about 0.1 s. This result indicates that the RSTF pulse width of the larger event is relatively insensitive to the pulse width variation of the EGF events. Therefore the RSTF of the larger event can be approximately treated as the STF with a tolerable error. Figure 6b plots the source spectra for the RSTF, $S_r(\omega)$, and the five predicted STFs. The corner frequencies, f_c, of the five predicted STFs range from 1.2 to 2 Hz for the $m_b = 6.5$ explosion.

SOURCE PARAMETERS OF EXPLOSIONS

Figure 7 summarizes the RSTFs for the four explosions in Central Asia. With the estimated STFs and magnitudes of the explosions, one can derive other explosion source parameters, such as the reduced displacement potential (ψ_∞), the seismic moment (M_0), the elastic radius (R_e), and the stress drop (Δs). The seismic moment of an explosion is given by [*Müller*, 1973]

$$M_0 = 4\pi\rho\alpha^2\psi_\infty, \tag{5}$$

where r and a are the density and the P wave velocity at the source, respectively. *Ringdal et al.* [1992] present an empirical relationship between ψ_∞ and m_b for explosions in KTS,

$$\log\psi_\infty = 1.1m_b - 2.57. \tag{6}$$

Assuming that the relation is also valid for XTS and assuming $\rho = 2700$ kg/m^3 and $\alpha = 5.2$ km/s [*Quin and Thurber*, 1992; *Matzko*, 1992], we can calculate reduced displacement potentials and seismic moments for all explosions ($m_b = 5.0$ to 6.5) used in this study (Table 3). Since the area under the RSTF is the seismic moment ratio (M_0/M_{0g}) between the larger explosion and the EGF event, we can also calculate the seismic moment of the larger explosion by multiplying the area with the seismic moment of EGF event, M_{0g}. In this manner, we estimated the seismic moment not only for the explosion source pulses but also for the secondary phases. The seismic moments of the larger explosions derived with the two methods agree with each other quite well (Table 3).

The elastic radius R_e is estimated with the relationship derived by [*Murphy*, 1977]

$$R_e = \alpha/2\pi f_c, \tag{7}$$

where f_c is the corner frequency of the STF pulse and the P wave velocity at the source is assumed to be 5.2 km/s. Assuming the source pulse width of the EGF event is less than a half of pulse width of the RSTF, we can estimate the corner frequency, f_c, and its error bar from the RSTF and corrected STFs with the method showing in Figure 6b. The stress drops for the explosions are calculated from *Aki et al.*'s [1969] formula for a spherical explosion source

$$\Delta\sigma = 23M_o/60\pi R_e^3. \tag{8}$$

The estimated source parameters and their error bars are summarized in Table 3. The seismic moments range from 1.7×10^{15} to 3.3×10^{16} Nm, and elastic radii range from 250 to 520 m for the four explosions with $m_b = 5.3$ to 6.5. The mean values of stress drops are estimated about 13 MPa for one event with $m_b = 5.3$ and about 27 to 52 MPa for larger explosions ($m_b > 6.0$). The lower and upper bounds of the stress drop estimates are 5 and 191 MPa. *Aki et al.* [1969] estimated the source parameters for the 681219 explosion BENHAM ($m_b = 6.3$) in NTS and found a seismic moment of 2.5×10^{17} Nm and elastic radius of 450 to 900 m, resulting in an estimate of the stress drop of 40 to 300 MPa. Our estimates of the elastic radii and stress drops for explosions at KTS and XTS are comparable to those estimated for the BENHAM explosion.

Spall Slapdown Phases

A significant feature of the RSTF for the 920521 explosion is that it comprises two distinct pulses with a total source duration of 1.6 s. This result is consistent with the result for the same explosion extracted by Lay and his colleague (*T. Lay*, personal communication, 1993) using the surface wave and EGF method. The cause of this secondary pulse is an interesting problem. Previous studies of explosion sources have revealed that besides the explosion process itself, two other physical processes contribute to the nonisotropic components of an explosion STF: spall [e.g., *Eisler et al.*, 1966; *Frasier*, 1972; *Viecelli*, 1973; *Day et al.*, 1983; *Stump*, 1985; *Schlittenhardt*, 1991] and tectonic release [e.g., *Toksöz and Kehrer*, 1972; *Wallace*, 1991; *Patton*, 1991]. A pP

reflection [e.g., *Lay*, 1991] may also affect the RSTF, since significant depth difference between an explosion and its EGF event may cause a secondary pulse in the RSTF. We will try to interpret the secondary pulse from all possible aspects.

Assuming that the DOB-m_b relation [*Jih and Wagner*, 1991] is also valid for explosions at XTS, then the depth differences between the $m_b = 6.5$ explosion (920521) and the two EGF events (931005 and 900816) estimated using m_b (Table 1) are only 0.25 and 0.14 km, respectively. If the secondary phase is caused by the depth phase pP, for an average P wave velocity of 5.2 km/s for the shallow crust at XTS [*Matzko*, 1992], the time delay of 0.75 s between the two pulse peaks will correspond to a depth difference of about 1.95 km, which is larger than the ones estimated from m_b by a factor of 8 to 14. The delay time of 0.75 s is too large to associate with the effect of the depth phase. Thus the secondary pulse was probably caused by spall or tectonic strain release, rather than by the pP reflection. For the same reason, we believe that the secondary pulse of the JVE explosion (Figure 4b) is not the effect of the pP reflection either.

The tectonic release caused by an explosion typically generates a non-isotropic seismic radiation pattern like a double-couple earthquake [e.g., *Toksöz and Kehrer*, 1972; *Wallace et al.*, 1985]. If the RSTF of the explosion (920521, $m_b = 6.5$) does indeed include the component of tectonic release, it is expected that a radiation pattern similar to an earthquake will be observed. We looked at the single station estimates of RSTFs at different azimuths in Figure 5c and found only slight differences among the RSTFs. The positive polarities of the secondary pulses at all stations (Figure 5c) led us to conclude that the secondary pulse is dominated by the contribution from the spall slapdown phase, which is thought to be associated with a vertical dipole [e.g., *Stump and Reinke*, 1991]. Since the tectonic release component of an explosion can be best observed from the S wave and/or surface wave data [*Wallace*, 1991], we suggest that a further study with S wave and surface waves of the same explosions will lead to a better understanding of the tectonic release components of the explosions.

The seismic moment release of the secondary pulse from the 880914 KST and the 920521 XTS explosions is about 10% to 30% of that for the first explosion pulse (Table 3). It is interesting to compare the features of the spall slapdown phases we observed for the explosions at XTS and KTS with those of the spall slapdown phases generated by other explosions at different test sites. Table 4 summarizes the parameters for spall slapdown phases of explosions at different test sites estimated with different methods by many

investigators. For explosions (m_b = 3.8 to 6.3) in Nevada Test Site (NTS), the delay times between the spall slapdown phases and the P arrivals (P_{ss}-P) range from 0.17 to 1.7 s, and the pulse widths of the spall phases vary from 0.3 to 1.0 s. For the large explosions LONGSHOT, MILROW, and CANNIKIN (m_b = 6 to 7) in Amchitka Test Site (ATS), P_{ss}-P ranges from 0.7 to 2 s, with a mean of 1.35 s, and the spall pulse widths range from 0.5 to 1 s. These numbers are comparable to what we have observed for the spall slapdown phase generated by the 920521 explosion and the 880914 explosion.

RELATIVE SOURCE TIME FUNCTIONS FOR EARTHQUAKES

The RSTF of the 931002 earthquake (m_b = 6.2) in southern Xinjiang was estimated using the teleseismic and regional broadband P waveforms of a nearby aftershock (m_b = 5.7) as the EGFs (Figure 8a). Eight single-station estimates of the RSTF are stacked to obtain an average RSTF. The mainshock consists of two subevents: a smaller precursor event followed by a larger one 2 s later. The total relative source duration of the mainshock is about 9 s. The location of the earthquake pair is about 300 km south of XTS.

We retrieved relative RSTFs for a deep earthquake (930809, m_b = 6.3) in the Hindu Kush region using the teleseismic broadband P waveforms of its foreshock (m_b = 5.8) as the EGFs (Figure 8b). Two pulses can be clearly observed on the single and the stacked RSTF traces. It is evident that the mainshock was a double event with a total relative source duration of about 14 s. Both mainshocks (931002 and 930809) show a relative complex source process and a longer relative source duration compared with the explosions.

We also apply the EGF method to the other five pairs of earthquakes in Central Asia (Figure 1 and Table 2). Figure 9 summarizes the stacked relative STFs estimated for all seven mainshocks. Stations used in retrieving RSTFs for each event are listed in Table 5. The body wave magnitudes (m_b) for the mainshocks range from 5.5 to 6.6, while the surface wave magnitudes (M_s) are from 5.2 to 7.4. The relative source duration of the earthquakes is from 7 to 29 s. It can be seen clearly from the RSTF in Figure 9 that almost all of the earthquakes consist of multiple events, indicating the complicated source processes of the earthquakes in Central Asia. The simplest RSTF among the seven earthquakes is 900614 Kazakhstan m_b = 6.1 earthquake. Its RSTF contains one major and one minor pulse with a total duration of about 7 s. The most complicated RSTF is for the April 26, 1990, Qinghai, China, mainshock sequence. The PDE reported that the sequence

126

included three subevents with m_b = 5.7, 6.5, and 6.2. The three major pulses corresponding to the three events can be clearly identified from the RSTF of the mainshock.

The fault radius (r) and the static stress drop ($\Delta\sigma$) can estimated using the following relationships [*Boatwright*, 1980; *Brune*, 1970]:

$$r = \frac{\tau_{1/2} v_r}{1 - (v_r \sin\theta / \alpha)}, \tag{9}$$

$$\Delta\sigma = 7 M_o / 16 r^3. \tag{10}$$

where $\tau_{1/2}$ is the rise time and q is the takeoff angle; v_r and a represent rupture velocity and P wave velocity, respectively. We use a = 6.5 and 8.2 km/s and v_r = 2.0 and 2.5 km/s for the earthquakes in the crust and the upper mantle, respectively, and assume an average q of 30°. For the larger event in each pair, the seismic moment ratio M_o / M_{og} is estimated based on a measurement of the area under the RSTF pulse. Using the CMT (HRV) solutions of seismic moments for the EGF events (M_{og}) as reference, we can derive the seismic moment M_o for the larger events. The seismic moments M_o estimated in this way are very close to the quick CMT solutions [e.g., *Ekström et al.*, 1986] for the larger events (see Table 6).

As we mentioned earlier, the traces in Figure 9 are the RSTFs rather than the STFs. The RSTF approximately equals the STF of the larger event only when the source pulse of the EGF event is short enough to approximate a delta function. For the EGF events with magnitudes less than 5.3, the RSTFs could be approximately treated as the STFs with tolerable errors since the source pulse widths for these events are typically 1 to 2 s. However, if we use a relatively large earthquake (e.g., m_b > 5.7) as the EGF event to retrieve the STF, the source pulse width of the EGF event itself must be accounted for. Otherwise, significant errors will be introduced into estimates of source parameters. We use the 900614 Kazakh earthquake and the 930809 Hindu Kush event to illustrate the effect of source pulse width of EGF event on the RSTF of the larger event.

According to the quick CMT (HRV) solution, the source durations for the 900614 Kazakh mainshock and its EGF counterpart (900803) are 17 and 9 s, respectively. Our inferred source duration of the RSTF of the Kazakh mainshock is only 7 s, about 2.5 times

127

shorter than the CMT estimate. We assume that the source of the EGF event is a triangular pulse with duration of 9 ± 1 s and convolve them with the RSTF to recover an "absolute" STF (Figure 10a). The peak amplitudes of these triangle pulses are 0.25, 0.22, and 0.2 so that the areas under the pulses are one unit. The duration of the corrected STF is measured about 18 ± 0.5 s, close to the CMT estimate for the larger event. Figure 10b shows how the rise time $\tau_{1/2}$ and its error bars are measured from the corrected STFs of the 900614 Kazakh event. The source durations of the 930809 Hindu Kush mainshock and its foreshock are 16 and 7 s, respectively, based on the CMT (HRV) solutions. The triangle source pulses with duration of 7 ± 1 s was convolved with the RSTF of the 930809 mainshock to retrieve the STF of the mainshock (Figure 10c). The source duration of the corrected STF is about 16.5 ± 1 s, which is about 2 to 3 s wider than that of the RSTF. The rise time and measurement error for the first subevent of the 930809 mainshock are shown in Figure 10d. Using the same approach, we measure the rise times for the 931002 and 920819 mainshocks from the corrected STFs. For the 900515, 900417, and 900426 mainshocks, their EGF events are relatively small, from magnitude 4.7 to 5.3. We convolve a triangle source pulse of duration 1.5 ± 1 s with the RSTFs of three mainshocks and find that the corrected STFs differ only a little from their respective RSTFs. The rise times and error bars estimated from the "corrected" STFs for 12 subevents of the seven mainshocks are listed in Table 6.

Source parameters for the 12 subevents are summarized in Table 6. These earthquakes have seismic moments ranging from 9.6×10^{16} to 7.7×10^{19} Nm, and their fault radii are estimated at about 4 to 21 km. Estimated stress drop values fall from 0.4 to 2.3 MPa. The average stress drop for 12 subevents of the seven mainshocks is 1.4 ± 0.5 MPa. It should be noted that the stress drop estimates are made under the assumption of a rupture velocity of 2 to 2.5 km/s. If the rupture velocity is assumed to be 3.0 to 3.6 km/s, the average stress drop will decrease to 0.5 ± 0.2 MPa. However, when we assume a relatively low rupture velocity of 1.5 to 2 km/s, the average stress drop will increase to 3.5 ± 1.3 MPa. Therefore we conclude that the stress drops for these intraplate earthquakes in Central Asia are typically estimated to range from 0.5 to 3.5 MPa.

For comparison, we also estimate the rise times from the RSTFs for the 12 subevents. The error bars for these relative rise time measurements are typically less than 0.1 s. The source parameters estimated with the relative rise times are also listed in Table 6. For the RSTF retrieved using relatively small events ($m_b < 5.3$) as EGF events, stress drops

estimated from the RSTFs differ from those estimated with the corrected STFs by a factor of 1.1 to 1.8, suggesting the RSTFs can be approximately treated as the STFs. However, when we use the larger earthquakes (m_b = 5.7 to 6.0) as the EGF events and size differences between the target and EGF events are less than 0.5 magnitude units, estimates of the rise time from the RSTFs will underestimate the fault radius by a factor of 1.5 to 2.5 and overestimate the stress drop by a factor of 3 to 16. Therefore, to obtain a reliable estimate of source parameters, especially stress drop, the source pulse width of the EGF event should be taken into account in the latter case.

The lower and upper bounds of the stress drop estimates for the earthquakes in Central Asia are 0.4 and 21 MPa, respectively. The wide range of variations indicates the stress drop is one of most difficult source parameters to be reliably estimated. The error sources include the uncertainties in the assumed rupture velocity, rise time measurement, and circular fault assumption. Our preferred stress drop estimates of 0.5 to 3.5 MPa are much lower than those for some moderate earthquakes, such as the 750204 m_b = 6.4 Haicheng, China, earthquake (14.4 MPa [*Chung and Brantley*, 1989]), the 831007 m_b = 5.1 Goodnow, New York, earthquake (26.5 MPa, [*Nabelek and Saurez*, 1989]), the 820109 m_b = 5.8 New Brunswick, Canada, earthquake (50.0 MPa [*Nabelek*, 1984]), but comparable to those of other moderate earthquakes, such as the 800727 m_b = 5.2 Sharpsburg, Kentucky, earthquake (0.3 to 0.6 MPa [*Herrmann et al.*, 1982]), the 650912 m_b = 5.9 South China Sea earthquake and the 671210 m_b = 6.0 Koyna, India, earthquake (1.8 and 2.0 MPa, respectively [*Chung and Brantley*, 1989]), and the 660628 m_b = 5.8 Parkfield, California, earthquake (3.3 MPa, [*Wu*, 1968]).

DISCUSSIONS AND CONCLUSIONS

Analysis of the RSTFs of four nuclear explosions (m_b = 5.3 to 6.5) and seven earthquakes (m_b = 5.5 to 6.6) in Central Asia indicates that the earthquake RSTF, in general, shows a complex source process with a duration of several tens of seconds, implying that the earthquake processes involve a fault dimension of a few to several tens of kilometers. In contrast, the explosion source presents a relatively simple RSTF with one or two pulses and a much shorter source duration of about 0.4 to 1.6 s, which corresponds to a relatively smaller elastic radius of 0.25 to 0.5 km, reflecting the rapid energy release over a small volume for the nuclear explosions. Among the four explosions, the 920521 explosions and the 880914 explosions show significantly a secondary pulse with a pulse

width similar to their first pulse. We interpret that the secondary pulses are most likely associated with the spall slapdown. The moment release of the spall slapdown phase is about one third of the explosion pulse itself.

The source durations of the explosions and earthquakes in Central Asia are plotted versus the magnitudes, m_b, in Figure 11. For events with similar magnitudes, the relative source durations for explosions are shorter than those of earthquakes by a factor of about 10, indicating the earthquakes and explosions within this magnitude range can be easily distinguished from one another by examining their relative source durations. Tables 3 and 6 clearly show that the elastic radii of the explosions are much smaller than the fault dimension of earthquakes with similar magnitudes by a factor of 10 to 40. Stress drops of the nuclear explosion sources are estimated typically at 13 to 52 MPa, compared with relatively low stress drops of 0.5 to 3.5 MPa for the natural earthquakes with similar magnitudes in the vicinity of the two test sites. Our results strongly indicate that the large explosions and earthquakes (m_b = 5.3 to 6.6) in Central Asia can be easily distinguished from each other by comparing the RSTFs and analyzing the source parameters such as source duration, source dimension, and stress drop. We conclude that the EGF method has a great potential for discriminating nuclear explosions and earthquakes, at least for events with m_b magnitudes ranging from 5.5 to 6.5, by comparing their RSTFs and source parameters.

ACKNOWLEDGMENTS

REFERENCES

Aki, K., and P. G. Richards, *Quantitative Seismology: Theory and Methods,* W. H. Freeman, New York, 1980.

Aki, K., M. Bouchon, and P. Reasenberg, Seismic source function for an underground nuclear explosion, *Bull. Seismol. Soc. Am., 64,* 131-148, 1974.

Aki, K., P. Reasenberg, T. DeFazio, and Y. Tsai, Near-field and far-field evidences for triggering of an earthquakes by the BENHAM explosion, *Bull. Seismol. Soc. Am., 59,* 2197-2208, 1969.

Ammon, C. J., A. A. Velasco, and T. Lay, Rapid estimation of rupture directivity: Application to the 1992 Landers (*Ms*=7.4) and Cape Mendocino (*Ms*=7.2) California earthquakes, *Geophys. Res. Lett., 20,* 97-100, 1993.

Bakun, W. H., and L. R. Johnson, The deconvolution of teleseismic *P* waves from explosions MILROW and CANNIKIN, *Geophys. J. R. Astron. Soc., 34,* 321-342, 1973.

Boatwright, J., A spectral theory for circular seismic sources: Simple estimates of source dimension, dynamic stress drops and radiation energy, *Bull. Seismol. Soc. Am., 70,* 1-28, 1980.

Brune, J. N., Tectonic stress and the spectra of seismic shear wave from earthquakes, *J. Geophys. Res., 75,* 4997-5009, 1970.

Brune, J. N., and P. W. Pomeroy, Surface wave radiation patterns for underground nuclear explosions and small-magnitude earthquakes, *J. Geophys. Res., 68,* 5005-5028, 1963.

Burdick, L. J., and D. V. Helmberger, Time functions appropriate for nuclear explosions, *Bull. Seismol. Soc. Am., 69,* 957-973, 1979.

Burger, R. W., and C. A. Langston, Source mechanism of the May 18, 1980, Mount St. Helens eruption from regional surface waves, *J. Geophys. Res., 90,* 7653-7664, 1985.

Chen, Y. T., J. Y. Zhou, and J. C. Ni, Inversion of near-source broadband accelerograms for the earthquake source-time function, *Tectonophysics, 197,* 89-98, 1991.

Chung, W.-Y., and B. J., Brantley, The 1984 southern Yellow sea earthquake of Eastern China: Source properties and seismotectonic implications for a stable continental area, *Bull. Seismol. Soc. Am., 79,* 1863-1882, 1989.

Day, S. M., N. Rimer, and J. T. Cherry, Surface waves from underground explosions with spall: Analysis of elastic and nonlinear source models, *Bull. Seismol. Soc. Am., 73,* 247-264, 1983.

Denny, M. D., and D. M. Goodman, A case study of the source time function: SALMON and STERLING reevaluated, *J. Geophys. Res., 95,* 19,705-19,723, 1990.

Denny, M. D., and L. R. Johnson, The explosion seismic source function: models and scaling laws reviewed, in *Explosion Source Phenomenology, Geophys. Monogr. Ser., Vol. 65,* edited by S. Taylor, H. Pattern, and P. Richards, pp. 1-24, AGU, Washington, D.C., 1991.

Der, Z. A., R. H. Shumway, and A. C. Lees, Multichannel deconvolution of *P* waves at seismic arrays, *Bull. Seismol. Soc. Am., 77,* 195- 211, 1987.

Douglas, A., Broad band estimates of the seismic source functions of Nevada explosions from far-field observations of *P* waves, in *Explosion Source Phenomenology, Geophys. Monogr. Ser., Vol. 65,* edited by S. Taylor, H. Pattern, and P. Richards, pp. 127-140, AGU, Washington, D.C., 1991.

Eisler, J. D., F. Chilton, and F. M. Sauer, Multiple subsurface spalling by underground nuclear explosions, *J. Geophys. Res., 71,* 3923-3927, 1966.

Ekström G. A., A. M. Dziewonski, and J. M. Steim, Quasi-real time CMT solutions for July 1986 California earthquakes: *Eos,Trans. AGU, 67,* 1090, 1986.

Frankel, A., J. Fletcher, F. Vernon, L. Haar, J. Berge, T. Hanks, and J. Burne, Rupture characteristics and tomographic source imaging of M_L~3 earthquakes near Anza, south California, *J. Geophys. Res., 91,* 12,633-12,650, 1986.

Frasier, C. W., Observations of *pP* in the short-period phases of NTS explosions recorded at Norway, *Geophys. J. R. Astron. Soc., 31,* 99-110, 1972.

Hartzell, S., Earthquake aftershocks as Green's functions, *Geophys. Res. Lett., 5,* 1-4, 1978.

Hartzell, S., Comparison of seismic waveform inversion results with the rupture history of a finite fault: Application to the 1986 North Palm Springs, California, earthquake, *J. Geophys. Res., 94,* 7515-7534, 1989.

Haskell, N. A., Analytic approximation for the elastic radiation from a contained underground explosion, *J. Geophys. Res., 72,* 2583-2587, 1967.

Helmberger, D. V., and D. M. Hadley, seismic source time functions and attenuation from local and teleseismic observations of the NTS events Jorum and Handley, *Bull. Seismol. Soc. Am., 71,* 51-67, 1981.

Helmberger, D. V., and D. G. Harkrider, Seismic source descriptions of underground explosion and a depth discriminate, *Geophys. J. R. Astron. Soc., 31,* 45-66, 1972.

Herrmann, R. B., C. A. Langston, and J. E. Zollweg, The Sharpsburg, Kentucky, earthquake of 27 July 1980, *Bull. Seismol. Soc. Am., 72,* 1219-1239, 1982.

Hough, S. E., L. Seeber, A. Lerner-Lam, and J.G. Armbruster, Empirical Green's function analysis of Loma Prieta aftershocks, *Bull. Seismol. Soc. Am., 81*, 1737-1753, 1991.

Hutchings, L. J., Modeling near-source earthquake ground motion with empirical Green's functions, Ph.D. dissertation, 180 pp., State Univ. of N.Y. at Binghamton, 1987.

Hutchings, L., and F. Wu, Empirical Green's functions from small earthquakes: A waveform study of locally recorded aftershocks of the 1971 San Fernando earthquake, *J. Geophys. Res., 95*, 1187-1214, 1990.

Jiao, W., and T. C. Wallace, Study of the relative source time function of the Lop Nor explosion and the attenuation bias, *Eos Trans. AGU, 74(43), Fall Meeting suppl.*, 449, 1993.

Jih, R.-S., and R. A. Wagner, Recent methodological developments in magnitude determination and yield estimation with applications to Semipalatinsk explosions, *Tech. Rep. PL-TR-91-2212(I)*, 90 pp., Phillips Laboratory, Hanscom, 1991.

Kanamori, H., H.-K. Thio, D. Dreger, E. Hauksson, and T. Heaton, Initial investigation of the Landers, California, earthquake of 28 June 1992 using TERRAscope, *Geophys. Res. Lett., 19*, 2267-2270, 1992.

King, C.-Y., A. M. Abo-Zena, and J. N. Murdoc, Teleseismic source parameters of the LONGSHOT, MILROW, and CANIKIN nuclear explosions, *J. Geophys. Res., 79*, 712-718, 1974.

Lay, T., The teleseismic manifestation of *pP*: Problems and paradoxes, in *Explosion Source Phenomenology, Geophys. Monogr. Ser., Vol. 65*, edited by S. Taylor, H. Pattern, and P. Richards, pp. 109-125, AGU, Washington, D.C., 1991.

Lay, T., D. V. Helmberger, and D. G., Harkrider, Source models and yield scaling relations for underground nuclear explosions at Amchitka Island, *Bull. Seismol. Soc. Am., 74*, 843-862, 1984a.

Lay, T., L. J. Burdick, and D. V. Helmberger, Estimating the yields of the Amchitka tests by waveform intercorrelation, *Geophys. J. R. Astron. Soc., 78*, 181-201, 1984b.

Li, Y., and C. H. Thurber, Source properties of two microearthquakes in Kilauea volcano, Hawaii, *Bull. Seismol. Soc. Am., 78*, 1123-1132, 1988.

Li, Y., and N. M. Toksöz, Study of the source process of the 1992 Colombia $Ms=7.3$ earthquake with the empirical Green's function method, *Geophys. Res. Lett., 20*, 1087-1090, 1993.

Li, Y., N. M. Toksöz, and W. Rodi, Investigation of source process of large earthquakes and nuclear explosions with the EGF method, *Seismol. Res. Lett., 64*, 31, 1993.

Mangino, S., and J. Ebel, The receiver function beneath the Chinese digital seismograph network (CDSN) stations: Preliminary results, in *Proceedings of the 14th Annual PL/DARPA Seismic Research Symposium*, pp. 289-296, Phillips Laboratory, Hanscom, 1992.

Masse, R., Review of seismic source models for underground nuclear explosions, *Bull. Seismol. Soc. Am., 71*, 1249-1268, 1981.

Matzko, R., Geology of the Chinese nuclear test site near Lop Nor, Xinjiang Province, China, in *Proceedings of the 14th Annual PL/DARPA Seismic Research Symposium*, pp. 297-303, Phillips Laboratory, Hanscom, 1992.

Merritt, M. L., Reaction of shallow onshore waters to ground shock, *Bull. Seismol. Soc. Am., 62*, 1543-1557, 1972.

Mori, J., Fault plane determinations for three small earthquakes along the San Jacinto fault California: Search for cross faults, *J. Geophys. Res., 98*, 17,711-17,722, 1993.

Mori, J., and A. Frankel, Source parameters for small events associated with the 1986 North Palm Springs, California, earthquake determined using empirical Green functions, *Bull. Seismol. Soc. Am., 80*, 278-295, 1990.

Mori, J., and S. Hartzell, Source inversion of the 1988 Upland, California, earthquake: Determination of a fault for a small event, *Bull. Seismol. Soc. Am., 80*, 507-518, 1990.

Mueller, C., Source pulse enhancement by deconvolution of an empirical Green's function, *Geophys. Res. Lett., 12*, 33-36, 1985.

Mueller, R. A., and J. R. Murphy, Seismic characteristics of underground nuclear detonations, 1, Seismic spectrum scaling, *Bull. Seismol. Soc. Am., 61*, 1675-1692, 1971.

Müller, G., Seismic moment and long period radiation of underground nuclear explosions, *Bull. Seismol. Soc. Am., 63*, 847-557, 1973.

Murphy, J. R., Seismic source functions and magnitude determinations for underground nuclear detonations, *Bull. Seismol. Soc. Am., 67*, 135-158, 1977.

Murphy, J. R., Free-field seismic observations from underground nuclear explosions, in *Explosion Source Phenomenology, Geophys. Monogr. Ser., Vol. 65*, edited by S. Taylor, H. Pattern, and P. Richards, pp. 25-33, AGU, Washington, D.C., 1991.

Nabelek, J., Determination of earthquake source parameters from body waves, Ph.D. thesis, Mass. Inst. of Technol., Cambridge, 361 pp., 1984.

Nabelek, J., and G. Suarez, The 1983 Goodnow earthquake in the central Adirondacks, New York: Rupture of a simple, circular crack, *Bull. Seismol. Soc. Am., 79,* 1762-1777, 1989.

Patton, H. J., Reference point equalization method for determining the source and path effects of surface waves, *J. Geophys. Res., 85,* 821-848, 1980.

Patton, H. J., Characterization of spall from observed strong ground motions on Pahute Mesa, *Bull. Seismol. Soc. Am., 80,* 1326-1345, 1990.

Patton, H. J., Seismic moment estimation and the scaling of the long-period explosion source spectrum, in *Explosion Source Phenomenology, Geophys. Monogr. Ser., Vol. 65,* edited by S. Taylor, H. Pattern, and P. Richards, pp. 171-183, AGU, Washington, D.C., 1991.

Pechmann, J. C., and H. Kanamori, Waveforms and spectra of preshocks and aftershocks of the 1979 Imperial Valley, California, earthquake: Evidence of fault heterogeneity?, *J. Geophys. Res., 87,* 10,579-10,597, 1982.

Poupinet, G., W. L., Ellsworth, and J. Frechet, Monitoring velocity variations in the crust using earthquake doublets: An application to the Calaveras fault, California, *J. Geophys. Res., 89,* 5719-5731, 1984.

Quin, H. R., and C. H. Thurber, Seismic velocity structure and event relocation in Kazakhstan from secondary *P* phases, *Bull. Seismol. Soc. Am., 82,* 2494-2510, 1992.

Ringdal, F., P. D. Marshall, and R. W. Alewine, Seismic yield determination of Soviet underground nuclear explosions at the Shengan river test site, *Geophys J. Int., 109,* 65-77, 1992.

Schlittenhardt, J., The effects of spall on teleseismic *P*-waves: An investigation with theoretical seismograms, in *Explosion Source Phenomenology, Geophys. Monogr. Ser., Vol. 65,* edited by S. Taylor, H. Pattern, and P. Richards, pp. 141-150, AGU, Washington, D.C., 1991.

Somerviller, P. G., J. P. Mclaren, L. V. LeFever, R. W. Burger, and D. V. Helmberger, Comparison of source scaling relations of eastern and western North American earthquakes, *Bull. Seismol. Soc. Am., 77,* 322-346, 1987.

Springer, D. L., Secondary sources of seismic waves from underground nuclear explosions, *Bull. Seismol. Soc. Am., 64,* 581-594, 1974.

Stump, B. W., Constraints on explosive sources with spall from near-source waveform, *Bull. Seismol. Soc. Am., 75,* 361-377, 1985.

Stump, B. W., and R. E. Reinke, Free-field and free surface ground motions from nuclear explosions, their spatial variations, and the constraint of physical source mechanisms, in

Explosion Source Phenomenology, Geophys. Monogr. Ser., Vol. 65, edited by S. Taylor, H. Pattern, and P. Richards, pp. 47-61, AGU, Washington, D.C., 1991.

Taylor, S. R., and G. E. Randall, The effects of spall on regional seismograms, *Geophys. Res. Lett., 16*, 211-214, 1989.

Thurber, C. H., H. R. Quin, and P. G. Richards, Accurate locations of nuclear explosions in Balapan, Kazakhstan, 1987 to 1989, *Geophys. Res. Lett., 20*, 399-402, 1993.

Toksöz, M. N., and H. H. Kehrer, Tectonic strain release by underground explosions and its effects on seismic discrimination, *Geophys. J. R. Astron. Soc., 31*, 141-161, 1972.

Toksöz, M. N., A. Ben-Menahem, and D. G. Harkrider, Determination of source parameters of explosions and earthquakes by amplitude equalization of seismic surface waves, 1, Underground nuclear explosions, *J. Geophys. Res., 69*, 4355-4366, 1964.

Toksöz, M. N., D. G. Harkrider, and A. Ben-Menahem, Determination of source parameters of explosions and earthquakes by amplitude equalization of seismic surface waves, 2, Release tectonic strain by underground nuclear explosions and mechanism of earthquakes, *J. Geophys. Res., 70*, 907-922, 1965.

Toksöz, M. N., Y. Li, and W. Rodi, Seismic source characterization with empirical Green's function and relative location techniques, in *Proceedings of the 15th Annual PL/DARPA Seismic Research Symposium*, pp. 398-404, Phillips Laboratory, Hanscom, 1993.

Velasco, A., C. J. Ammon, and T. Lay, Recent large earthquakes near Cape Mendocino and in the Gorda plate: Broadband source time functions, fault orientations, and rupture complexities, *J. Geophys. Res., 99*, 711-728, 1994.

Viecelli, J. A., Spallation and the generation of surface waves by an underground explosions, *J. Geophys. Res., 78*, 2475-2487, 1973.

von Seggern, D., and R. Blandford, Source time function and spectra for underground nuclear explosions, *Geophys. J., 31*, 83-79, 1972.

Wallace, T., Body wave observations of tectonic release, in *Explosion Source Phenomenology, Geophys. Monogr. Ser., Vol. 65*, edited by S. Taylor, H. Pattern, and P. Richards, pp. 161-170, AGU, Washington, D.C., 1991.

Wallace, T., D. Helmberger, and G. Engen, Evidence of tectonic release from underground nuclear explosions in long period S waves, *Bull. Seismol. Soc. Am., 75*, 157-174, 1985.

Weidner, D. J., and K. Aki, Focal depth and mechanism of mid-ocean ridge earthquakes, *J. Geophys. Res., 78*, 1818-1831, 1973.

Wu, F. T., Parkfield earthquake of June 28, 1966: Magnitude and source mechanism, *Bull. Seismol. Soc. Am.*, *58*, 689-710, 1968.

Xie, J., Z. Liu, R. Herrmann, and E. Cranswick, Source processes of three aftershocks of the 1983 Goodnow, New York, earthquake: High-resolution image of small, symmetric ruptures, *Bull. Seismol. Soc. Am.*, *81*, 818-843, 1991.

Table 1. Hypocentral Parameters of Nuclear Explosions in Central Asia

No.	Date*	Time, UT	Latitude,	Longitude,	Depth†, km	m_b	M_S
1	881112	0330:03.7	50.078° N	79.988° E	0.30	5.3	
1g	880614	0227:06.4	50.045° N	79.005° E	0.24	5.0	4.1
2‡	880914	0359:57.4	49.833° N	78.808° E	0.50	6.1	4.5
2g	890708	0346:57.6	49.888° N	78.802° E	0.37	5.6	4.1
3	900816	0459:57.6	41.564° N	88.770° E	0.57	6.2	
3g	931005	0159:56.5	41.647° N	88.681° E	0.46	5.9	4.8
4	920521	0459:57.5	41.604° N	88.813° E	0.71	6.5	5.0
4g-a	931005	0159:56.5	41.647° N	88.681° E	0.46	5.9	4.8
4g-b	900816	0459:57.6	41.564° N	88.770° E	0.57	6.2	

*Read 881112 as Nov. 12, 1988: year, month, day.
†Estimated with the formula of *Jih and Wagner* [1991].
‡JVE2.

Table 2. Hypocentral Parameters of Nuclear Earthquakes in Central Asia

No.	Date*	Time, UT	Latitude,	Longitude,	Depth, km	m_b	M_S
1	900515	2229:59.3	36.112° N	100.118° E	14	5.5	5.2
1 g	900428	0356:46.7	36.225° N	99.999° E	10	4.8	
2	900417	0159:33.4	39.436° N	74.900° E	33†	6.0	6.2
2 g	900901	2132:49.8	39.375° N	74.760° E	17	4.7	3.8
3	900614	1247:28.8	47.869° N	85.076° E	58†	6.1	6.8
3 g	900803	0915:06.1	47.963° N	84.961° E	33†	6.0	6.1
4	931002	0842:32.8	38.141° N	88.638° E	16	6.2	6.3
4 g	931002	0943:19.5	38.127° N	88.502° E	12	5.7	5.3
5	930809	1242:50.0	36.348° N	70.840° E	233	6.3	
5 g	930809	1138:33.0	36.395° N	70.707° E	230	5.8	
6-1	900426	0937:10.9	36.040° N	100.274° E	10	5.7	
6-2	900426	0937:15.0	35.986° N	100.245° E	8	6.5	6.9
6-3	900426	0937:45.3	36.239° N	100.254° E	10	6.3	
6 g	900507	0517:37.6	36.032° N	100.341° E	33†	5.3	5.0
7	920819	0204:37.4	42.142° N	73.575° E	27	6.6	7.4
7 g	920819	0312:04.9	42.107° N	73.264° E	21	6.0	6.3

*Read 900515 as May 15, 1990: year, month, day.
†Depths are not well constrained.

Table 3. Source Parameters of Nuclear Explosions in Central Asia

No.	Date*	M_s	m_b	$M_o{}^{m_b}$, 10^{16} Nm	M_o/M_{og},	$M_o{}^{STF}$, 10^{16} Nm	f_c, Hz	R_e, km	$\Delta\sigma$ †, MPa
1g	880614	4.1	5.0	0.08					
1	881112		5.3	0.17	2.1	0.17	3.3±1.0	0.25±0.10	13 (5-61)
2g	890708	4.1	5.6	0.36					
2-1	880914	4.5	6.1	1.27	3.4	1.22	2.5±0.6	0.33±0.11	41 (18-140)
2-2					0.6	0.22			
3g	931005	4.8	5.9	0.76					
3	900816		6.2	1.63	2.2	1.67	2.4±0.6	0.34±0.12	52 (21-191)
4g-a	931005	4.8	5.9	0.76					
4-1	920521	5.0	6.5	3.49	4.3	3.27	1.6±0.4	0.52±0.15	28 (13- 79)
4-2					1.2	0.91			
4g-b	900816		6.2	1.63					
4-1	920521	5.0	6.5	3.49	1.9	3.10	1.6±0.4	0.52±0.15	27 (13- 75)
4-2					0.6	0.98			

*Read 880614 as June14, 1988: year, month, day.
†Values in parentheses are the minimum and maximum value, respectively.

Table 4. Comparison of Spall Slapdown Phases at Different Test Sites

Event	Date*	m_b	Depth, km	P_{ss}-P, s	P_{ss} Width, s	Method/Reference/Remark
Cannikin	711106	7.0	1.79	1.96	0.6	TD/Bakun and Johnson [1973]/ATS
				1.95		IC/Lay et al. [1984a]
				1.85		SM/King et al. [1974]
				0.7-1.4		NF/[Springer [1974] and Lay [1991]
				0.8-1.3		LWP/Merritt [1972]
Milrow	691002	6.5	1.22	1.37	0.5	TD/Bakun and Johnson [1973]/ATS
				1.35		IC/Lay et al. [1984a]
				1.35		SM/King et al. [1974]
Lop Nor-92	920521	6.5	0.71†	0.75	0.8	TEGF/this study/XTS
Boxcar	680426	6.3	1.16	1.35	1.0	NF/Springer [1974]/NTS
JVE2	880914	6.1	0.50†	0.45	0.6	TEGF/this study/KTS
Longshot	651029	6.0	0.70	1.40		NF/Springer [1974]/ ATS
				0.87		SM/King et al. [1974]
Hardin	870430	5.8	0.63	1.30		NF/Patton [1990]/NTS
Chancellor	830901	5.7	0.62	0.4-0.6		NF/Patton [1990]/NTS
Baseball	810115	5.6	0.56	1.75		NF/Taylor and Randall [1989]/NTS
Amarillo	890627	4.9	0.60	0.4-0.8		NF/Stump and Reinke [1991]/NTS
Hardhat	620215	4.2	0.29	1.40	0.7	NF/Patton [1990]/NTS
Borrego	780213	3.8	0.56	0.17		NF/Taylor and Randall [1989]/NTS
Merlin	650216		0.30	1.0-1.2		NF/Murphy [1991]/NTS
Hupmobile	680118		0.25	0.45	0.3	NF/Springer [1974]/NTS

IC, intercorrelation; LWP, lake water pressure; NF, near field; SM, spectral method;
TD, teleseismic deconvolution; TEGF, teleseismic EGF.
ATS, Amchitka Test Site; XTS, Xinjiang Test site; NTS, Nevada Test Site; KTS, Kazakhstan Test Site.
*Read 711106 as November 6, 1971: year, month, day.
†Estimated with the formula of *Jih and Wagner* [1991].

Table 5. Broadband *P* Waveform Data of Earthquakes Used in This Study

No.	Date*	Time, UT	Broadband Seismic Stations
1	900515	2229:59.3	LZH
1g	900428	0356:46.7	
2	900417	0159:33.4	GAR WMQ
2g	900901	2132:49.8	
3	900614	1247:28.8	BJI KMI LZH
3g	900803	0915:06.1	
4	931002	0842:32.8	AAK ARU KEV KMI LSA LZH
4g	931002	0943:19.5	TLY WMQ
5	930809	1242:50.0	ANTO CHTO COL KONO
5g	930809	1138:33.0	MAJO PAB TBT
6	900426	0937:15.0	KMI WMQ
6g	900507	0517:37.6	
7	920819	0204:37.4	LZH MDJ WMQ
7g	920819	0312:04.9	

* Read 900515 as May 15, 1990: year, month, day

Table 6. Source Parameters of Earthquakes in Central Asia

No.	Date*	M_s	m_b	M_o^{CMT}, 10^{17} Nm	M_o/M_{og}	M_o^{STF}, 10^{17} Nm	$\tau_{1/2}$, s	r, km	$\Delta\sigma$, MPa	
1g	900428		4.8							
1	900515	5.2	5.5	1.1	15.0		1.5±0.1	3.5+0.2	1.12	(0.95-1.34)†
							1.7±0.2	4.0±0.5	0.75	(0.53-1.12)‡
2g	900901	3.8	4.7							
2	900417	6.2	6.0	12	196		4.3±0.1	10.2±0.2	0.49	(0.47-0.52)†
							4.5±0.2	10.6±0.5	0.44	(0.38-0.51)‡
3g	900803	6.1	6.0	20						
3	900614	6.8	6.0	97	4.95	99	2.6±0.1	6.1±0.2	19.1	(17.3-21.1)§
							5.8±0.5	13.7±1.2	1.68	(1.31-2.22)‡
4g	931002	5.3	5.7							
4	931002	6.3	6.2	14	14.5		1.5±0.1	3.5±0.2	14.3	(12.1-17.0)§
							3.7±0.4	8.7±0.9	0.93	(0.69-1.29)‡
5g	930809		5.8	21						
5-1	930809		6.3	290	8.58	180	3.0±0.1	8.8±0.2	11.6	(10.8-12.4)§
							5.5±0.4	16.2±0.9	1.85	(1.57-2.20)‡
5-2					6.82	143	2.9±0.1	8.6+0.2	9.84	(9.18-10.6)§
							5.4±0.4	15.9±0.9	1.56	(1.32-1.85)‡
6g	900507		5.3	0.96						
6-1	900426	5.7		29	29.3	28	4.1±0.1	9.7±0.2	1.34	(1.26-1.43)†
							4.4±0.4	10.4±0.5	1.09	(0.95-1.26)‡
6-2		6.9	6.5	56	60.8	58	5.0±0.1	11.8±0.2	1.54	(1.47-1.63)†
							5.3±0.2	12.5±0.5	1.30	(1.16-1.47)‡
6-3			6.3		64.0	61	5.5±0.1	13.0±0.2	1.22	(1.16-1.27)†
							5.8±0.2	13.7±0.5	1.04	(0.93-1.16)‡
7g	920819	6.3	6.0							
7-1	920819	7.4	6.6	770	61.6	419	5.6±0.1	13.2±0.2	7.97	(7.62-8.34)§
							8.5±0.5	20.1±1.2	2.26	(1.90-2.72)‡
7-2					22.5	154	3.4±0.1	8.0±0.2	13.2	(12.2-14.2)§
							6.8±0.5	16.0+1.2	1.64	(1.32-2.08)‡
7-3					28.7	197	4.3±0.1	10.1±0.2	8.36	(7.89-8.88)§
							7.5±0.5	17.7±1.2	1.55	(1.28-1.92)‡

*Read 900428 as April 28, 1990: year, month, day.
†Estimated from the RSTF.
‡Results after correcting fot the source pulse widths of the EGF events.
§Estimated from the RSTF and probably overestimated for the stress drops.
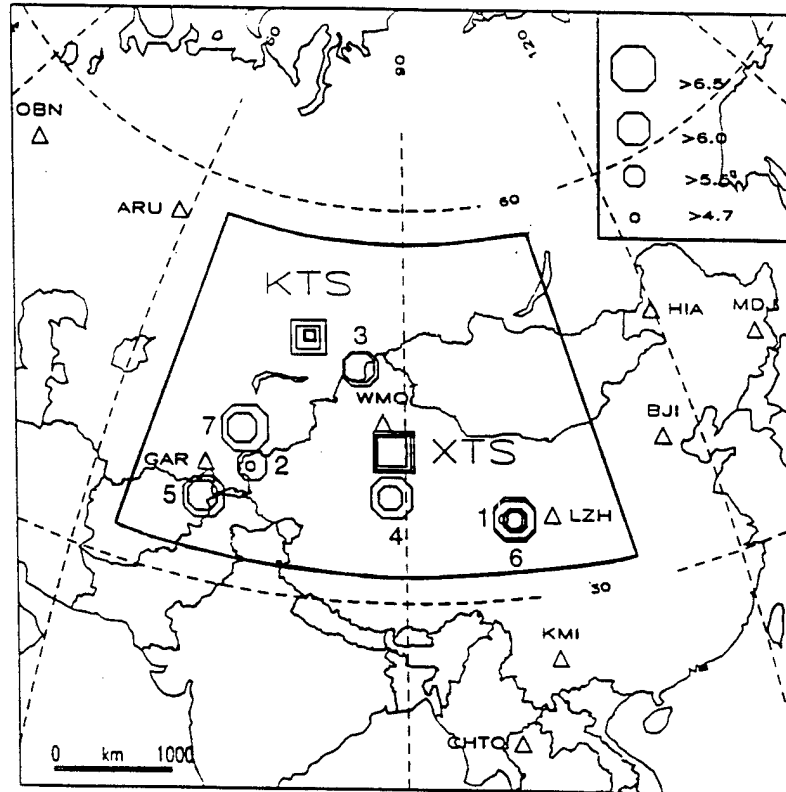
Figure 1. Map of Central Asia showing the study area and epicentral locations of nuclear explosions (squares) and earthquakes (circles). Triangles with three-letter codes are some of the broadband seismic stations used in this study. The numbers marked around the earthquakes correspond to those listed in Tables 2, 5, and 6.
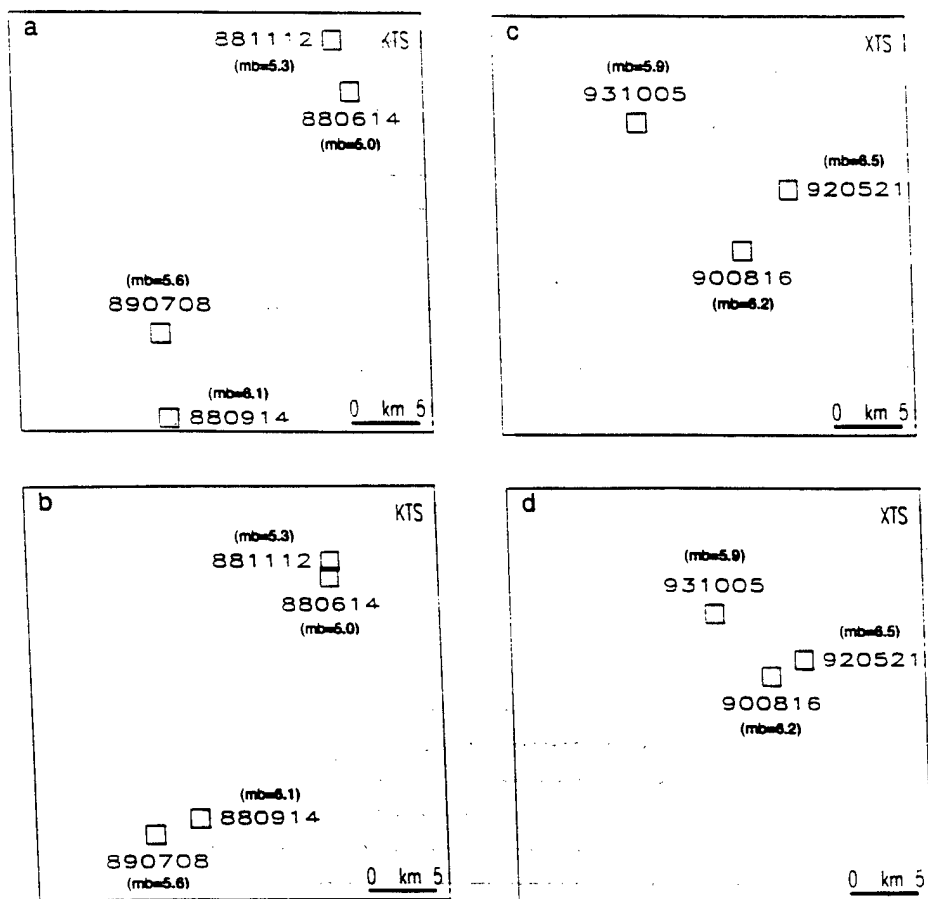
Figure 2. (a) PDE locations for four nuclear explosions at the Kazakhstan Test Site (KTS). (b) Relative relocations for the same events at KTS from SPOT satellite image analysis [*Thurber et al.*, 1993]. (c) PDE locations for three nuclear explosions at the Xinjiang Test Site (XTS). (d) Relocation results for the same events at XTS determined with waveform correlation analysis and relative location technique.
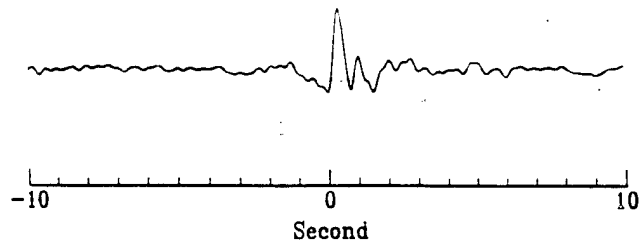
a OBN (AZ=310 D=36): XTS Explosion Pair

Mb=6.5   1992.05.21 04:59:57.5 BHZ
-5123

Mb=6.2 (EGF)   1990.08.16 04:59:57.6 BHZ
-2012

0   50

Second
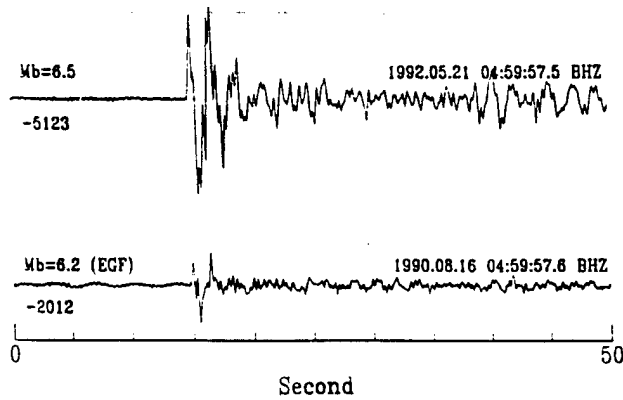
b   Relative Source Time Function

-10   0   10

Second

Figure 3. (a) Vertical component broadband P waveforms of two XTS explosions (m_b = 6.5 and 6.2) recorded at station OBN, Obninsk, Russia, 36° away from XTS. The P waveform of the smaller event is used as an EGF. The numbers below the traces are negative peak amplitudes in digital counts. (b) Retrieved relative STF for the larger explosion. Note that there is a secondary phase on the seismogram of the larger earthquake, suggesting the secondary pulse of RSTF of the 920521 explosion is indeed caused by the explosion source rather than propagation or structure effect.

146

Source Time Function: 881112 03:30 Balapan Explosion mb=5.3

a

EGF=880614 02:27 mb=5.0   STN   AZ   DIST

8.72

WMQ   133   9

Time (Second)

Source Time Function: 880914 04:00 Balapan Explosion mb=6.1

b

EGF=890708 03:47 mb=5.6   STN   AZ   DIST

COL   21   60

HIA   75   26

LZH   118   23

WMQ   132   9

9.16

STACK

Time (Second)
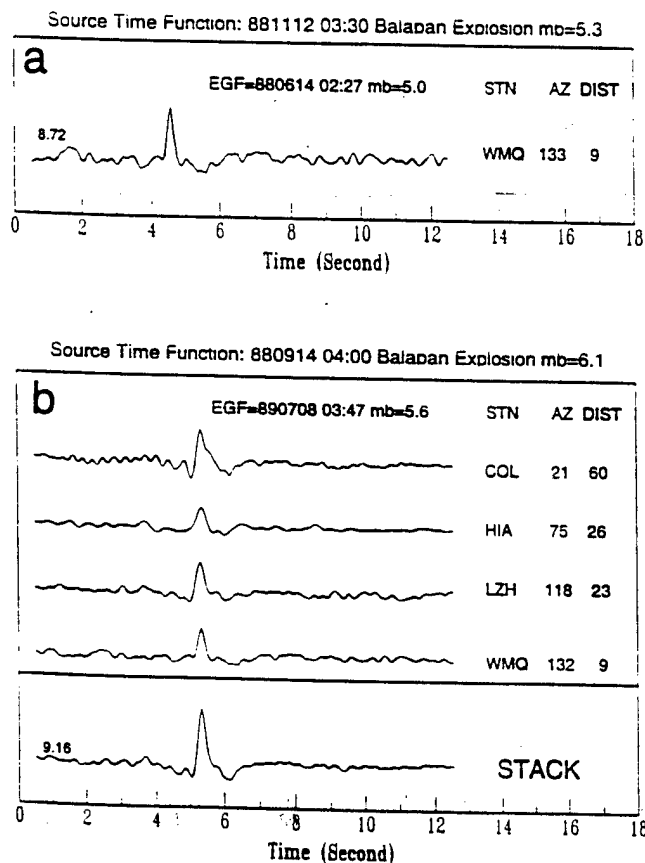
Figure 4. (a) A single-station estimate of the relative STF for the 881112 explosion (m_b = 5.3) in KTS. (b) Single-station estimates and a stacked trace of relative STF for the 880914 JVE2 explosion (m_b = 6.1) in KTS. Numbers following station codes are azimuth and epicentral distance in degrees. The numbers above the RSTF traces are the peak amplitudes of the source pulses.

147
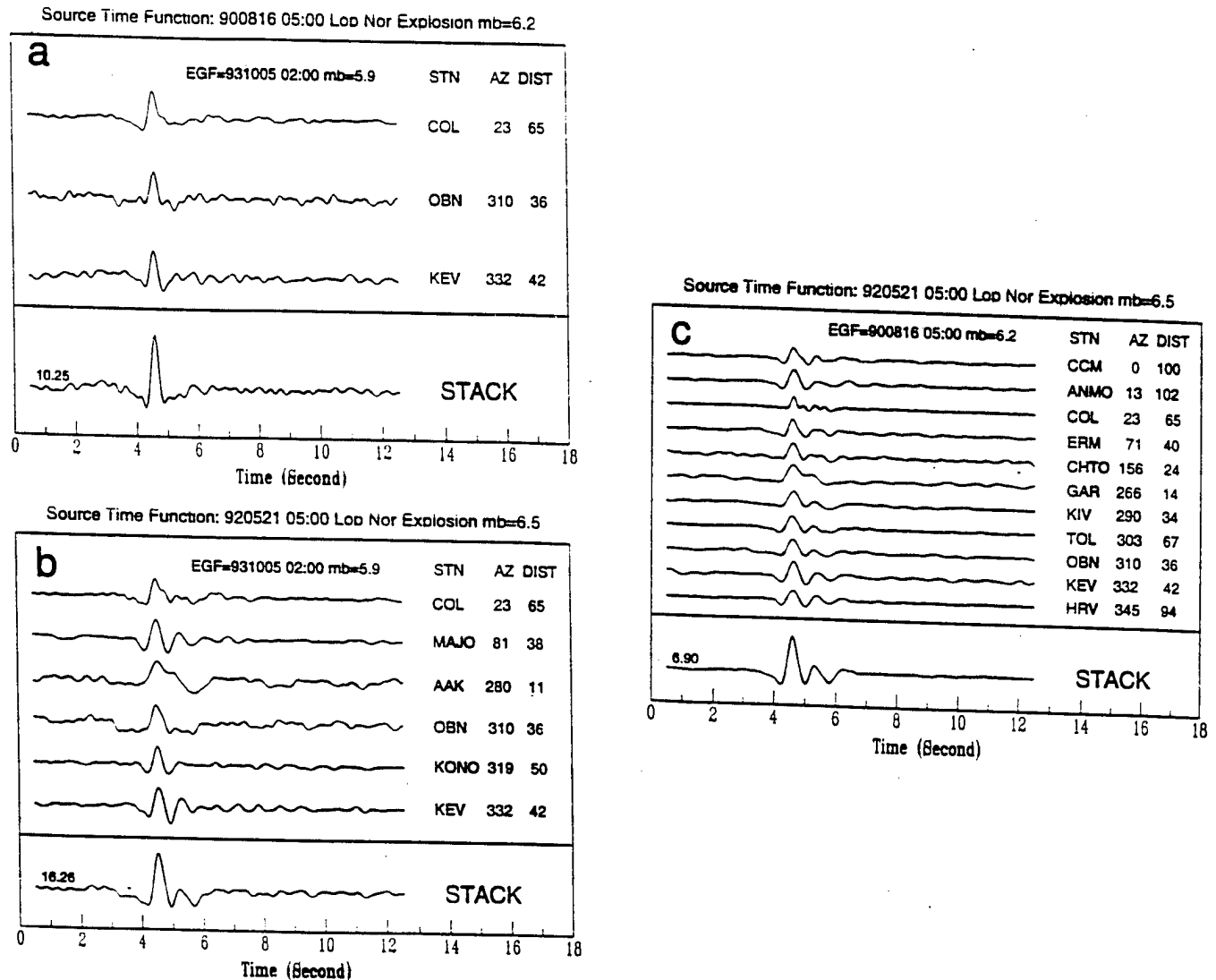
Figure 5. (a) The single-station estimated and stacked RSTF for the 900816 explosion (m_b = 6.2) in XTS, using the 931005 explosion (m_b = 5.9) as the EGF event. (b) Six single-station estimates of RSTF and the stacked trace for the 920521 explosions (m_b = 6.5) in XTS, using the 931005 explosion (m_b = 5.9) as the EGF event. (c) RSTF of the 920521 explosion in XTS estimated with the 900816 explosion (m_b = 6.2) as the EGF event. Numbers following station codes are azimuth and epicentral distance in degrees. The numbers above the stacked RSTF traces are the peak amplitudes of the source pulses. Note that the stacked RSTFs in Figures 5b and 5c, determined with two EGF events, are very similar except for the peak amplitudes.
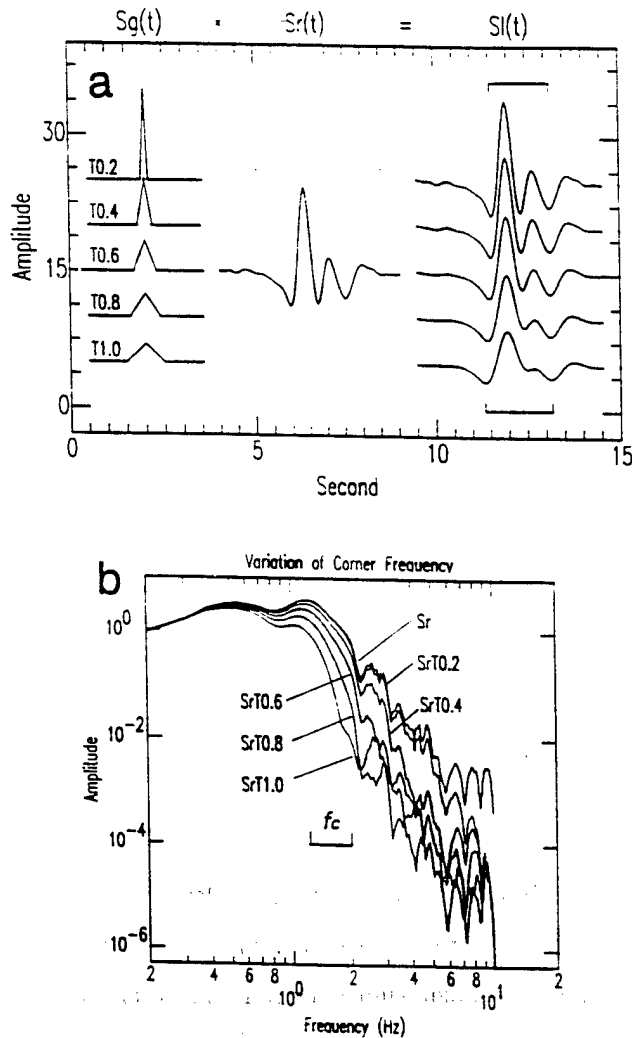
Figure 6. (a) Convolution of an assumed STF of the EGF event, $S_g(t)$, with the RSTF, $S_r(t)$, to predict an "absolute" STF, $S_l(t)$, for the 920521 XTS explosion ($m_b = 6.5$). The $S_g(t)$ are assumed to be triangular pulses with pulse widths of 0.2, 0.4, 0.6, 0.8, and 1.0 s and the peak amplitudes are scaled to be 10, 5, 3.3, 2.5, and 2 so that the areas under the STFs are one unit. The horizontal bars are the minimum and maximum pulse widths of predicted STFs. (b) Spectra of the predicted STFs and the RSTF for the 920521 $m_b = 6.5$ explosion. Horizontal bar presents variation of the corner frequency, f_c, of the RSTF and the predicted STF.

149
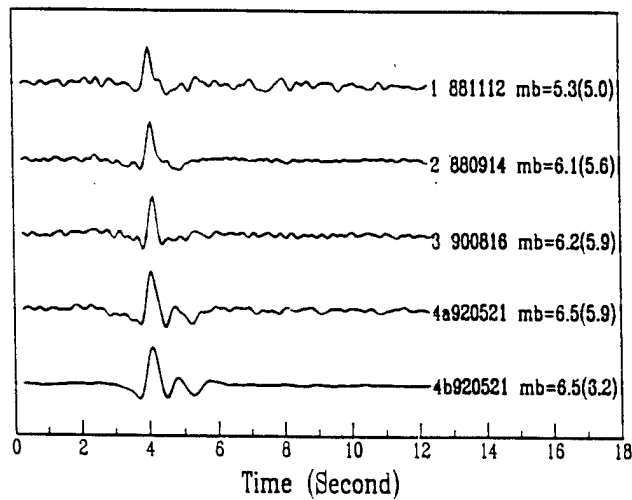
Figure 7. Comparison of RSTFs for the four explosions at KTS and XTS. The numbers in parentheses are m_b magnitudes for the EGF events. The RSTF of two explosions with $m_b = 5.3$ and 6.2 show a simple pulse. The other two explosions ($m_b = 6.1$ and 6.5) have the secondary pulses with smaller amplitudes, which we explain as the spall slapdown phases.

150

Source Time Function: 931002 08:42 Xinjiang Earthquake mb=6.2
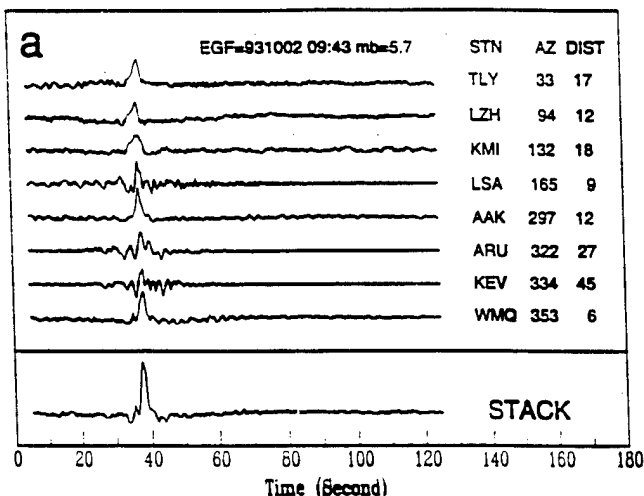
Source Time Function: 930809 12:42 Hindu Kush Earthquake mb=6.3
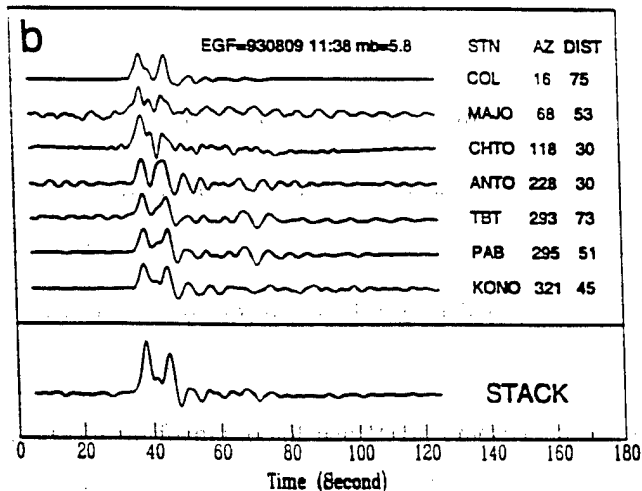
Figure 8. (a) Eight single station estimates of RSTF for the 931002 Xinjiang earthquake ($m_b = 6.2$) and the stacked RSTF trace, indicating a small precursor event before the mainshock. An aftershock ($m_b = 5.7$) was used as the EGF event. (b) Seven single-station estimates of the RSTF and the tacked RSTF trace for the 930809 Hindu Kush deep earthquake ($m_b = 6.3$) indicate that the mainshock is a double event. The EGF event was a $m_b = 5.8$ foreshock.
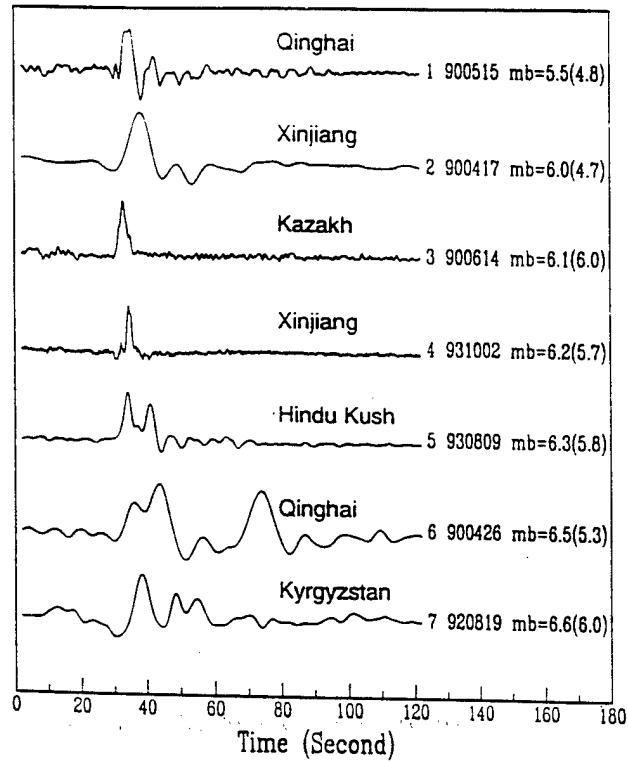
151

Figure 9. Comparison of RSTFs for the seven earthquakes in Central Asia. Top trace is a single-station estimate, and the other traces are stacked RSTFs. The numbers in brackets are m_b magnitudes for the EGF events. The locations of the events are shown in Figure 1 and listed in Table 2. Relative source durations for the earthquakes range from 7 to 29 s. Most of RSTFs show the earthquakes have a complex rupture process. The RSTF of the 900426 Qinghai mainshock sequence indicated that it started with a smaller precursor event about 5 s before the second subevent, followed by the third subevent about 30 s later. PDE reported the origin time of the three subevents was at 0937:10.9, 0937:15.0, and 0937:45.3 (Table 2).
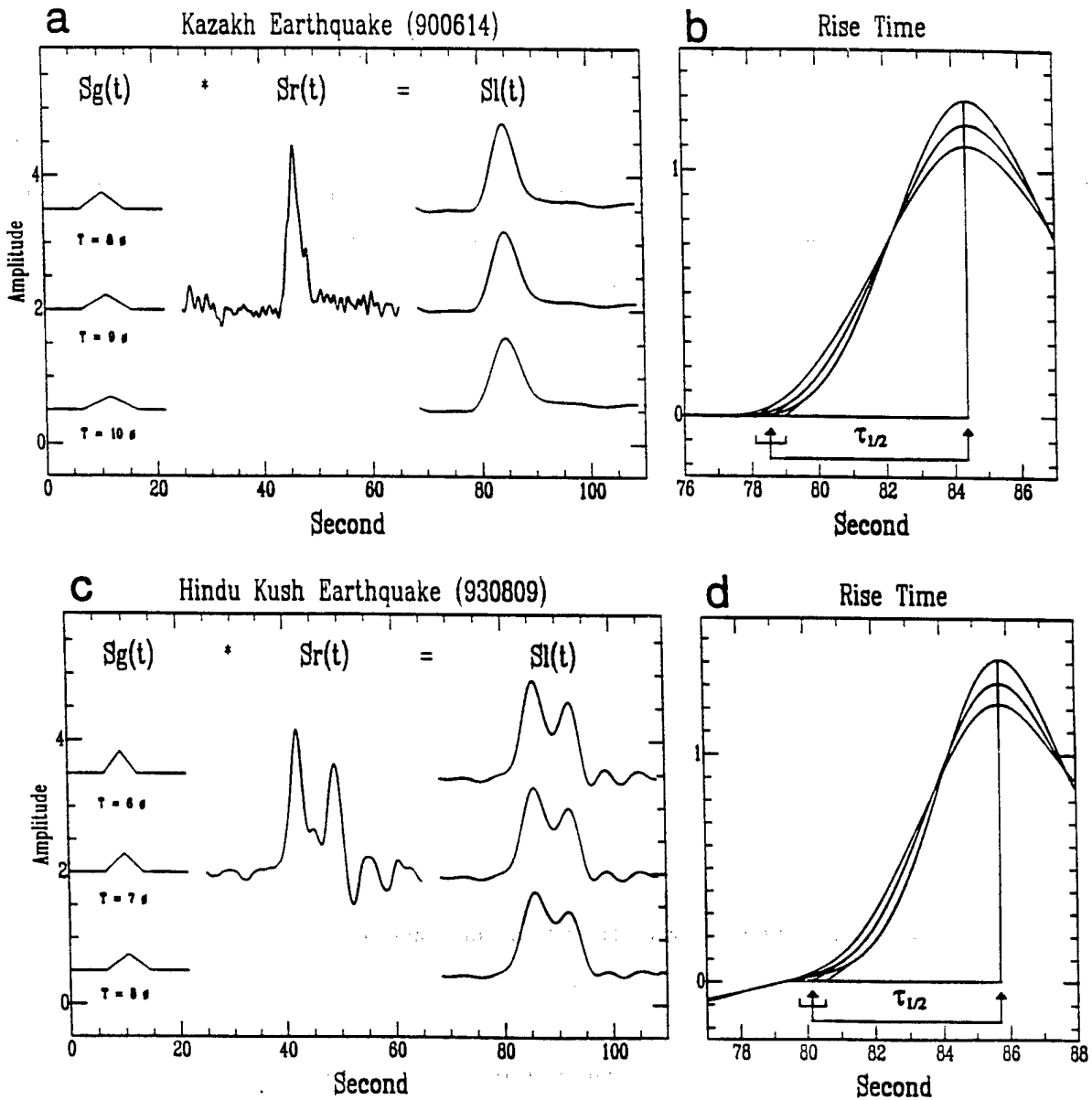
Figure 10. (a) Convolution of an assumed STF of the EGF event, $S_g(t)$, with the RSTF, $S_r(t)$, to retrieve an "absolute" STF, $S_l(t)$, for the Kazakh mainshock ($m_b = 6.1$). The $S_g(t)$ are assumed to be triangular pulses with source duration of 9 ± 1 s, and the peak amplitudes are scaled to be 1/4, 9/2, and 1/5 so that the areas under the STFs equal one. (b) Estimate of the rise time from the three "absolute" STFs of the larger Kazakh event. (c) Recovery of an "absolute" STF for the Hindu Kush mainshock. The source pulse widths of the EGF event are assumed to be 6, 7, and 8 s, and the STF peak amplitudes are scaled to be 1/3, 2/7, and 1/4, respectively. (d) Estimate of the rise time for the first subevent from the three "absolute" STFs of the Hindu Kush mainshock. The horizontal bars in Figures 10b and 10d represent errors of the rise time measurements.
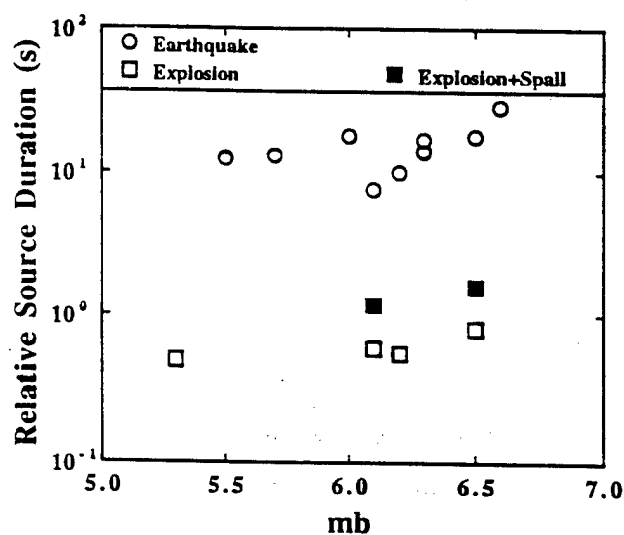
Figure 11. Comparison of relative source durations for earthquakes and explosions in Central Asia. Note that the source durations for explosions are typically less than those of earthquakes by a factor of 10.

Discrimination of Small Earthquakes and Explosions

Y. Li, M. N. Toksöz and W. L. Rodi

Earth Resources Laboratory

Department of Earth, Atmospheric, and Planetary Sciences

Massachusetts Institute of Technology, Cambridge, MA 02139

Contract No. F49620-94-1-0282

Sponsored by AFOSR

ABSTRACT

The discrimination of seismic events as small as magnitude 2.0 at regional distances is of critical importance to achieving the goal of monitoring the Comprehensive Test Ban Treaty (CTBT). Although many discriminants work well for large earthquakes and explosions, little has been learned about their performance for smaller events. In this study, we explore the performance of Pg/Lg and Lg spectral ratio discriminants on smaller events using waveforms of 14 earthquakes and 10 industrial explosions with magnitudes between 1.6 and 3.8 in New England, recorded by short-period stations at distances up to 250 km. We find that the Pg/Lg discriminant fails to separate the small explosion and earthquake populations, but Lg spectral ratio appears to be a good discriminant for these events. Our analysis indicates that the Lg spectra observed from industrial explosions have much larger amplitudes at lower frequencies, while earthquakes have higher amplitudes at higher frequencies, which is reversed from the situation for large earthquakes and explosions. To understand the physical basis of the Lg spectral ratio discriminant for small magnitude seismic events, we performed numerical modeling experiments to study the effects of source properties, depth, and attenuation. Synthetic seismograms demonstrate that the lower frequency content of small explosions, relative to earthquakes, is partially explained by their shallower depth. The

155

energy from a near-surface explosion experiences greater high frequency attenuation in shallow, low Q, layers and greater trapping of low frequency energy in lower velocity layers. Furthermore, the separation between earthquake and explosion Lg spectra is enhanced by two source effects: the shorter source duration of small earthquakes and the extended duration of explosions that are multiply detonated. These modeling results, together with our empirical study of New England events, suggest that Lg spectral ratio is a promising method for discriminating seismic events of small magnitude.

OBJECTIVES

The objective of this project is to characterize the source properties of seismic events, as a function of event type and magnitude, with the ultimate goal of developing effective regional discriminants. In previous work we applied the EGF method to estimate source time functions for a wide variety of events (earthquakes, chemical and nuclear explosions, mining tremors) over a large magnitude range (0.9–6.6), and discovered that the source time function duration could discriminate earthquakes and explosions in certain magnitude ranges, including very small events (magnitudes of 3.0 or less) but not including events in the magnitude range 3–4.5.

To achieve the goal of monitoring a CTBT, it is critical to discriminate seismic events as small as magnitude 2.0 (Murphy, 1995). Although many methods work well for discriminating larger earthquakes and explosions, little has been learned about their performance on the smaller events. The objective of our present work is to understand the physical basis of our previous results for small events, and to compare them to the behavior of discriminants based on Lg.

RESEARCH ACCOMPLISHED

In our previous studies (Toksöz et al., 1993; Li et al., 1994, 1995a,b) we applied an empirical Green's function (EGF) method to characterize seismic sources and estimate source time functions for explosions, earthquakes, and mining tremors covering the magnitude range 0.9–6.6. Figure 1 displays source duration vs. event magnitude for all the events we have studied to date. We see that the earthquake and explosion populations appear to obey different source scaling relations. For magnitudes between 3.5 and 4.5, the earthquake and explosion populations overlap due to the

crossover of two scaling relations with different slopes, indicating that simple source duration is not a good discriminant in this magnitude range. However, for M = 5 and greater, source durations of nuclear explosions are about a factor of 5 to 10 shorter than those of the earthquakes (Figure 1). Thus source duration, like other discriminants such as P/Lg, Lg spectral ratio, and mb-Ms (e.g., Pomeroy et al., 1982; Bennett and Murphy, 1986; Taylor et al., 1988), works as a good discriminant for larger earthquakes and explosions.

For the small (M<3) events we analyzed, the discriminant also works but in an opposite way. The source durations of quarry and construction blasts are significantly longer than those of earthquakes with similar magnitudes (Figure 1). This is consistent with the results of Herrin et al. (1994), who found that Lg spectra of small magnitude earthquakes in the Vogtland area have relatively higher peak frequencies compared to explosions with similar magnitudes. Possible explanations for these observations from small earthquakes and explosions are source, depth, and attenuation effects, i.e.,

1. Smaller earthquakes and explosions may have significantly different source dimensions over space and time. For example, the source duration of industrial blasts is often controlled by shooting practices, such as multiple detonation and ripple firing.

2. Explosions typically are detonated at shallow depths (<1 km) while earthquakes occur at depths of a few kilometers or more.

3. Explosions are typically in a near-surface medium with high attenuation while earthquakes occur in a medium with lower attenuation.

In this study we explore the performance of the P/Lg discriminant and Lg spectral ratio discriminant on the smallest events from our previous work. These include earthquakes and industrial explosions with magnitudes between 1.6 and 3.8 in New England recorded by short-period stations of the M.I.T. seismic network at regional distances.

Figure 3 shows velocity seismograms of one quarry blast (M=2.0) and one earthquake (M=2.8) at Littleton, Massachusetts, recorded at station DNH, which is about 80 km from the epicenters (see Figure 4). As we expected, the small earthquake has a much richer high frequency content compared to the explosion. Bandpass filtered seismograms, using 2–4 and 6–8 Hz bands, are also shown in Figure 3. For the explosion, the Lg peak amplitude on the 2–4 Hz trace is about 5

times greater than that on the 6–8 Hz seismogram. In contrast, the Lg peak amplitude on the 2–4 Hz seismogram is about 2 times smaller than that on the 6–8 Hz seismogram. The Fourier spectra of the Lg phases from the filtered traces (bottom of Figure 3) show this same pattern, with the explosion displaying relatively more low frequency energy. Since the two events have very similar epicenters and are recorded at a common station, we believe that the observed differences between their Lg spectral patterns are mainly caused by differences between the sources themselves and by effects related to focal depth differences, as opposed to propagation along different paths. This suggests that Lg spectral ratios may generally discriminate between small earthquakes from explosions.

It is interesting to compare this result to an example with large events. Figure 2 shows Lg spectra of one Xinjang earthquake (931002, $m_b6.2$) and one Lop Nor explosion (900816, $m_b6.2$) recorded at station ARU about 25 degrees away. We see that the Lg spectral ratio between higher (0.4 to 2 Hz) and lower (0.04 to 0.2 Hz) frequency bands is much higher for the explosion than for the earthquake. That is, the large explosion has relatively higher peak frequencies compared to the large earthquake, which is reversed from the small event example of Figure 3. Again, the two events have similar propagation paths and, considering also the lower frequencies used, the Lg spectra are probably dominated by the source effect. The behavior of Lg spectral ratios for small vs. large events suggests that the source scaling relations for source duration may be true in general.

Next, we apply the Lg spectral ratio discriminant to 10 explosions (M=1.6 to 2.7) and 14 earthquakes (M=2.2 to 3.8) in New England (see Figure 4). The spectral ratio Lg(2–4Hz)/Lg(6–8Hz) plotted against epicentral distance and magnitude are shown in Figure 5. We find that the Lg spectral ratio separates well the earthquake and explosion populations, although the magnitude and distance ranges containing both types of events are limited. We note that Pg/Lg at either 2-4 Hz or 6-8 Hz does not separate the small explosion and earthquake populations.

To understand the physical basis for the Lg spectral ratio discriminant for small magnitude events, we performed tests with synthetic data to study the various effects listed above: source properties, depth, and attenuation. Synthetic seismograms were computed using the discrete wavenumber algorithm of Mandal and Toksöz (1990) and a 1-D structure comprising three crustal layers over a half-space (Table 1). Seismograms were computed for an explosion source at 0.1 km

depth and a thrust earthquake at a depth of 4 km. The source-receiver distance is 80 km. We selected both source time functions to be a triangle pulse with time duration of 0.1 s. The synthetic velocity seismograms for the explosion and earthquake are shown in Figures 6b and 6c, and the Lg spectra are displayed in Figures 7b and 7c. From the seismograms and Lg spectra we can see that, for the same source pulse, the explosion has much higher amplitudes at lower frequencies (< 4Hz) while the earthquake has higher amplitudes at higher frequencies (> 6Hz). Since the explosion is detonated in the more attenuating surface layer, and ray paths go through this layer twice, there is a greater loss of high frequency energy from this source compared to the earthquake, which is in the second layer of the model. There may also be an enhancement of lower frequency energy from the explosion due to the trapping of energy in the shallow layer.

We also calculated synthetics for a multiply detonated blast at a depth of 0.1 km (Figures 6a and 7a). The multiple explosion has 10 subevents with delay times varying between 0.08 to 0.12 s and a total source duration of 1.0 s. We see that multiple firing increases the energy at lower frequencies and decreases it at higher frequencies, thus increasing the difference from the earthquake synthetic.

As shown in Figure 1, the source duration for a small earthquake is typically 2 to 3 times shorter than for an explosion with similar magnitude. To examine how a sharper source pulse for earthquakes affects the Lg ratio discriminant, we recalculated the earthquake synthetic with the triangle source pulse reduced to 0.05 s in duration (Figures 6d and 7d). As expected, the energy content shifts to higher frequency, further enhancing the difference between the earthquake and explosions.

We applied the Lg(2-4Hz)/Lg(6-8Hz) discriminant to the synthetic data from all four cases. The Lg spectra in the two frequency bands are shown for the multiple blast, single blast, and earthquakes with differing source durations in Figures 8a–8d, respectively. The Lg spectral ratio between the two frequency bands clearly separates the explosions and earthquakes. The greatest separation is between the multiple explosion (Figure 8a) and the earthquake with a shorter source duration (Figure 8d).

CONCLUSIONS AND RECOMMENDATIONS

The Lg spectral ratio, using frequency bands of 2–4 Hz and 6–8 Hz, discriminates earthquakes and industrial explosions in New England at magnitudes below 3 and epicentral distances up to 250 km. The Pg/Lg discriminant is not effective on these events, however. The success of the Lg spectral ratio discriminant is consistent with our previous work that showed that the source time duration of M<3 earthquakes is 2 to 3 times shorter than that of explosions of similar magnitude.

Based on numerical modeling of earthquake and explosion seismograms in New England, we conclude that the lower frequency content of small explosions, relative to earthquakes, is partially attributable to their shallower depth. The energy from near-surface explosions experiences greater high frequency attenuation in shallow, low Q layers and greater trapping of low frequency energy in lower velocity layers. The separation between earthquake and explosion Lg spectra is enhanced by two source effects: the shorter source duration of small earthquakes and the extended duration of explosions that are multiply detonated.

These results imply that source time duration and Lg spectral ratio are promising discriminants for small earthquake and explosions. The Lg discriminant is particularly interesting since Lg spectra are more directly and easily measured. For future work, therefore, we recommend that Lg spectral discriminants be tested on a large number of events from different regions to assess their general effectiveness and transportability. Of particular importance is to learn their effectiveness on events of magnitude 3 and greater, and at greater distances. To better understand the physical basis for the Lg spectral ratio discriminant, and to provide the knowledge needed to adapt the discriminant to different regions, we recommend further numerical modeling studies aimed at determining how Lg spectra are affected by vertical layering in the crust, and 2-D and 3-D scattering by topographic and geologic features.

REFERENCES

Bennett, T., and J. Murphy, 1986. Analysis of seismic discrimination using regional data from western United States evnets, *Bull. Seis. Soc. Am., 76*, 1069-1086.

Herrin, E., Burlacu, V., Gray, H.L., Swanson, J., Golden, P., and Myers, B., 1994. Research in regional event discrimination using Ms:mb and autoregressive modeling of Lg waves, *Proceedings*, 16th Annual Seismic Research Symposium, Thornwood, New York, Phillips Laboratory, Hanscom AFB, Massachusetts, 152–158. PL-TR-94-2217.

Li, Y., Rodi, W., and Toksöz, M.N., 1994. Seismic source characterization with empirical Green's function and relative location techniques, *Proceedings*, 16th Annual Seismic Research Symposium, Thornwood, New York, Phillips Laboratory, Hanscom AFB, Massachusetts, 231–237. PL-TR-94-2217

Li, Y., Toksöz, M.N., and Rodi, W., 1995a. Source time functions of nuclear explosions and earthquakes in central Asia determined using empirical Green's functions, *J. Geophys. Res., 100*, 659–674.

Li, Y., Rodi, W., and Toksöz, M.N., 1995b. Discrimination of earthquakes, explosions, and mining tremors using the empirical Green's function method, *Proceedings*, 17th Annual Seismic Research Symposium, Scottdale, Arizona, Phillips Laboratory, Hanscom AFB, Massachusetts, 78–87. PL-TR-95-2108

Mandal, B. and Toksöz, M.N., 1990. Computation of complete waveforms in general anisotropic media – results from an explosion source in an anisotropic medium, *Geophys. J. Int., 103*, 33–45.

Murphy, J. R., 1995. An overview of seismic Discrimination issues relevant to CTBT monitoring, *Proceedings*, 17th Annual Seismic Research Symposium, Scottdale, Arizona, Phillips Laboratory, Hanscom AFB, Massachusetts, 88. PL-TR-95-2108

Pomeroy, P.W., J.B. Best, and T.V., McEvilly, 1982. Test ban treaty verification with regional data – a review, *Bull. Seis. Soc. Am., 72*, S89-S129.

Talyor, S.R., N.W.Sherman, and D.D. Marvin, 1988. Spectraal discrimination between NTS explosions and western United States earthquakes at regional distances, *Bull. Seis. Soc. Am., 78*, 1563-1579.

Toksöz, M.N., Li, Y., and Rodi, W., 1993. Seismic source characterization with empirical Green's function and relative location techniques, *Proceedings*, 15th Annual Seismic Research Sympo-
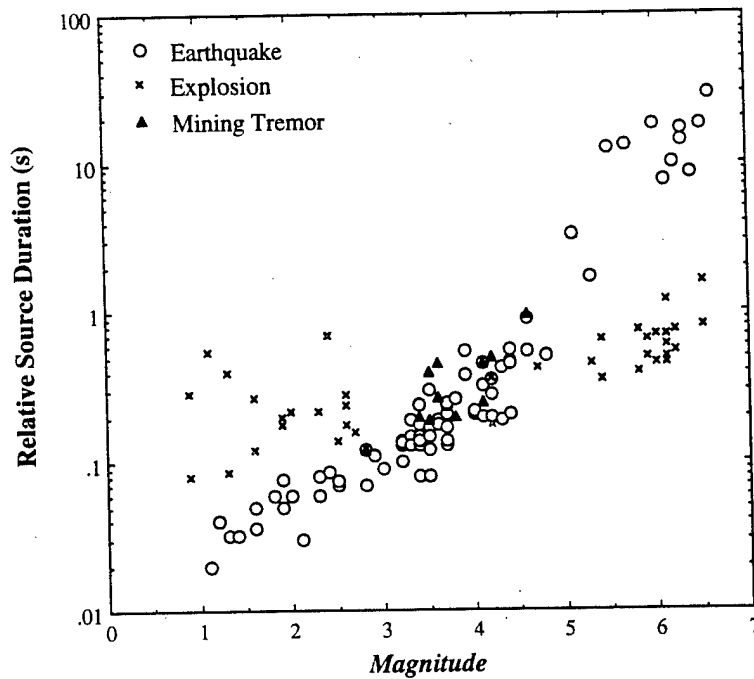
Figure 1: Source duration vs. magnitude for earthquakes (circles), explosions (squares), and mining tremors (triangles), determined by EGF analysis (Li et al., 1995b). For events having magnitude less than 3 or greater than 4.5, the source duration is a good discriminator between earthquakes and explosions. In the remaining magnitude range (3.0 to 4.5) the earthquake, explosion and mining tremor populations overlap.
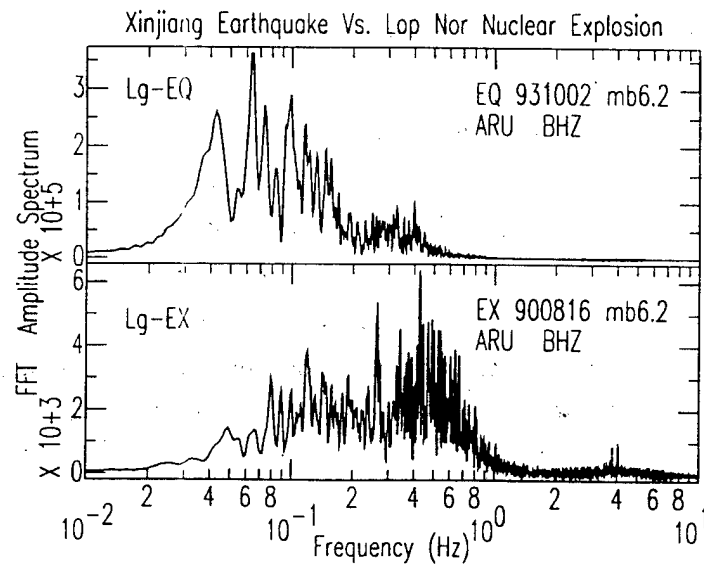

Figure 2: The Lg spectra for an $m_b6.2$ earthquake in Xinjang (931002) and an $m_b6.2$ Lop Nor nuclear explosion (900816) recorded at broadband station ARU.
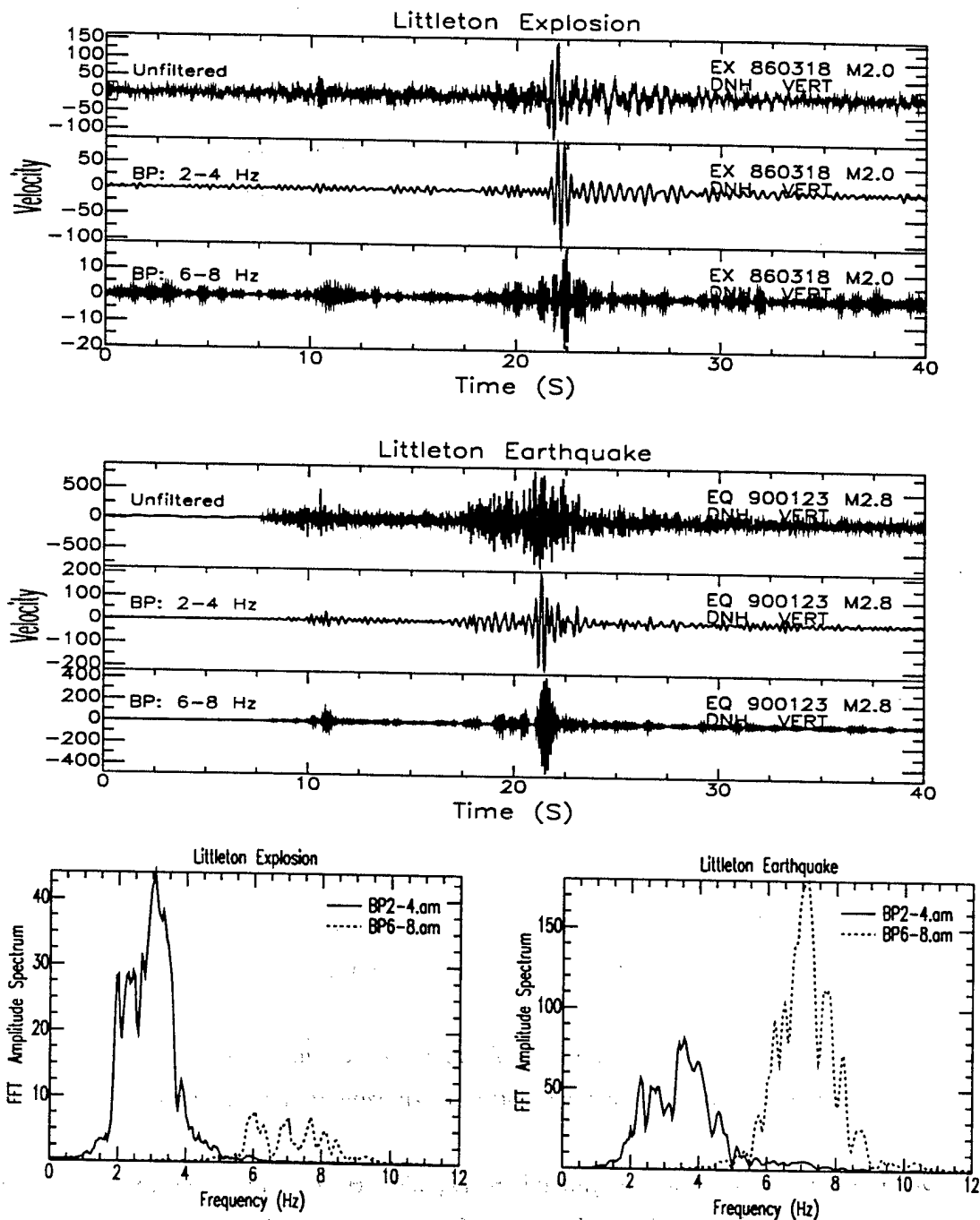
Figure 3: Short period, vertical component seismograms recorded at station DNH (distance 80 km) for a Littleton explosion (top) and a nearby earthquake (middle). Unfiltered, bandpass filtered from 2-4 Hz, and bandpass filtered from 6-8 Hz waveforms are displayed in velocity. Lg spectra of the two frequency bands are plotted for the explosion (bottom left) and the earthquake (bottom right). Note that the Lg spectral ratios between the two frequency bands are different for the explosion and the earthquake.
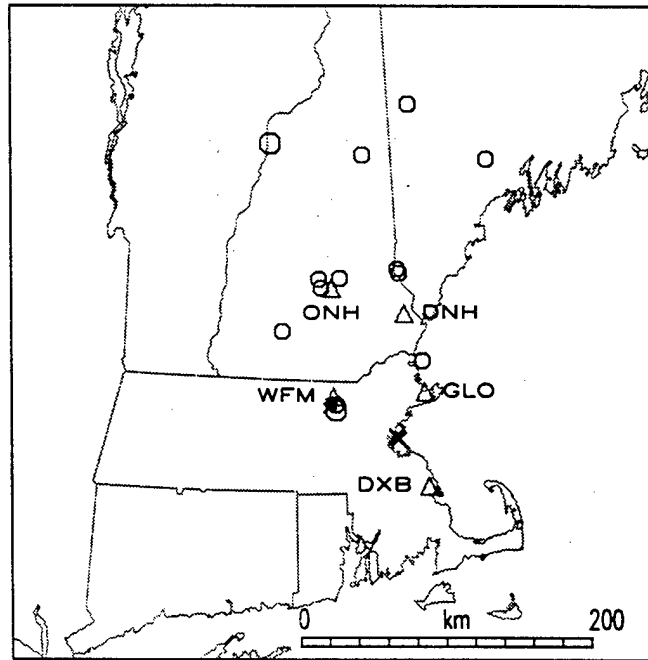
Figure 4: Map of New England showing locations of 10 explosions (crosses) and 14 earthquakes (circles) and 5 M.I.T. seismic stations (triangles) used in this study. The distance from the Littleton earthquakes and explosions (close to station WFM) to station DNH is about 80 km.
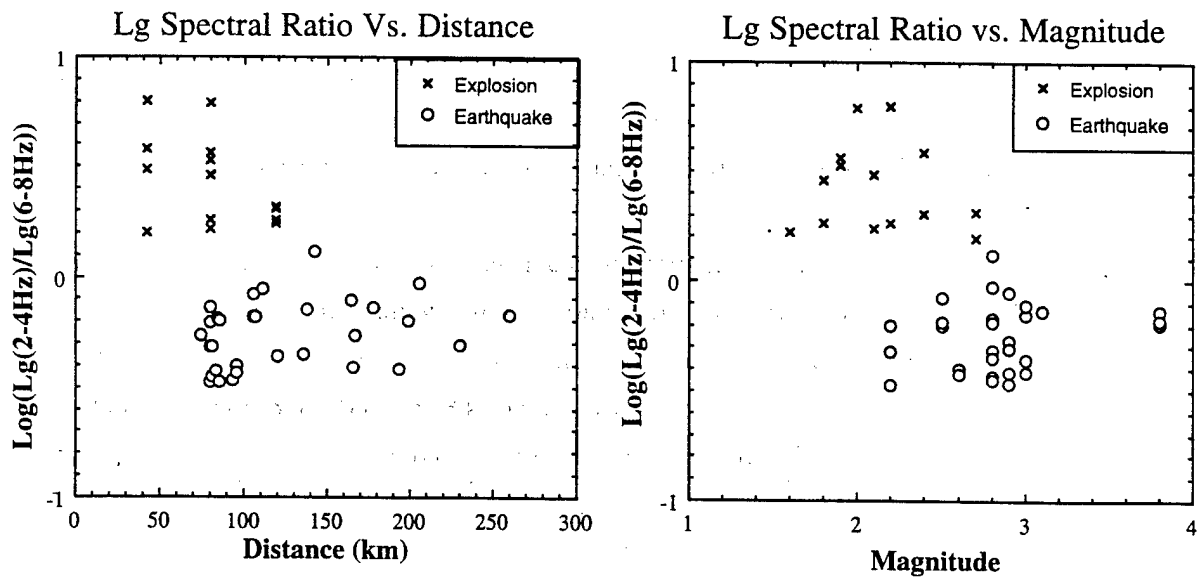

Figure 5: The Lg spectral ratio (2-4Hz)/(6-8Hz) versus epicentral distance (left) and magnitude (right) for explosions (crosses) and earthquakes (circles). The Lg spectral ratio well separates the small earthquake and explosion populations.
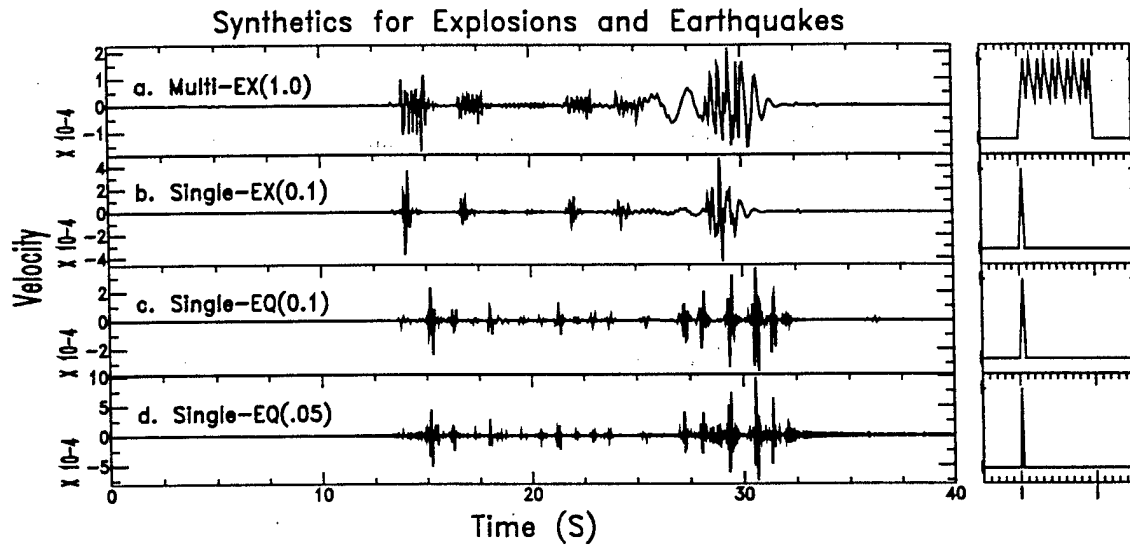
164

Figure 6: Synthetic velocity waveforms for a multiple explosion (a), a single explosion (b), and a thrust earthquakes with a source duration of 0.1 s (c) and 0.05 s (d). The left column shows the source time functions used in the calculation of the synthetics.
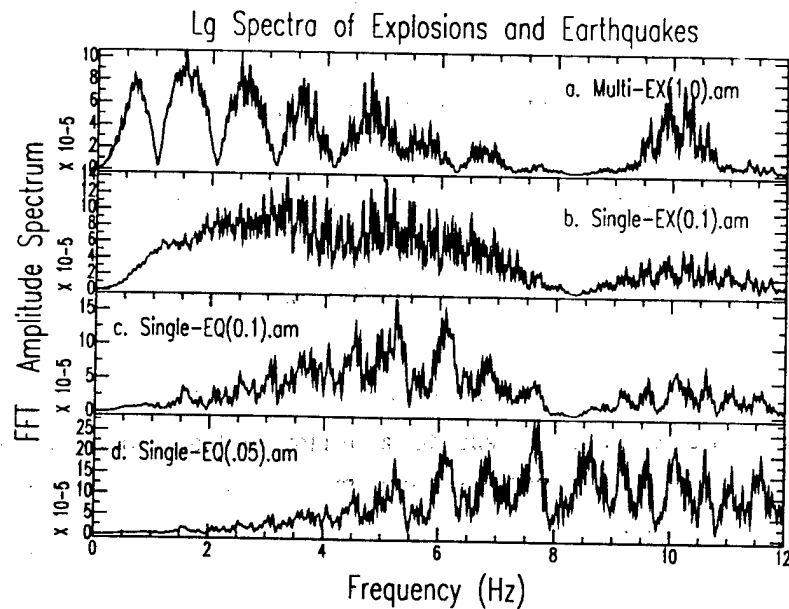

Figure 7: Fourier spectra of the Lg phase for a multiple explosion (a), a single explosion (b), and two thrust earthquakes (c and d) with different source durations. Note that the explosions are richer in lower frequency energy and earthquakes have more higher frequency energy.
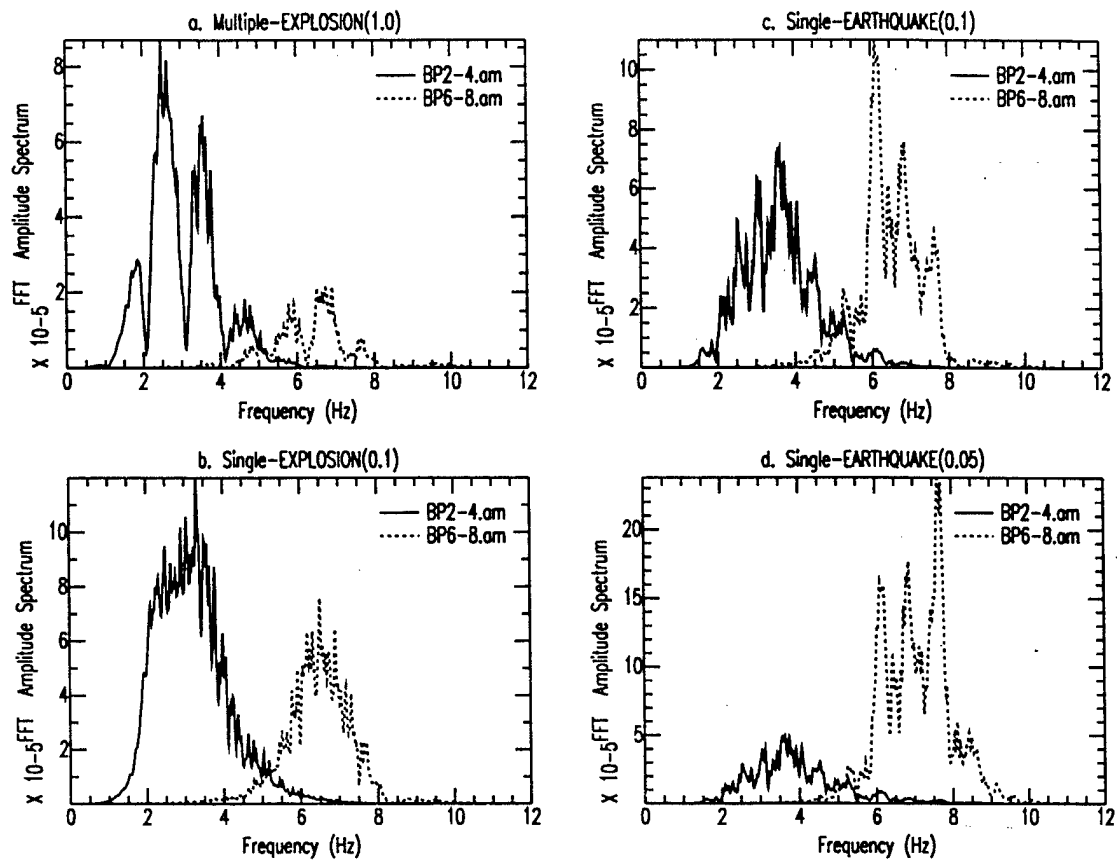
Figure 8: The Lg spectra of two bandpass filtered signals (2-4Hz and 6-8 Hz) for a multiply detonated explosion (a), a single explosion (b), and two earthquakes with source duration of 0.1 and 0.05 s (c and d).

Table 1. Velocity Structure Used in This Study

Layer	Thickness (km)	V_p (km/s)	V_s (km/s)	Density (g/cc)	Q_p	Q_s
1	1.0	5.31	3.07	2.4	70	35
2	12.0	6.06	3.50	2.6	100	50
3	22.0	6.59	3.80	2.7	1000	500
4	∞	8.10	4.68	2.8	∞	∞